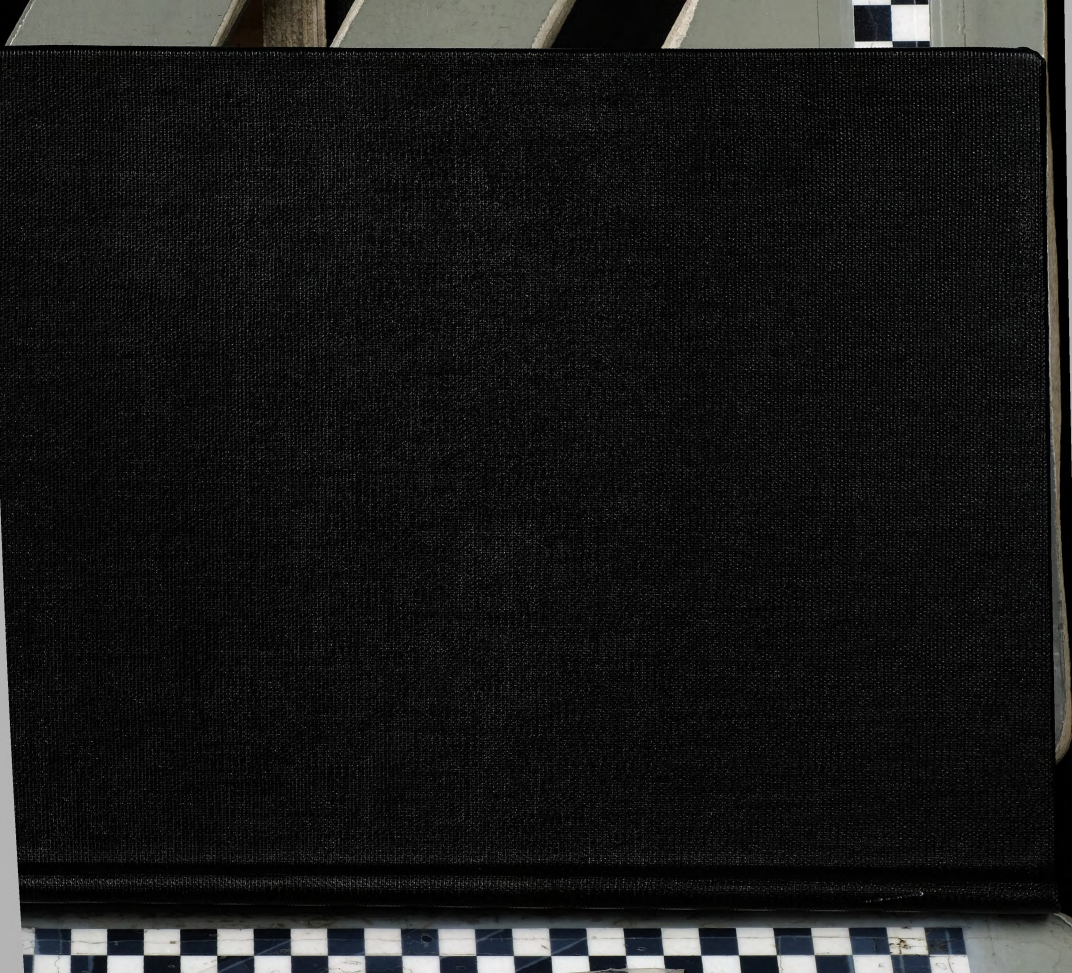

This is to certify that the

dissertation entitled

THE SINGULARITY EXPANSION METHOD FOR
INTEGRATED ELECTRONICS

presented by

George Warren Hanson

has been accepted towards fulfillment
of the requirements for

Ph.D. degree in Electrical Engineering

Dennis P. Nyquist
Major professor

Date July 16, 1991

THE SINGULARITY EXPANSION METHOD FOR INTEGRATED ELECTRONICS

By

George Warren Hanson

A DISSERTATION

Submitted to
Michigan State University
in partial fulfillment of the requirements
for the degree of

DOCTOR OF PHILOSOPHY

Department of Electrical Engineering

1991

In th

devices i

technique

presence

the layere

unknown

singulariti

problem.

An el

embedded

circuits.

investigatic

It is we

exhibit high

device in a

representati

ABSTRACT

THE SINGULARITY EXPANSION METHOD FOR INTEGRATED ELECTRONICS

By

George Warren Hanson

In this dissertation, an approximate theory for the analysis of systems of microstrip devices in the resonant frequency regime is presented. Standard integral-operator techniques applied to this type of problem are often computationally inefficient due to the presence of Sommerfeld integrals associated with the Greens functions which describe the layered environment. When the near-resonant frequency regime is considered, the unknown current on the microstrip device may be represented by a series of pole-singularities in the complex frequency plane, leading to an efficient formulation of the problem.

An electric field integral equation (EFIE) is developed for conducting devices embedded in the tri-layered conductor/film/cover environment typical of microstrip circuits. This EFIE is conceptually exact, and forms the basis for most rigorous investigations of the electromagnetic (EM) properties of such systems.

It is well known that isolated and loosely coupled systems of microstrip components exhibit highly resonant behavior. This motivates expanding the unknown current on the device in a series of pole-singularities in the complex temporal-frequency plane. This representation for the device current leads to an efficient technique for the relatively

general

microstr

effective

The

from a c

leading t

is found

moments

presented

general deduction of EM properties of microstrip circuits. The specific example of a microstrip dipole excited by a nearby transmission line is studied to demonstrate the effectiveness of this method.

The EM properties of systems of coupled, nearly-identical devices are investigated from a coupled set of EFIE's. The singularity expansion technique is again invoked, leading to an approximate perturbation solution for the system-mode resonances. This is found to be an accurate and efficient method when compared to the direct method of moments (MoM) solution to the same problem. Numerical and experimental results are presented for a two-dipole system to support the validity of this approximate solution.

TO MY BEST FRIEND, SHEILA

I wo

support,

his willin

of my stu

Byron Dr

Furth

performin

my fellow

programs

Finall

their cons

would als

computatio

ACKNOWLEDGEMENTS

I would like to express sincere thanks to Dennis P. Nyquist for his guidance, support, and inspiration throughout the course of this research. I especially appreciate his willingness to accommodate my rather difficult schedule during the last few months of my studies. Special thanks are also due Kun-Mu Chen, Edward J. Rothwell, and Byron Drachman for their assistance in completing this research.

Furthermore, I would like to thank James Kallis for the outstanding job he did in performing the experimental component of this work. I would also like to acknowledge my fellow graduate students, in particular Jack Ross for the generous use of his computer programs which enabled efficient data collection for this and other projects.

Finally, I am grateful to my wife, Sheila Hanson, and my mother, Ruth Hanson, for their constant encouragement and support during the course of my graduate study. I would also like to thank Dave and Carol Hyster for their generous provision of computational resources.

TABLE OF CONTENTS

4.

4.

4.

5. C

5.

5.

5.

5.

5.

6. EX

6.

6.

6.

6.

6.

7. CO

Table 4.

Table 4.

Table 7.

LIST OF TABLES

LIST OF FIGURES

Figure

Figure

Figure

Thi

microstr

depicted

This di

investiga

Earl

approxin

rectangul

technique

shapes [

inception

microstri

Most

associated

A rigorou

CHAPTER ONE

INTRODUCTION

This dissertation presents an approximate theory for the analysis of systems of microstrip devices in the resonant frequency regime. A typical microstrip system is depicted in Figure 1.1, consisting of a transmission line feed for a two dipole array. This dissertation is intended to provide an efficient method of analysis for the investigation of electromagnetic phenomena associated with these systems.

Early work on the analysis of microstrip radiator characteristics centered on approximate modeling techniques, such as applying transmission line analogies to rectangular patches fed at the center of a radiating wall [1]. A more sophisticated technique, the modal-expansion method, was latter applied to study a variety of radiator shapes [2]. A thorough survey of microstrip antenna element technology from its inception until 1981 is given by Carver and Mink [3], while a similar survey of microstrip array technology is found in Mailloux et al. [4].

Most of the early methods are approximate, and do not account for all phenomena associated with the radiator itself, and the background environment in which it resides. A rigorous study of microstrip dipole elements was presented by Rana et al. [5], using

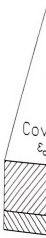

Figure 1.1

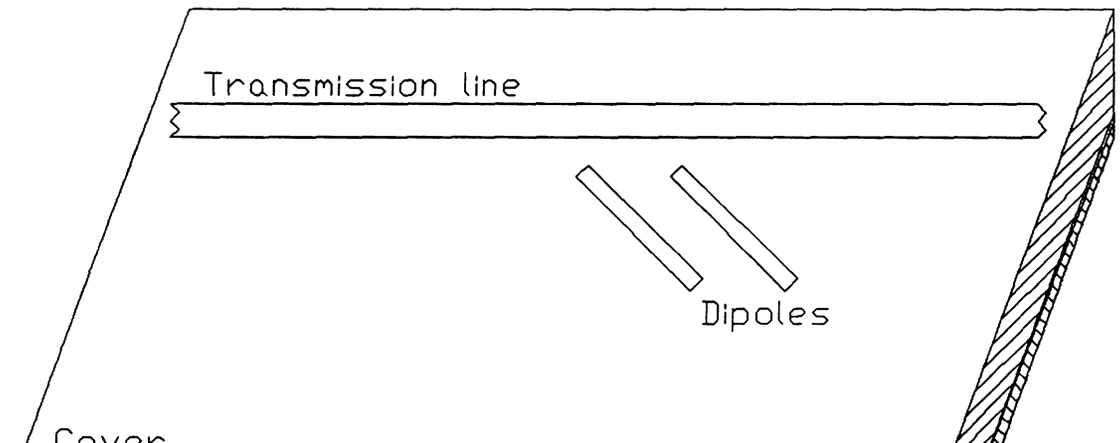

Figure 1.1: Typical microstrip system consisting of transmission line and dipole elements.

integral

microst

consider

integrals

space ar

elements

evaluate

As a

here wh

efficienc

utilizatio

generally

and appr

approxim

The

electric

environm

included

inverse F

integrand

significan

evaluation

integral equations involving the conceptually exact Green's functions for the layered microstrip media. Recent efforts have concentrated on this approach [6-11], and considerable attention has been given to evaluation of the slowly convergent Sommerfeld integrals associated with the Green's functions [12-16]. This technique accounts for space and surface-wave radiation, dielectric loss, and mutual coupling among system elements. A disadvantage of this method is the long computation times needed to evaluate the Sommerfeld integrals, even with relatively efficient integration routines.

As an alternative to the above method, an integral-operator approach is presented here which involves the rigorous Green's functions in an efficient manner. This efficiency is due not to the specific integration scheme employed, but rather to the utilization of known characteristics of microstrip dipoles near resonance, which is generally the frequency regime of interest. Thus, the theory is built on an exact model, and approximations are made at a later stage in the problem. This contrasts with other approximate theories, which are not based on exact models.

The text is divided into seven chapters. Chapter 2 presents a derivation of the electric dyadic Green's function associated with the layered-background microstrip environment. This work was originally performed by Bagby and Nyquist [17], and is included here for completeness. The Green's dyad is in the form of a two-dimensional, inverse Fourier transform integral in the spectral plane. Singularities of the spectral integrand include branch-points and surface-wave poles (swp's), and the physical significance of these singularities is discussed, along with their implication to numerical evaluation of the Green's functions.

In C

electron

is an int

The SE

integrate

the devic

for the a

other ful

theoretic

transmiss

fundamer

SEM.

Coup

perturbati

coupled r

intended

found to

two-dipol

The d

presented

isolated an

chapter, a

In Chapter 3, the steady-state singularity expansion method (SEM) for integrated electronics is presented. This method, based on the SEM for transient scattering [18-20], is an integral-operator description of currents induced on conducting integrated devices. The SEM evolves from the fundamental electric field integral equation (EFIE) for integrated electronics, thus it inherently includes all loss mechanism associated with both the device and the layered surround. It is found to be a computationally efficient method for the analysis of integrated devices, yielding results which agree with experiment and other full-wave methods. These other methods are presented in Chapter 4, along with theoretical and experimental results for the example of a dipole fed by a nearby transmission line. Two different method of moments (MoM) solutions to the fundamental EFIE are developed, which are used in part to validate the approximate SEM.

Coupled systems of devices are considered in Chapter 5. An approximate perturbation theory for coupled devices is presented, and applied to the problem of coupled microstrip dipoles. A full-wave MoM solution is also developed, which is intended to provide a comparison to the approximate theory. Theoretical results were found to agree with measurements made to identify the system-mode resonances of a two-dipole system.

The description of the experimental methods used in the course of this research is presented in Chapter 6. Measurements were made to quantify the EM properties of both isolated and coupled microstrip dipoles. Some experimental results are presented in this chapter, although most are dispersed throughout the text where appropriate. Finally,

some general conclusions and recommendations for future work are provided in Chapter 7.

Throughout this dissertation, vectors will appear overstruck with a single arrow, dyads with a double arrow. The assumptions that:

(1) All media are linear, isotropic, and non-magnetic
(2) The time dependance is harmonic ($e^{j\omega t}$) and is suppressed

lead to Maxwell's equations in M-K-S units as

$$\nabla\cdot\epsilon^{*}\vec{E} = \rho \tag{1a}$$

$$\nabla\cdot\vec{H} = 0 \tag{1b}$$

$$\nabla\times\vec{E} = -j\omega\mu\vec{H} \tag{1c}$$

$$\nabla\times\vec{H} = \vec{J}+j\omega\epsilon^{*}\vec{E}. \tag{1d}$$

Lastly, the term "device" is used throughout this dissertation, and refers to an arbitrarily shaped conductor embedded in the layered surround. The techniques presented here are sufficiently general to be applicable to a wide variety of shapes, although the specific class of narrow, conducting dipoles or resonators are considered as examples.

2.1 In

In th

Fields in

expressed

of electro

analysis.

The r

who addr

propagatio

fields due

were high

class of i

integrals r

found in B

In Sec

CHAPTER TWO

ELECTROMAGNETICS OF PLANARLY LAYERED MEDIA

2.1 INTRODUCTION

In this chapter, the electromagnetics of planarly layered media are investigated. Fields in the layered environment are obtained as Fourier transform integrals, and are expressed in dyadic notation. This formulation provides a conceptually exact description of electromagnetic interactions in layered media, and will form the basis of all subsequent analysis.

The rigorous study of layered media problems began in 1909 with Sommerfeld [21], who addressed the problem of the lossy half-space. His intention was to study wave propagation along the earth's surface, using integral-transform techniques to obtain the fields due to radiating elements above the earth-air interface. The resultant integrals were highly oscillatory and slowly convergent, and have formed the generic basis for a class of integrals known as "Sommerfeld integrals". Efficient evaluation of these integrals remains an active research area today [12-16]. A good historical overview is found in Baños [22].

In Section 2.2 the field equations are formulated by expressing the electric and

magneti

volume

are deve

bottom

circuit e

The

dyad. I

Green's

this matt

depends

[23]. Th

theorem,

The la

Fourier t

transform

singularit

discussed

2.2 El

The E

derivation

magnetic fields in terms of a Hertz potential, $\vec{\Pi}$. This potential is in the form of a volume integral of a dyadic Green's function and a current density. The field equations are developed for a general tri-layered environment, as shown in Figure 2.1. Later, the bottom layer will become conducting, forming the typical microstrip\millimeter-wave circuit environment.

The next section address the problem of the source-point singularity of the Green's dyad. It is well-known that great care must be exercised when forming the electric Green's dyad in regions where the source and observation points coincide. In the past, this matter caused some confusion since the principal value of the integral in question depends critically on the shape of the infinitesimal singularity excluding volume used [23]. The Green's function is, of course, unique, which is required by the uniqueness theorem, and is derived in this section.

The last section address the various singularities encountered in the complex spectral Fourier transform space, knowledge of which are necessary to compute the inverse transform integrals. These consist of surface-wave poles (swp's) and branch-point singularities of the spectral integrand. The physical significance of these singularities is discussed, as well as their implication to numerical evaluation of the field quantities.

2.2 ELECTRIC HERTZIAN POTENTIAL DYADIC GREEN'S FUNCTION

The Hertzian potential dyadic Green's function is formulated in this section. The derivation is based on the classical development of Sommerfeld [24], utilizing Fourier

transfo

Nyquis

of the

typical

Co

is imm

environ

and cov

y norma

isotropic

for i=s,

i and j is

$k_i=n_ik_0$

The

cover re

layer, as

to a field

arrives at

total pote

potential

potential

transform techniques. This Green's function was originally developed by Bagby and Nyquist [17], and is valid for arbitrary tri-layered media. Subsequent to development of the general Green's function, media for $y<-t$ will become conducting, forming the typical microstrip\millimeter-wave environment.

Consider the layered environment shown in Figure 2.1. Electric current density $\vec{J}$ is immersed in the cover region of a tri-layered substrate/film/cover background environment. The film layer of thickness t is embedded between unbounded substrate and cover layers. The origin of coordinates is chosen at the film/cover interface, with y normal and x,z tangential to that interface. Each layer is assumed to be linear, isotropic, and homogeneous, with dielectric and magnetic properties $\epsilon_i=n^2_i\epsilon_0$ and $\mu_i=\mu_0$ for i=s,f,c, where n_i is the electric refractive index. The electric contrast between layer i and j is given by $N_{ji}=n_j/n_i$. The wavenumber and intrinsic impedance of each layer are $k_i=n_ik_0$ and $\eta_i=\eta_0/n_i$, where (k_0,η_0) are their free-space counterparts.

The impressed current $\vec{J}$ (or an impressed polarization $\vec{P}=\vec{J}/j\omega$) radiates into the cover region of the multilayered structure, generating electric Hertzian potential in each layer, as shown in Figure 2.2. The primary potential propagates directly from the source to a field point in the cover layer, and the scattered potential (reflected or transmitted) arrives at a field point after being scattered from interfaces between adjacent layers. The total potential in the cover layer is the sum of a primary potential $\vec{\Pi}^p$ and a scattered potential $\vec{\Pi}^s$. In the $i\neq c$ layer there is just a scattered potential. All components of potential satisfy the Helmholtz equations (A.7)

y=0

y=-t

Su

Figure 2.

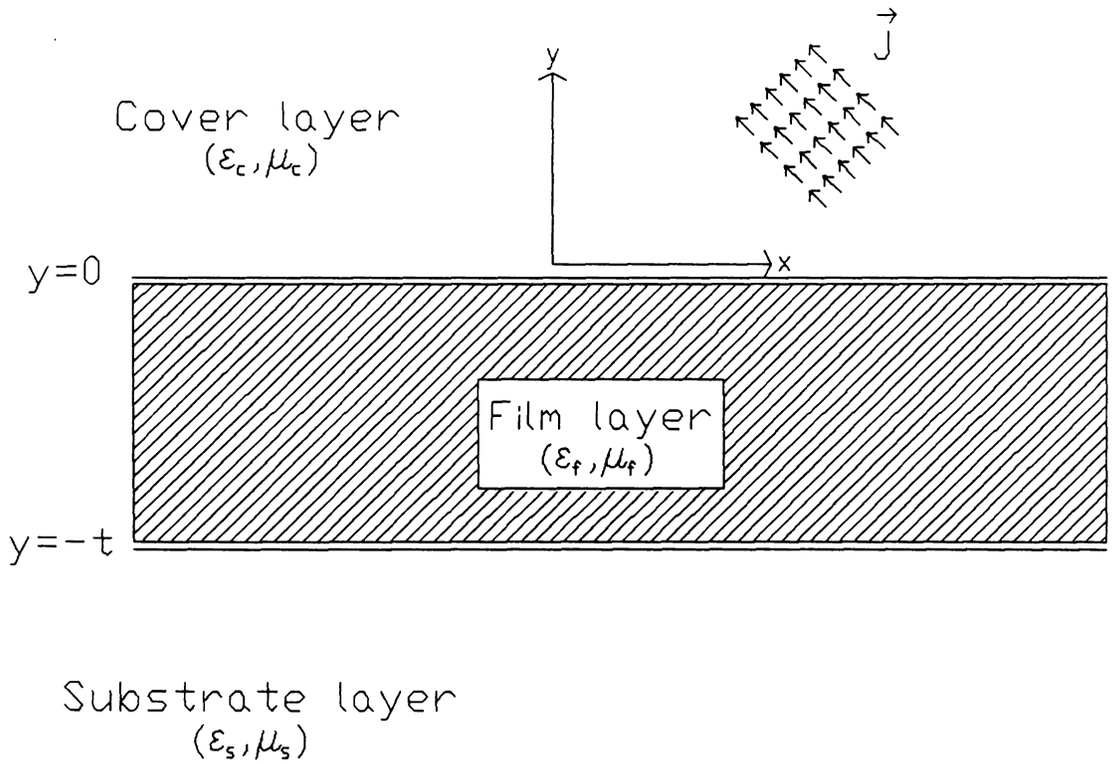

Figure 2.1: Tri-layered background environment for integrated electronics.

y=0

y=-t

Figure 2.

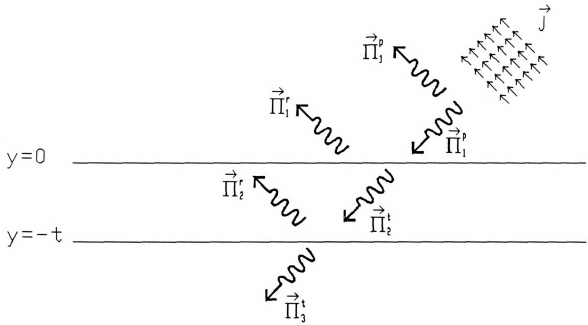

Figure 2.2: Principal and scattered electric Hertzian potential components.

as derive

as a supe

will be s

2.2.1 Pl

The pri

unbounde

point. T

where

is the far

distance f

makes it c

$$(\nabla^2 + k_i^2)\begin{Bmatrix} \vec{\Pi}_i^p \\ \vec{\Pi}_i^s \end{Bmatrix} = \begin{cases} -\vec{J}/j\omega\epsilon_i & i=c \\ 0 & all\ i. \end{cases} \quad (1)$$

as derived in Appendix A. A solution for the total potential in any region can be written as a superposition of Hertzian potentials. A solution for the total potential of the form

$$\vec{\Pi}(\vec{r}) = \int_V \ddot{G}(\vec{r}|\vec{r}') \cdot \frac{\vec{J}(\vec{r}')}{j\omega\epsilon} dV' \quad (2)$$

will be sought, where $\ddot{G}(\vec{r}|\vec{r}')$ is the dyadic Green's function to be determined.

2.2.1 PRIMARY GREEN'S COMPONENT

The primary wave of potential corresponds to the potential generated by a source in an unbounded homogeneous medium, which propagates directly from source point to field point. This potential can be written for the cover region as [25]

$$\vec{\Pi}_c^p(\vec{r}) = \int_V G^p(\vec{r}|\vec{r}') \frac{\vec{J}(\vec{r}')}{j\omega\epsilon_c} dV' \quad (3)$$

where

$$G^p(\vec{r}|\vec{r}') = \frac{e^{-jk_c|\vec{r}-\vec{r}'|}}{4\pi|\vec{r}-\vec{r}'|} \quad (4)$$

is the familiar free-space Green's function in spatial form. The quantity $|\vec{r}-\vec{r}'|$ is the distance from a source point at $\vec{r}'$ to a field point $\vec{r}$. The presence of this quantity makes it difficult or impossible to analytically integrate G^p into other functions, which

will be

for G^p

variable

The

as

where

Wavenu

between

is well-k

uniquene

It sh

spatial re

slowly co

but also t

will be required to perform a numerical solution. An alternate spectral representation for G^p is developed in Appendix B, which has a simple dependence on the spatial variables x,y,z, thus facilitating the numerical solution for $\vec{\Pi}$.

The spectral representation for the principal Green's dyad is found in Appendix B as

$$G^p(\vec{r}|\vec{r}') = \iint_{-\infty}^{\infty} \frac{e^{j\vec{\lambda}\cdot(\vec{r}-\vec{r}')}\, e^{-p_c|y-y'|}}{2(2\pi)^2 p_c} d^2\lambda. \tag{5}$$

where $\vec{\lambda} = \hat{x}\xi + \hat{z}\zeta$ is a 2-D spatial frequency with $\lambda^2 = \xi^2 + \zeta^2$ and $d^2\lambda = d\xi d\zeta$. Wavenumber parameters are $p_i = \sqrt{\lambda^2 - k_i^2}$ with $Re\{p_i\} > 0$ for i=s,f,c. The equivalence between the spectral and spatial forms,

$$\frac{e^{-jk_c|\vec{r}-\vec{r}'|}}{4\pi|\vec{r}-\vec{r}'|} = \iint_{-\infty}^{\infty} \frac{e^{j\vec{\lambda}\cdot(\vec{r}-\vec{r}')}\, e^{-p_c|y-y'|}}{2(2\pi)^2 p_c} d^2\lambda$$

is well-known as the Weyl identity [26], and can be confirmed by direct integration or uniqueness arguments.

It should be noted that the source point singularity at $\vec{r} = \vec{r}'$, which is obvious in the spatial representation, is still contained in (5). As $\vec{r} \to \vec{r}'$, equation (5) becomes very slowly convergent. This is due not only to the loss of the exponential decay as $y \to y'$, but also to the loss of the oscillatory nature of the integrand as $x,z \to x',z'$. For $\vec{r} = \vec{r}'$,

which is

present

2.2.2 R

Equat

variables

y, to allo

Fourier t

where $\bar{\lambda}$

Equation

where th

$$G^p(\vec{r}=\vec{r}') \rightarrow \frac{1}{2(2\pi)^2} \int\int_{-\infty}^{\infty} \frac{d^2\lambda}{\lambda}$$

which is a divergent integral. Therefore, the source-point singularity of $O(1/|\vec{r}-\vec{r}'|)$ present in the spatial form corresponds to non-convergence of the spectral integral.

2.2.2 REFLECTED GREEN'S DYAD FOR SOURCES IN THE COVER

Equation (1) is solved for the scattered potential by Fourier transforming on spatial variables tangential to the layer interfaces. This will preserve the normal spatial variable y, to allow implementation of the appropriate boundary conditions. A two-dimensional Fourier transform pair is defined as

$$\vec{\Pi}(\vec{r}) = \frac{1}{(2\pi)^2} \int\int_{-\infty}^{\infty} \vec{\Lambda}(\vec{\lambda},y) e^{+j\vec{\lambda}\cdot\vec{r}} \, d^2\lambda \tag{6}$$

$$\vec{\Lambda}(\vec{\lambda},y) = \int\int_{-\infty}^{\infty} \vec{\Pi}(\vec{r}) e^{-j\vec{\lambda}\cdot\vec{r}} dxdz$$

where $\vec{\lambda} = \hat{x}\xi + \hat{z}\zeta$. Operation of the Fourier transform on equation (1) results in

$$\left(\frac{\partial^2}{\partial y^2} - p_i^2\right) \vec{\Lambda}_i^s(\vec{\lambda},y) = 0. \tag{7}$$

Equation (7) has solutions

$$\vec{\Lambda}_i^s(\vec{\lambda},y) = \vec{W}_i^s(\vec{\lambda}) e^{\pm p_i y} \tag{8}$$

where the coefficient $\vec{W}_i^s$ is determined by application of the appropriate boundary

conditio

The corr

bounded

Desi

the total

potential

as showr

$\bar{\Pi}_1$

where tl

impleme

The

In a manu

The total

conditions, derived in Appendix C. Substitution of (8) into (6) results in

$$\vec{\Pi}_i^e(\vec{r}) = \int\int_{-\infty}^{\infty} \frac{\vec{W}_i^s(\vec{\lambda})}{(2\pi)^2} e^{j\vec{\lambda}\cdot\vec{r}} e^{\mp p_i(\lambda)y} d^2\lambda. \tag{9}$$

The correct branch of $p_i(\lambda)$ must be chosen to yield spectral components which remain bounded and propagate outward as $y \to \pm\infty$. This will be discussed in Section (2.4.1).

Designating the cover, film, and substrate layers as regions 1, 2, and 3, respectively, the total potential in region (1) is found as the sum of a principal potential and a reflected potential,

$$\vec{\Pi}_1(\vec{r}) = \vec{\Pi}_1^p(\vec{r}) + \vec{\Pi}_1^r(\vec{r}) \tag{10}$$

as shown in Figure (2.2). Using (5) and (9), equation (10) may be written as

$$\vec{\Pi}_1(\vec{r}) = \frac{1}{(2\pi)^2} \int\int_{-\infty}^{\infty} e^{j\vec{\lambda}\cdot\vec{r}} \left[\int_V \frac{\vec{J}}{j\omega\epsilon_1} \frac{e^{-j\vec{\lambda}\cdot\vec{r}'} e^{-p_1(\lambda)|y-y'|}}{2p_1(\lambda)} dV' + \vec{W}_1^r(\vec{\lambda}) e^{-p_1(\lambda)y} \right] d^2\lambda \tag{11}$$

where the spatial and spectral integrations have been interchanged to facilitate implementation of the boundary conditions.

The total potential in region (2) is the sum of a transmitted and a reflected potential,

$$\vec{\Pi}_2(\vec{r}) = \vec{\Pi}_2^t(\vec{r}) + \vec{\Pi}_2^r(\vec{r}). \tag{12}$$

In a manner similar to (10), equation (12) may be written as

$$\vec{\Pi}_2(\vec{r}) = \frac{1}{(2\pi)^2} \int\int_{-\infty}^{\infty} e^{j\vec{\lambda}\cdot\vec{r}} \left[\vec{W}_2^t(\vec{\lambda}) e^{p_2(\lambda)y} + \vec{W}_2^r(\vec{\lambda}) e^{-p_2(\lambda)y} \right] d^2\lambda. \tag{13}$$

The total potential in region (3) consists of only a transmitted wave,

where

Ap

is quite

specializ

environ

where th

The prin

where

$$\vec{\Pi}_3(\vec{r}) = \vec{\Pi}_3^r(\vec{r}) \tag{14}$$

where

$$\vec{\Pi}_3(\vec{r}) = \frac{1}{(2\pi)^2}\int\int_{-\infty}^{\infty} e^{j\vec{\lambda}\cdot\vec{r}}\left[\ \vec{W}_3^r(\vec{\lambda})e^{p_3(\lambda)y}\ \right] d^2\lambda. \tag{15}$$

Application of the appropriate boundary conditions to determine the various $\vec{W}_i^s$'s is quite tedious, and is summarized in Appendix C. Also in Appendix C, the specialization $Im\{n_s\}\to\infty$ is implemented, resulting in the desired cover/film/conductor environment. The resulting potential in the cover region is given by

$$\vec{\Pi}_1(\vec{r}) = -\frac{j\eta_c}{k_c}\int_V \ddot{G}(\vec{r}|\vec{r}')\cdot\vec{J}(\vec{r}')dV' \tag{16}$$

where the Green's dyad is

$$\ddot{G}(\vec{r}|\vec{r}') = \ddot{G}^p(\vec{r}|\vec{r}') + \ddot{G}^r(\vec{r}|\vec{r}').$$

The principal and reflected components may be decomposed as

$$\ddot{G}^p(\vec{r}|\vec{r}') = \ddot{I}G^p(\vec{r}|\vec{r}')$$

$$\ddot{G}^r(\vec{r}|\vec{r}') = \hat{x}\ G_t^r\hat{x} + \hat{y}\left[\frac{\partial G_c^r}{\partial x}\hat{x} + G_n^r\hat{y} + \frac{\partial G_c^r}{\partial z}\hat{z}\right] + \hat{z}\ G_t^r\ \hat{z}$$

where

The

maintain

potential

of poten

$C(\lambda)$ ar

where

Pole sing

of Z^{λ} ar

$$G^p(\vec{r}|\vec{r}') = \int\int_{-\infty}^{\infty} \frac{e^{j\vec{\lambda}\cdot(\vec{r}-\vec{r}')}\, e^{-p_c|y-y'|}}{2(2\pi)^2 p_c} d^2\lambda$$

$$\begin{Bmatrix} G_t^r(\vec{r}|\vec{r}') \\ G_n^r(\vec{r}|\vec{r}') \\ G_c^r(\vec{r}|\vec{r}') \end{Bmatrix} = \int\int_{-\infty}^{\infty} \begin{Bmatrix} R_t(\lambda) \\ R_n(\lambda) \\ C(\lambda) \end{Bmatrix} \frac{e^{j\vec{\lambda}\cdot(\vec{r}-\vec{r}')} e^{-p_c(y+y')}}{2(2\pi)^2 p_c} d^2\lambda. \tag{17}$$

The reflected Green's component G_t^r yields tangential components of potential maintained by tangential components of current, while G_n^r yields normal components of potential maintained by normal components of current and G_c^r gives normal components of potential coupled to tangential components of current. Coefficients $R_t(\lambda)$, $R_n(\lambda)$, and $C(\lambda)$ are given in Appendix C as

$$\begin{aligned} R_t(\lambda) &= \frac{N_1(\lambda)}{Z^h(\lambda)}, \qquad R_n(\lambda) = \frac{N_2(\lambda)}{Z^e(\lambda)} \\ C(\lambda) &= \frac{2(N_{fc}^2 - 1)p_c}{Z^h(\lambda) Z^e(\lambda)} \end{aligned} \tag{18}$$

where

$$\begin{aligned} N_1(\lambda) &= p_c - p_f \coth(p_f t) \\ N_2(\lambda) &= N_{fc}^2 p_c - p_f \tanh(p_f t) \\ Z^e(\lambda) &= N_{fc}^2 p_c + p_f \tanh(p_f t) \\ Z^h(\lambda) &= p_c + p_f \coth(p_f t). \end{aligned} \tag{19}$$

Pole singularities of the reflection and coupling coefficients, associated with the vanishing of Z^h and Z^e, lead to surface waves excited along the layered background environment.

These w

2.3 ELE

The e

quantity f

is given i

It is desir

potential

where $\ddot{G}$

as it; 1)

manipulati

a numerica

integral re

These will be discussed further in Section (2.4.1).

2.3 ELECTRIC DYADIC GREEN'S FUNCTION

The electric field in the cover region, rather then the Hertzian potential, is the needed quantity for analyzing the electromagnetics of the layered environment. This relationship is given in Appendix A, and with (16) becomes

$$\vec{E}(\vec{r}) = \frac{-j\eta_c}{k_c}(k_c^2 + \nabla\nabla\cdot)\int_V \ddot{G}(\vec{r}|\vec{r}')\cdot\vec{J}(\vec{r}')\,dV'. \tag{20}$$

It is desired to pass spatial derivatives under the spatial integral found in the Hertzian potential to obtain

$$\vec{E}(\vec{r}) = \frac{-j\eta_c}{k_c}\int_V \ddot{G}^{\epsilon}(\vec{r}|\vec{r}')\cdot\vec{J}(\vec{r}')\,dV' \tag{21}$$

where $\ddot{G}^{\epsilon}(\vec{r}|\vec{r}')$ is an electric dyadic Green's function. Representation (21) is desirable as it; 1) provides a compact notation for the electric field amenable to algebraic manipulations, and 2) allows implementation of the spatial derivatives analytically before a numerical solution is undertaken. Passage of these spatial derivatives under the spatial integral requires special care, which is the subject of this section.

2.3.1 S

The el

$\vec{G}(\vec{r}|\vec{r}')$

under th

be conti

Green's

of the a

arising f

can be h

incorpor

The

given by

The third

invoking

2.3.1 SOURCE-POINT SINGULARITY OF THE ELECTRIC GREEN'S DYAD

The electric field in the cover is recovered from the Hertzian potential as (20) where $\ddot{G}(\vec{r}|\vec{r}')$ is given by (17). It is desired to pass the spatial differential operator $\nabla\nabla\cdot$ under the volume integral in (20). This requires that the integrand of the volume integral be continuous with continuous second derivatives [27]. The reflected components of the Green's dyad posses this property, but the principal component does not. The presence of the absolute value function $|y-y'|$ in (4,5) gives rise to a source-point singularity arising from derivatives with respect to the normal coordinate variable. This situation can be handled by defining the spatial integral in a principal value (P.V.) sense, and incorporating an appropriate correction term [23].

The electric field in the cover region, which contains electric current sources, is given by (20), rewritten as

$$\begin{aligned}\vec{E}(\vec{r}) \;=\; & \frac{-j\eta_c}{k_c}(k_c^2+\nabla\nabla\cdot)\int_V \ddot{G}^r\cdot\vec{J}(\vec{r}')\,dV' \\ & -j\eta_c k_c\int_V \ddot{I}G^p\cdot\vec{J}(\vec{r}')\,dV' \\ & \frac{-j\eta_c}{k_c}\nabla\nabla\cdot\int_V \ddot{I}G^p\cdot\vec{J}(\vec{r}')\,dV'.\end{aligned} \tag{22}$$

The third term in (22) demands careful attention. It can be properly evaluated by invoking Leibnitz's rule, and excluding a specific principal volume [28], ie.;

$$\nabla\nabla\cdot\int_V \ddot{G}^p\cdot\vec{J}(\vec{r}')\,dV' \;=\; P.V.\int_V \nabla\nabla\cdot\ddot{G}^p\cdot\vec{J}(\vec{r}')\,dV' \;+\; \ddot{L}\delta(\vec{r}-\vec{r}')$$

where P

and P.V

dyad, wh

for the to

above, th

where

As

tangential

2.4 A
E

The

integrals

oscillatory

is used to

undertake

where P.V. designates evaluating the integration in a principal value sense,

$$P.V.\int_V \{\cdots\}\,dV' = \lim_{v_\delta \to 0} \int_{V-V_\delta} \{\cdots\}\,dV'$$

and P.V. is a shape dependant principal value. The term $\ddot{L}\delta(\vec{r}-\vec{r}')$ is a depolarizing dyad, which is dependent on the specific principal volume used. It should be noted that for the topic of this work, a slice principal volume is naturally assumed [28]. With the above, the electric field may be written as

$$\vec{E}(\vec{r}) = \frac{-j\eta_c}{k_c}\int_V \ddot{G}^e(\vec{r}|\vec{r}')\cdot\vec{J}(\vec{r}')\,dV' \tag{23}$$

where

$$\ddot{G}^e(\vec{r}|\vec{r}') = P.V.(k_c^2 + \nabla\nabla\cdot)\ddot{G}(\vec{r}|\vec{r}') + \ddot{L}\delta(\vec{r}-\vec{r}'). \tag{24}$$

As will be seen later, the depolarizing dyad $\ddot{L}=\hat{y}\hat{y}$ is never required, as only tangential current components are needed to describe the desired interactions.

2.4 ANALYTICAL AND NUMERICAL CONSIDERATIONS IN THE EVALUATION OF THE GREEN'S DYAD

The Green's dyad components given by (17) are generally known as Sommerfeld integrals [24], which are notoriously difficult to compute. In general, they exhibit very oscillatory, slowly convergent behavior. Typically, the Method of Moments (MoM) [29] is used to solve the equations associated with these dyads. The type of MoM solution undertaken, such as the use of Galerkin's method or the type of expansion or testing

function chosen, will greatly effect the accuracy and speed of obtaining a solution. This topic is discussed in Chapter 4, after the relevant equations are formulated. In this and the following sections, the singularities inherently present in the integrands of the Sommerfeld integrals are discussed. These singularities are in the form of poles and branch points in the complex λ-plane, as shown in Figure 2.3, and each is associated with physical phenomena. Knowledge of these singularities, and their physical significance, is paramount to accurate evaluation of these integrals.

2.4.1 SPECTRAL SINGULARITIES OF THE GREEN'S DYAD

Spectral singularities of the Green's dyad are poles and branch points in the complex λ-plane. Accurate determination of the location of these singularities is possible, and allows for determination of the correct inversion contour when evaluating the inverse transform (spectral) integrals.

Pole singularities occur in the reflection and coupling coefficients given by (18). Physically, these poles correspond to surface waves launched in the background dielectric layering. There is no pole associated with the principal Green's component, since this is the solution for a homogeneous medium.

Under the assumption that the background environment has limitingly small loss, the pole singularities are located in quadrants two and four, infinitesimally close to the real-λ axis. Representative pole locations are shown in Figure 2.3. Ignoring branch points for the moment, Figure 2.4 depicts the complex-λ plane with pole singularities $p_0, p_1, \ldots p_N$.

Implied

numerica

at $\pm\infty$ l

that the p

inversion

Cauchy-

have no

Tran

leading t

where κ

is also th

waveguid

Tran

and the r

Equation

symmetri

least one

Implied inversion contour C_r is shown slightly offset from the real-λ axis, to avoid numerical instabilities near the surface-wave poles. By closing the original contour C_r at $\pm\infty$ by a semicircle of infinite radius, and invoking the residue theorem, it is seen that the poles contribute a discrete field component from each residue. Equivalently, the inversion contour may be deformed around the pole singularities to allow use of the Cauchy-Goursat theorem [30]. The integration along the infinite semicircle is found to have no contribution, by proper choice of the branch cuts, as discussed later.

Transverse electric (TE) surface waves are associated with the vanishing of $Z^h(\lambda)$, leading to the eigenvalue equation

$$\tan(\kappa t) = -\frac{\kappa}{p_c} \tag{25}$$

where $\kappa = -jp_c$ is a commonly defined wave parameter for the film region. Equation (25) is also the eigenvalue equation for TE-odd surface-wave modes of the symmetric slab waveguide [31], which exhibit a low-frequency cutoff.

Transverse magnetic (TM) surface waves are associated with the vanishing of $Z^e(\lambda)$, and the resulting eigenvalue equation

$$\tan(\kappa t) = N_{fc}^2 \frac{p_c}{\kappa}. \tag{26}$$

Equation (26) is the eigenvalue equation for even TM surface-wave modes of the symmetric slab waveguide. These modes do not have a low-frequency cutoff, and so at least one pole singularity will always be present in the complex λ-plane. The cutoff

Figure 2.

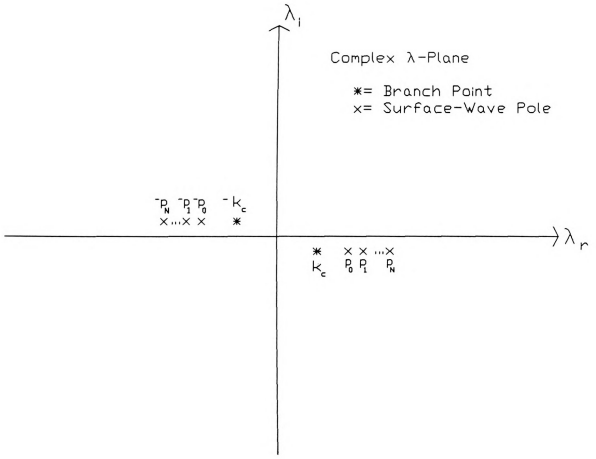

Figure 2.3: Complex lambda-plane singularities of the Green's dyad components.

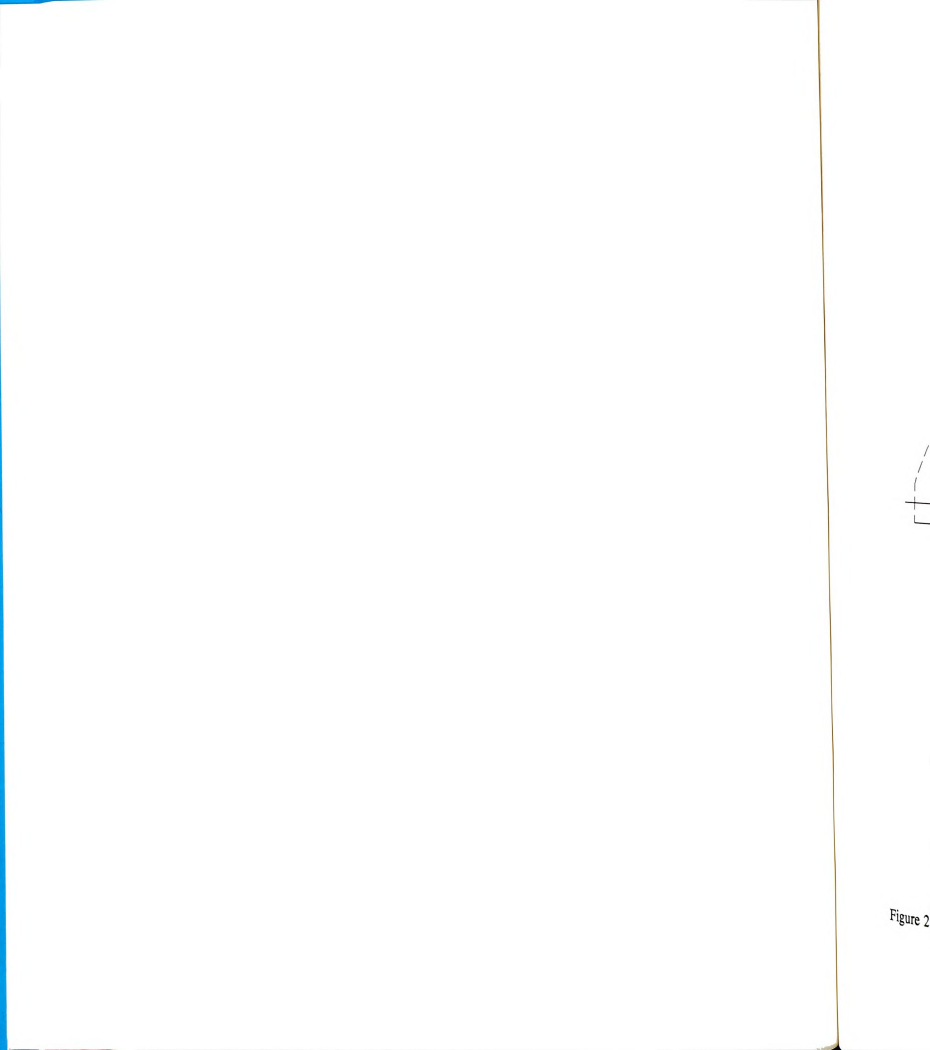

Figure 2

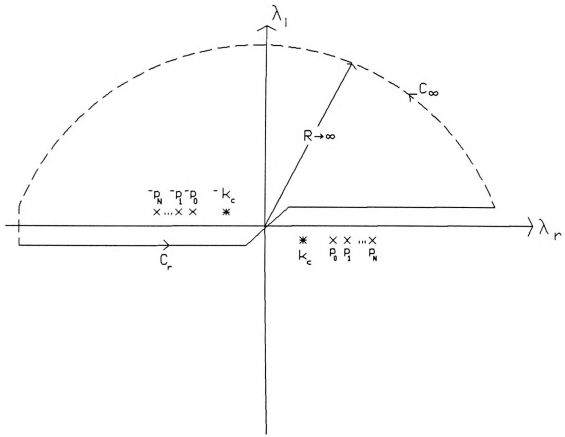

Figure 2.4: Complex lambda-plane with integration contour.

conditio

where t
will exi
and cov
suppres
conduct
usually
techniqu

The
loss, as
nearby c
to the sp

The
points.
$P_c(\lambda)$ ar
point sin
structure
examina

only the

condition for the n^{th} TM or TE, even/odd surface-wave mode is given by

$$\frac{2t}{\lambda_0} = \frac{n}{2\sqrt{n_f^2 - n_c^2}} \tag{27}$$

where t is the film thickness. Note that whether or not a particular surface-wave mode will exist depends on the frequency, film thickness, and indices of refraction of the film and cover. With the exception of the TM_0 mode, these parameters may be chosen to suppress or initiate a particular surface-wave mode. For the present discussion of conductor-based microstrip or millimeter wave circuits, these surface-wave modes are usually viewed as undesirable, although they form the basis of dielectric waveguiding techniques.

The main physical consequence of surface-waves is that they are a source of power loss, as they carry energy away from the circuit. These waves may couple to other nearby circuits, complicating circuit/system analysis. Numerically, they contribute poles to the spectral integrals, complicating their evaluation.

The second type of singularities inherent in the Sommerfeld integrals are branch points. Branch points arise from the multivalued nature of wavenumber parameters $p_c(\lambda)$ and $p_f(\lambda)$, resulting in a sign ambiguity. It can be shown in general that branch point singularities are only associated with the outer layers of a multilayered dielectric structure [25, p. 112]. For the specific example of the tri-layered structure studied here, examination of the spectral integrands revel that they are even functions of p_f. Hence, only the branch points at $\lambda = \pm k_c$ are of consequence.

Generally, physical constraints indicate which branch of the function to use. For problems involving real frequencies and lossy or limitingly low-loss materials, the branch points are below the positive real-λ axis, as shown in Figure 2.3. This can be seen by considering the cover wavenumber to be $k_c = k_c' - jk_c''$ where $k_c'' > 0$. Requiring waves to decay and propagate outward from a source point necessitates $Re\{p_c\} > 0$ and $Im\{P_c\} > 0$, to be consistent with exponential factors of the form $e^{-p_c y}$. This leads to the standard hyperbolic branch cuts [31], which separate the proper and improper Riemann sheets, and are depicted in Figure 2.5. Also shown in Figure 2.5 is the implied integral inversion contour , which is along the real-λ axis or may be deformed into the complex-λ plane.

When considering resonant phenomena, the frequency must become complex with positive imaginary part to provide temporal decay consistent with the $e^{j\omega t}$ time dependance. This leads to a migration of the branch points and poles across the real-λ axis [32], since the imaginary part of k_c becomes positive for a low-loss cover. The branch cuts to separate the proper from improper sheets now become as shown in Figure 2.6. It has been found [33] that the integration path must cross the branch cuts. Alternately, physical reasoning would dictate that all quantities must change in a continuous manner as the migrating singularities cross the real-λ axis (which is also the implicit integral inversion contour for the non-resonant case). Since the original inversion contour is above the singularities, it should remain above the singularities as

they migrate across the real-λ axis, to keep all parameters changing in a continuous manner Chew [32]. These branch cuts are shown in Figure 2.7, along with the new inversion contour. The branch cuts shown in Figure 2.7 have been implemented in this work, and yield good numerical results.

2.4.2 INTEGRATION TECHNIQUES FOR THE EFFICIENT NUMERICAL EVALUATION OF THE GREEN'S DYAD

The Sommerfeld integrals associated with the Green's function for the layered media are difficult to compute, as evidenced by the large number of papers concerning this topic [12-16]. Their evaluation involves a double infinite integration, which is often transformed to a finite and an infinite integration by the transformation

$$\int_{-\infty}^{\infty}\int \{\cdots\}\, d^2\lambda \rightarrow \int_{0}^{\infty}\int_{0}^{2\pi} \{\cdots\}\, \lambda\, d\theta d\lambda \tag{28}$$

where

$$\begin{aligned} \xi &= \lambda\cos(\theta) \\ \zeta &= \lambda\sin(\theta) \\ \xi^2 + \zeta^2 &= \lambda^2. \end{aligned}$$

A possible problem with this formulation is that the finite integration becomes highly oscillatory with increasing λ. Alternatively, the integration may be preformed in rectangular coordinates [16]. This involves regarding the inner integral (over ξ) as some function of ζ, and tabulating that function for different values of ζ. Interpolation then provides the needed values when performing the outer integration, although numerically

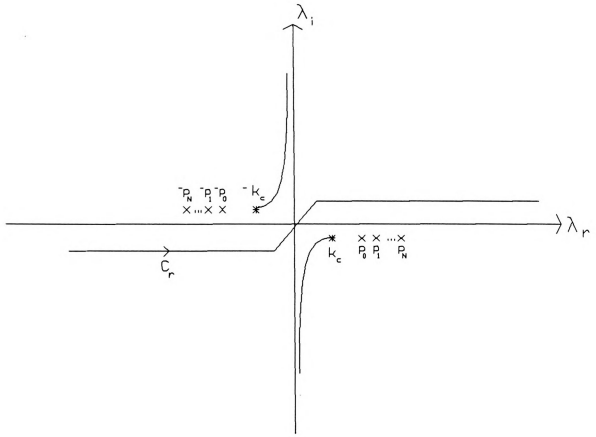

Figure 2.5: Branch cuts in the complex lambda-plane.

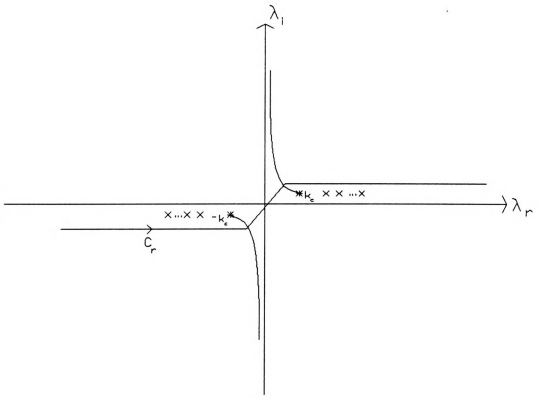

Figure 2.6: Proper branch cuts and the associated integration contour for studying resonant phenomena.

Figure 2.

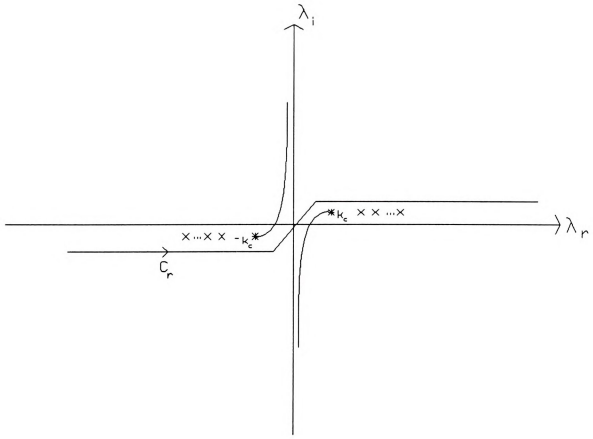

Figure 2.7: Alternative branch cuts for investigation of resonant phenomena.

it is mo

evaluati

where

is the fu

found th

approxir

integral.

The

(1990) a

integran

requiring

preferab

this worl

type of

it is more accurate to do a function approximation rather then an interpolation, since evaluation points may be chosen judiciously. This is illustrated by

$$I = \int_{\zeta} d\zeta \, f_1(\zeta) \int_{\xi} f_2(\zeta,\xi)\, d\xi = \int_{\zeta} f_1(\zeta) f_{2a}(\zeta) d\zeta$$

where

$$f_{2a}(\zeta) = \int_{\xi} f_2(\zeta,\xi) d\xi$$

is the function to be approximated. This scheme proves to be efficient because it is found that f_{2a} is a smooth function of ζ. As a result, once the function f_{2a} has been approximated, evaluating the integral I reduces to evaluation of a one-dimensional integral.

The method of performing the spectral integration in rectangular coordinates is new (1990) and is found to be very efficient and accurate. The oscillatory nature of the polar integrand is avoided in rectangular coordinates, leading to greater accuracy while requiring less evaluation time. There are, however, situations where the polar form is preferable. Both polar and rectangular integral formulations have been implemented for this work, and the question of which method to use has been found to depend on what type of MoM solution is being implemented. This is discussed further in Chapter 4.

2.5 SU

The

cover/fi

Hertzia

as

where

$\bar{G}(\bar{r}|\bar{r}')$

compon

Onc

where

forming

mathem

which p

source r

2.5 SUMMARY

The electric field induced by currents in the cover region of a tri-layered cover/film/conductor environment is formulated in terms of Hertzian potentials. All Hertzian potentials satisfy the vector Helmholtz equations (A.7), and can be expressed as

$$\vec{\Pi}(\vec{r}) = \int \ddot{G}(\vec{r}|\vec{r}') \cdot \frac{\vec{J}(\vec{r}')}{j\omega\epsilon} dV'$$

where $\ddot{G}(\vec{r}|\vec{r}')$ is a Green's dyad specific to the layered surround. Determination of $\ddot{G}(\vec{r}|\vec{r}')$ requires matching the appropriate boundary conditions (C.3), for potential components in each region.

Once the Hertzian potential is obtained, it is desired to form the electric field as

$$\vec{E}(\vec{r}) = \frac{-j\eta_c}{k_c} \int_V \ddot{G}^e(\vec{r}|\vec{r}') \cdot \vec{J}(\vec{r}') dV' \qquad (29)$$

where $\ddot{G}^e(\vec{r}|\vec{r}')$ is an electric dyadic Green's function. Care must be exercised when forming (29), as spatial derivatives must be passed through a spatial integral in a mathematically correct manner. This leads to a depolarizing dyad term, $\ddot{L}\delta(\vec{r}-\vec{r}')$, which provides the field with the correct value when the observation point is in the source region. The electric Green's dyad may be written as

where F
sense.

Cor
present
As well
the form
backgro
of the sp
loss and
with ra
paramou

$$\vec{G}^{e}(\vec{r}|\vec{r}') = P.V.(k_c^2 + \nabla\nabla\cdot)\vec{G}(\vec{r}|\vec{r}') + \vec{L}\delta(\vec{r} - \vec{r}')$$

where P.V. indicates that the spatial integration must be preformed in a principal value sense.

Components of the Green's dyad are in the form of Sommerfeld integrals, which present analytical and numerical difficulties to evaluation of the desired field quantities. As well as being oscillatory and slowly convergent, they possess spectral singularities in the form of poles and branch points. These singularities are associated with the layered background environment, and important physical significance is attached to them. Poles of the spectral integrand are associated with surface-waves which usually result in energy loss and undesirable coupling between circuit elements. Branch points are associated with radiation. Knowledge of the types and locations of these singularities is of paramount importance in evaluating the Green's dyad components.

3.1

In t
cover/fi
film lay
often ch
on the c

Inve
continue
technolo
similar s
[5-11] r
compreh
microstr

A w
mentione

CHAPTER THREE

THE SINGULARITY EXPANSION METHOD FOR INTEGRATED ELECTRONICS

3.1 INTRODUCTION

In this chapter, the analysis of a general conducting object placed in a tri-layered cover/film/conductor environment is investigated. The device is printed on the dielectric film layer, residing in the cover region, as shown in Figure 3.1. This type of object is often characterized as a microstrip antenna element or a microstrip resonator, depending on the desired application.

Investigation of the properties of this type of device started in the 1950's, and has continued through the present. A thorough survey of microstrip antenna element technology from its inception through 1981 is given by Carver and Mink [3], while a similar survey of microstrip array technology is found in Mailloux et al. [4]. References [5-11] refer to later papers on these subjects, although this list is by no means comprehensive. References [34-36] refer to papers treating the conducting objects as microstrip resonators.

A wide variety of mathematical techniques have been employed in the above mentioned works to analyze these devices. Rigorous methods involve utilizing the exact

Figure 3

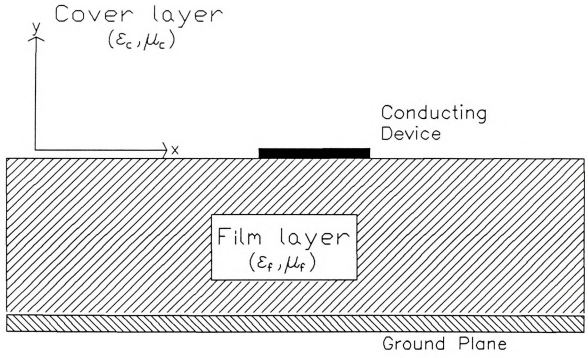

Figure 3.1: General conducting device embedded in a tri-layered conductor/film/cover environment.

Green's functions for the layered media, and result in conceptually exact descriptions of EM phenomena. These methods may be computationally inefficient, due to the presence of Sommerfeld integrals in the Green's functions. In this chapter, a mathematical model is described which involves the rigorous Green's functions in a numerically efficient manner.

In the next section, the fundamental electric field integral equation (EFIE) describing EM interactions in the layered environment is formulated. This equation is the starting point for the analysis to be presented in this chapter, as well as the basis for the well-established methods which will be used for comparison. The later methods are described in the next chapter.

In Section 3.3, the singularity expansion method (SEM) is presented, and applied to the fundamental EFIE. The motivation for representing the unknown device current as a sum of pole singularities is developed by considering the singularity expansion method for transient scattering from free-space objects. Natural resonant modes (or eigenmodes) are defined, which are characteristic of the device structure. Coupling coefficients are found which relate the device response to an impressed field for near-resonant frequencies. Later, it will be shown that results of the SEM agree with those of other techniques.

In Section 4, the SEM is applied to the specific example of a microstrip dipole excited by a nearby transmission line. The electric field of an isolated microstrip transmission line is found, and used as an approximation to the impressed electric field incident upon the dipole. The validity of approximating the impressed field by the

unpertur

detailed

wave m

3.2 I

In th

current

study of

Con

dipole,

impresse

perfectly

condition

$\hat{r}$ is a un

form of

unperturbed field of an isolated transmission line is assessed. The results of the SEM detailed in this chapter are presented in Chapter 4, along with results from other full-wave methods and measurement.

3.2 FORMATION OF THE ELECTRIC FIELD INTEGRAL EQUATION

In this section, the electric field integral equation (EFIE) for unknown device surface current $\vec{K}$ is formed. This equation is the fundamental integral-operator equation for the study of microstrip-based circuits.

Consider Figure 3.2, which shows a microstrip device, specifically a microstrip dipole, embedded within the tri-layered integrated electronics environment. An impressed source $\vec{J}$ maintains electric field $\vec{E}^i$, which excites surface currents on perfectly conducting device surface S, producing scattered field $\vec{E}^s$. The boundary condition for tangential $\vec{E}$ at conducting surface S requires that $\hat{t}\cdot(\vec{E}^i+\vec{E}^s)=0$, where $\hat{t}$ is a unit tangent vector at any point on surface S. Expressing scattered field $\vec{E}^s$ in the form of equation (2.20) leads to the EFIE for unknown current $\vec{K}$

$$\hat{t}\cdot(k_c+\nabla\nabla\cdot)\int_S \ddot{G}(\vec{r}|\vec{r}')\cdot\vec{K}(\vec{r}')\,dS' = -\frac{jk_c}{\eta_c}\hat{t}\cdot\vec{E}^i(\vec{r}) \;\ldots\; \forall\ \vec{r}\in S. \qquad (1)$$

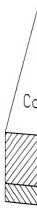

Figure

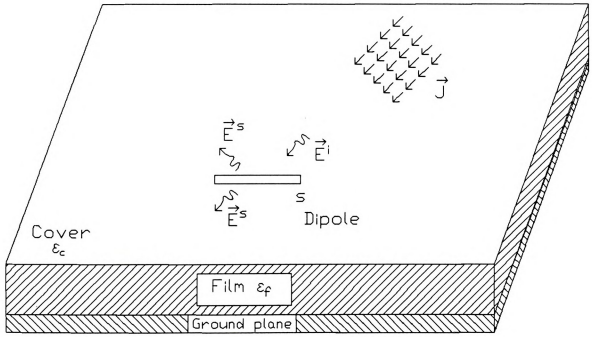

Figure 3.2: Microstrip device excited by an impressed source **J**.

Alternatively, the scattered field may be expressed in the form of equation (2.21), and the EFIE becomes

$$\hat{t}\cdot\int_S \vec{G}^e(\vec{r}|\vec{r}')\cdot\vec{K}(\vec{r}')dS' = -\frac{jk_c}{\eta_c}\hat{t}\cdot\vec{E}^i(\vec{r}) \;\ldots\; \forall\, \vec{r}\in S. \tag{2}$$

Equation (2) is useful for theoretical manipulations, whereas equation (1) is used for numerical computation.

3.3 SINGULARITY EXPANSION OF DEVICE CURRENTS

EFIE (2) is to be solved for unknown surface current $\vec{K}$. It is well-known that microstrip antenna and resonator elements exhibit very frequency selective responses. These devices interact strongly when excited at or near their resonant frequency, but have limited responses at other frequencies. This feature has initiated representing these devices as lossy cavities, and other physically insightful models.

Knowledge of the resonant characteristics of microstrip elements leads to the representation for the device surface current near resonance as

$$\vec{K}(\vec{r},\omega) \approx \frac{A_p\vec{k}_p(\vec{r})}{(\omega-\omega_p)^l} \tag{3}$$

where ω_p is a complex natural frequency, l is the order of the pole at $\omega=\omega_p$, $\vec{k}_p$ is the natural-mode current distribution associated with the pth natural-mode, and A_p is the amplitude of the pth natural mode. It will be shown later that the order of the pole

singularity is unity [37].

Equation (3) describes the surface current near a single resonant frequency. In order to describe the current over a wider frequency range, the current is represented as a sum of terms of the form of equation (3),

$$\vec{K}(\vec{r},\omega) \approx \sum_q \frac{A_q \vec{k}_q(\vec{r})}{(\omega - \omega_q)}. \qquad (4)$$

The representation for surface current (4) will be used in EFIE (2) to quantify complex natural-mode frequencies ω_q and their associated amplitudes A_q. Before proceeding, the motivation for surface current representation (4) should be placed in the proper context, which is the subject of the following section.

3.3.1 MOTIVATION OF CURRENT EXPANSION: THE TRANSIENT SINGULARITY EXPANSION METHOD

The transient singularity expansion method [18-20] was developed in the early 1970's as a method to characterize the response of a scatterer to a transient excitation. It was motivated by the observation that the transient response of an object appears to be dominated by a few temporally-damped sinusoids, which are characteristic of the size and shape of the responding structure. The Laplace transform of a damped sinusoid corresponds to pole pairs in the complex frequency plane, leading to the frequency-plane singularity representation for scatterer current.

The experimental observation of the time-domain, transient current response of a scatterer leads to

or equi

where

modal

where

This pr

for the

For

in the n

corresp

the stea

of pole-

$$\vec{K}(\vec{r},t) \approx \sum_{n=1}^{N} A_n \vec{k}_n(\vec{r})\, e^{\sigma_n t}\cos(\omega_n t + \phi_n) \tag{5}$$

or equivalently

$$\vec{K}(\vec{r},t) \approx \sum_{n=1}^{2N} a_n \vec{k}_n(\vec{r}) e^{s_n t} \tag{6}$$

where $s_n = \sigma_n + j\omega_n$ is the complex natural-mode frequency of the nth mode, and $\vec{k}_n$ is the modal distribution of current. Defining the bilateral Laplace transform pair [38]

$$f(t) = \frac{1}{2\pi j}\int_{\sigma-j\infty}^{\sigma+j\infty} F(s)e^{st}ds$$

$$F(s) = \int_{-\infty}^{\infty} f(t)e^{-st}dt$$

where $s = \sigma + j\omega$, equation (6) may be written in the complex frequency plane as

$$\vec{K}(\vec{r},s) \approx \sum_{n=1}^{2N} \frac{a_n \vec{k}_n(\vec{r})}{(s - s_n)}.$$

This provides the desired motivation for the frequency-plane, pole-singularity expansion for the surface current in the case of a transient excitation.

For excitations at a single frequency, the region of interest in the s-plane would be in the neighborhood of a single point. For sinusoidal steady-state excitations, only modes corresponding to poles near points $s = j\omega$ will be excited. Therein lies the motivation for the steady-state singularity expansion of current. Surface current (4) consists of a sum of pole-terms, which may be truncated after one or two terms to represent current for

excitations near a single frequency. Evaluation of one term of (4) is found to be an efficient representation for the device current near resonance, leading to results which agree with other methods.

It should be noted that, in general, the complex s-plane may contain singularities of $\vec{K}(\vec{r},s)$ other then simple poles. The time-domain current $\vec{K}(\vec{r},t)$ will then be expressed as a sum of contributions from poles, branch points, and possibly entire function singularities (singularities at infinity). It has been shown that for finite-sized objects in free-space, the object response has only poles as singularities. Other objects may require branch point and entire function singularities, as well as pole singularities. The present work concerns conducting objects placed in a non-homogeneous medium. It is shown in Appendix D that branch point singularities are present in the complex frequency plane, and relate to surface-wave propagation. Hence for a complete singularity expansion of frequency domain current $\vec{K}$, singularities other than just poles would be required. It will be shown, though, that (4) yields results that agree quite well with other more established methods in the resonance range, justifying its use.

3.3.2 DETERMINATION OF NATURAL MODES

In this section, the defining relation for natural modes is obtained. These modes are typically defined by the source-free solution to EFIE (1) or (2) ($\vec{E}^i = 0$). An alternative method is followed here [37], which provides more physical insight into the problem.

Singularity expansion (4) is substituted into EFIE (1), leading to

$$\sum_q \frac{A_q}{(\omega - \omega_q)} \hat{t} \cdot \int_S \vec{\vec{G}}^e(\vec{r}|\vec{r}') \cdot \vec{k}_q(\vec{r}') dS' \approx -\frac{jk_c}{\eta_c} \hat{t} \cdot \vec{E}^i(\vec{r}) \ \ldots \ \forall \ \vec{r} \in S. \tag{7}$$

For frequencies $\omega \approx \omega_p$, it is obvious that the p^{th} term in the sum (7) becomes unbounded. Since $\vec{E}^i$ is regular at these frequencies, the p^{th} integral term must vanish to produce an indeterminate form. Therefore, modal current distribution $\vec{k}_p$ must satisfy the homogeneous EFIE

$$\hat{t} \cdot \int_S \vec{\vec{G}}^e(\vec{r}|\vec{r}';\omega) \cdot \vec{k}_p(\vec{r}') dS' = 0 \ \ldots \ \forall \ \vec{r} \in S \tag{8}$$

with non-trivial solutions only for $\omega = \omega_p$. Equation (8) defines the p^{th} natural mode with complex natural frequency ω_p.

3.3.3 DETERMINATION OF EXCITATION AMPLITUDES

The excitation amplitude for natural-mode current, A_q, found in current expansion (4), relates the amplitude of the q^{th} natural mode to the impressed excitation. These amplitudes are determined from fundamental EFIE (2) and current expansion (4) upon invoking reciprocity of the Green's dyad kernel, $G^e_{\alpha\beta}(\vec{r}|\vec{r}') = G^e_{\beta\alpha}(\vec{r}'|\vec{r})$ [37].

The integral operator

which p

where r

$\omega = \omega_p$ l

The lea

Singular

leading

$$\int_S dS\ \vec{k}_p(\vec{r})\cdot\{\cdots\}$$

which performs the $\hat{t}\cdot\{\cdots\}$ operation, is applied to EFIE (2) yielding

$$\int_S dS'\ \vec{K}(\vec{r}')\cdot\int_S \vec{G}^{\,e}(\vec{r}'|\vec{r};\omega)\cdot\vec{k}_p(\vec{r})\,dS \;=\; -\frac{jk_c}{\eta_c}\int_S \vec{k}_p(\vec{r})\cdot\vec{E}^{\,i}(\vec{r})\,dS$$

where reciprocity of $\vec{G}^{\,e}$ has been invoked. Expanding $\vec{G}^{\,e}$ in a Taylor's series about $\omega=\omega_p$ leads to

$$\int_S dS'\ \vec{K}(\vec{r}')\cdot\int_S\left[\vec{G}^{\,e}(\vec{r}'|\vec{r},\omega_p)+\left.\frac{\partial\vec{G}^{\,e}(\vec{r}'|\vec{r};\omega)}{\partial\omega}\right|_{\omega=\omega_p}(\omega-\omega_p)\;+\;\cdots\right]\cdot\vec{k}_p(\vec{r})\,dS\;=$$
$$-\frac{jk_c}{\eta_c}\int_S \vec{k}_p(\vec{r})\cdot\vec{E}^{\,i}(\vec{r})\,dS.$$

The leading term vanishes due to (8), consequently

$$\int_S dS'\ \vec{K}(\vec{r}')\cdot\int_S\left[\left.\frac{\partial\vec{G}^{\,e}(\vec{r}'|\vec{r};\omega)}{\partial\omega}\right|_{\omega=\omega_p}(\omega-\omega_p)\;+\;\cdots\right]\cdot\vec{k}_p(\vec{r})\,dS\;=$$
$$-\frac{jk_c}{\eta_c}\int_S \vec{k}_p(\vec{r})\cdot\vec{E}^{\,i}(\vec{r})\,dS.$$

Singularity expansion (4), with poles of arbitrary order l_q, is exploited in the above, leading to

$$\sum_q\frac{A_q}{(\omega-\omega_q)^{l_q}}\int_S dS'\ \vec{k}_q(\vec{r}')\cdot\int_S\left[\left.\frac{\partial\vec{G}^{\,e}(\vec{r}'|\vec{r};\omega)}{\partial\omega}\right|_{\omega=\omega_p}(\omega-\omega_p)\;+\;\cdots\right]\cdot\vec{k}_p(\vec{r})\,dS\;=$$
$$-\frac{jk_c}{\eta_c}\int_S \vec{k}_p(\vec{r})\cdot\vec{E}^{\,i}(\vec{r},\omega)\,dS.$$

In the

in the

A

One r

q=p t

where

The al

in the

consid

(ω-ω

that na

to rela

large c

leads t

SEM l

In the limit $\omega \to \omega_p$, the term $(\omega - \omega_p)$ can annul at most a simple pole for the q=p term in the sum over q. This establishes the simple nature of the q=p pole.

At this point, two viewpoints may be adopted, leading to slightly different results. One method would be to take the limit of the above expression, and note that only the q=p term is non-vanishing, resulting in coupling coefficient

$$A_p = \lim_{\omega \to \omega_p} -\frac{jk_c}{\eta_c C_p} \int_S \vec{k}_p(\vec{r}) \cdot \vec{E}^i(\vec{r}, \omega) dS \tag{9}$$

where natural-mode currents are normalized such that (reciprocity invoked again)

$$C_p = \int_S dS \; \vec{k}_p(\vec{r}) \cdot \int_S \left. \frac{\partial \vec{\vec{G}}^e(\vec{r}|\vec{r}';\omega)}{\partial \omega} \right|_{\omega=\omega_p} \cdot \vec{k}_p(\vec{r}') dS'. \tag{10}$$

The above coupling coefficient is seen to be similar to a "class- 1" coupling coefficient in the transient SEM literature [18]. Alternatively, the frequency range $\omega \approx \omega_p$ is considered. All terms $q \neq p$ in the sum over q are small due to the presence of the term $(\omega - \omega_p)$, which does not cancel with the corresponding pole term. Moreover, it is found that natural frequencies ω_q are widely separated from each other $(\omega_n \approx 2\omega_{n-1})$, leading to relatively large denominators $(\omega - \omega_q)$. The combination of small numerators and large denominators for the $q \neq p$ terms indicate that their sum may be neglected. This leads to a quantity similar to a "class 2" coupling coefficient as defined in the transient SEM literature [18]

$$A_p = -\frac{jk_c}{\eta_c C_p} \int_S \vec{k}_p(\vec{r}) \cdot \vec{E}^i(\vec{r}, \omega) dS \tag{11}$$

with normalization (10), valid for frequencies $\omega \approx \omega_p$. The differences between equations (9) and (11) are minor, since the source excitation $\vec{E}^i(\vec{r},\omega)$ and the normalization constant $C_p(\omega)$ are assumed regular in the frequency range of interest. The two results become identical when evaluating residues at the poles in the transient response current summation, but the class-2 coefficient leads to a better physical interpretation of "turn-on" time, which is important in the transient case. For steady-state excitations the differences between (9) and (11) are not important, although for the remainder of this dissertation, the term "coupling coefficient" refers to expression (11).

Several observations can be made regarding equations (10) and (11). Coupling coefficient (11) is seen to be an overlap integral of the p^{th}-mode natural current with the impressed field. It is found that natural-mode currents $\vec{k}_p(\vec{r})$ can be modeled by fairly simple expressions, hence any difficulties associated with evaluation of integral (11) are due to the form of the impressed field. For plane-wave excitation, the simple form of $\vec{E}^i(\vec{r})$ yields an easily evaluated integral. Excitations due to infinite transmission lines will involve one-dimensional Sommerfeld integrals, leading to a more difficult numerical task. When the source of excitation is another finite size microstrip device, the impressed field will involve two-dimensional Sommerfeld integrals. A perturbation theory is developed in Chapter 5 which simplifies the analysis for nearly-identical devices.

Normalization constant C_p involves the frequency derivative of the Green's dyad

$\vec{G}^{e}(\vec{r}|\vec{r}';\omega)$. This derivative may be evaluated analytically, in a straightforward though tedious manner. Although C_p involves two-dimensional spectral integrals, it only needs to be evaluated once for a given mode and device.

3.4 SEM ANALYSIS OF THE MICROSTRIP DIPOLE

The coupling coefficient (11) and normalization constant (10) are in a compact form suitable for analytical manipulations. It is the aim of this section to explicitly obtain (10) and (11) for the example of a microstrip dipole excited by a nearby microstrip transmission line. It is found that the natural-mode current $\vec{k}_p(\vec{r})$ can be represented by an expression that leads to closed-form evaluation of the spatial integrals in (10). The impressed field in (11), due to the microstrip transmission line, is found to involve one-dimensional spectral integrals, where again spatial integrals can be preformed analytically.

The configuration to be considered is shown in Figure 3.3. A microstrip transmission line of infinite length and width $2w_t$ is located along the x-axis. A dipole of total length $L=2l$ and width $2w_d$ is located a distance d from the transmission line, at an angle θ. Coupling coefficient (11) along with normalization constant (10) relate the amplitude of the natural-mode current to the excitation provided by the transmission line. The following analysis neglects the effect of the transmission line field maintained by currents induced upon the microstrip line by dipole current $\vec{K}$ and its associated electric

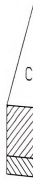

Figure

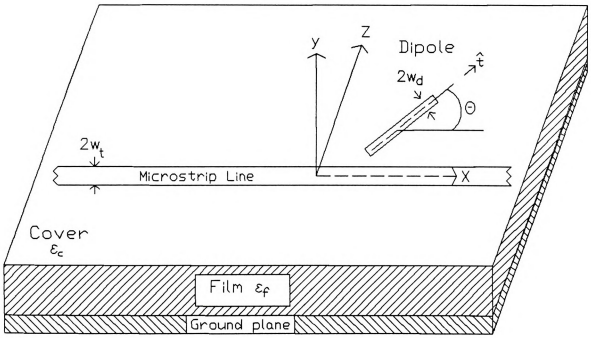

Figure 3.3: Microstrip dipole excited by a nearby transmission line.

field. This approximation is found to be valid for dipole elements spaced sufficiently far from the transmission line. This can be seen from the experimentally measured data of Figure 3.4 (Details of the experimental method can be found in Chapter 7). Figure 3.4 shows the real resonant frequency and quality-factor (Q-factor) of a 5.0 cm parallel-coupled ($\theta = 0$) dipole excited by the transmission line as a function of dipole/transmission line separation. The Q-factor, which is proportional to the complex component of frequency by $\omega_i = \omega_r / 2Q$, is a measure of the degree of coupling of the dipole to the transmission line. It can be seen that the real resonant frequency does not change substantially as the dipole position is varied. The Q-factor changes considerably for small dipole/line spacing, but becomes relativity constant for $d > .40$ cm. This indicates that for $d < .40$ cm mutual coupling in this dipole/transmission line system must be accounted for. When the dipole is located beyond $d = .40$ cm, the principal field of the unperturbed transmission line should be sufficient to represent the impressed excitation.

Furthermore, the radiation pattern of the dipole is principally normal to the plane of the dipole, and is zero in the plane of the dipole in the far field [39]. Although this work is not concerned with separations which would place the transmission line in the far field of the dipole, knowledge of the radiation pattern of the dipole qualitatively motivates neglecting the effect of the dipole field upon the transmission line for sufficient spacing.

3.4.1 NORMALIZATION CONSTANT

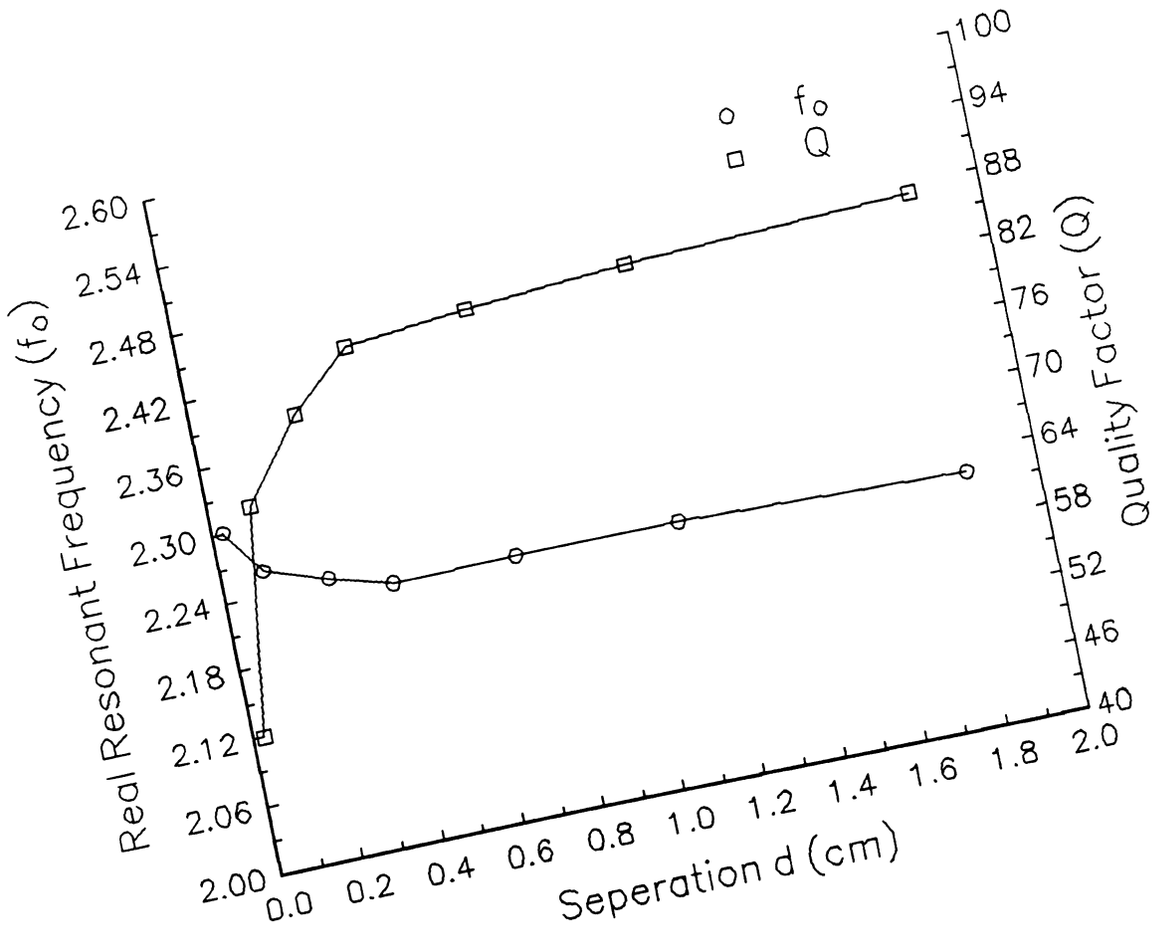

Figure 3.4: Measured real resonant frequency and Q-factor of a dipole excited microstrip transmission line as a function of dipole/line separation

3.4.1

Th

integra

found f

to (8),

definin

and onl

Fig

associa

These r

pulses

with th

very si

for eve

3.4.1 NORMALIZATION CONSTANT

The normalization constant (10) is a four-dimensional integral, with two spatial integrals and two spectral integrals (associated with $\ddot{G}^e$). Natural-mode currents $\vec{k}_p$ are found from the solution of (8). A pulse function/Galerkin's MoM procedure is applied to (8), to allow the unknown current freedom to assume any form required by the defining homogeneous EFIE. The details of this procedure are covered in Chapter 4, and only the results will be presented here.

Figure 3.5 shows complex resonant modes in the wavevector-plane, and their associated current distributions, obtained by the pulse function MoM solution of (8). These results were found by using 40 pulses over the dipole half-length, although fewer pulses lead to similar results. Even and odd modes are found to alternate, beginning with the principal first even mode. It is seen that the various current distributions are very similar to sinusoidal functions. This motivates modeling the modal current as

$$\vec{K}_p(\vec{r}) = \hat{t}\frac{a_n \cos\left[\frac{n\pi z}{2l}\right]}{\sqrt{1-\left[\frac{x}{w_d}\right]^2}} \tag{12}$$

for even modes; n=1,3,5 or

$$\vec{K}_p(\vec{r}) = \hat{t}\frac{a_n \sin\left[n\pi\frac{z}{l}\right]}{\sqrt{1-\left[\frac{x}{w_d}\right]^2}} \tag{13}$$

Real Resonant Frequency (f_o)

Figur

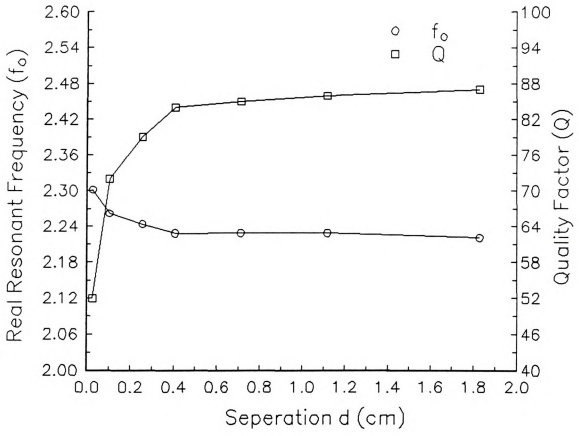

Figure 3.4: Measured real resonant frequency and Q-factor of a dipole excited by a microstrip transmission line as a function of dipole/line separation.

Figure

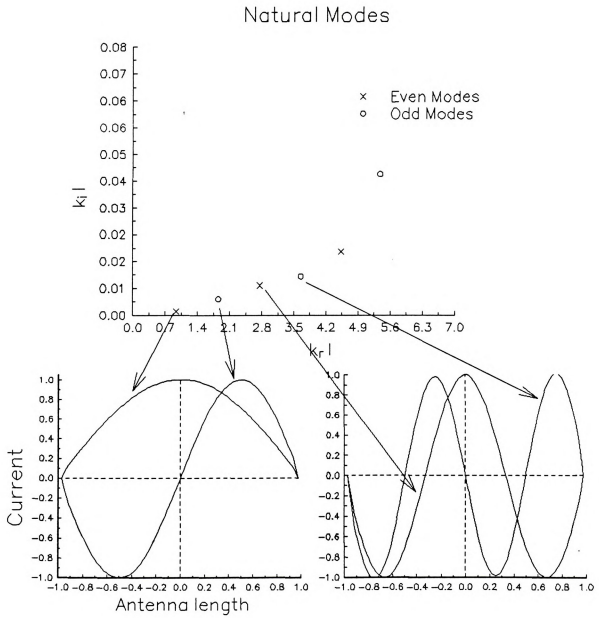

Figure 3.5: Microstrip dipole eigenmodes and their associated current distributions obtained by pulse-function MoM solution, 40 pulses.

for c

3.6

equa

comp

be v

know

V

is pr

Indiv

where

for odd modes; n=1,2,3. The unit vector $\hat{t}$ is oriented tangential to the dipole. Figure 3.6 shows the comparison between the pulse function MoM current distribution and equations (12,13) for the n=1 first even/odd modes, and Figure 3.7 shows the same comparison for the second even/odd modes. In each example, agreement is found to be very good. The square-root edge singularity in (12,13) is included to model well-known behavior at the dipole edges.

With $\vec{k}_p$ known, the normalization constant (10) may be found. Evaluation of

$$\vec{G}^{e\prime} = \left.\frac{\partial \vec{G}^{e}(\vec{r}|\vec{r}';\omega)}{\partial\omega}\right|_{\omega=\omega_p}$$

is preformed by term by term differentiation of the electric Green's dyad $\vec{G}^{e}$. Individual terms of $\vec{G}^{e\prime}$ are found to be

$$\begin{Bmatrix} G_t^{r\prime} \\ G_c^{r\prime} \\ G^{p\prime} \end{Bmatrix} = \int_{-\infty}^{\infty}\int d\xi d\zeta \; \frac{e^{j[\xi(x-x')+\zeta(z-z')]}}{2(2\pi)^2 p_c} \begin{Bmatrix} \left[\frac{R_t b_c^2\omega}{p_c}\left[(y+y')+\frac{1}{p_c}\right]+R_t'\right]e^{-p_c(y+y')} \\ \left[\frac{C b_c^2\omega}{p_c}\left[(y+y')+\frac{1}{p_c}\right]+C'\right]e^{-p_c(y+y')} \\ \frac{b_c^2\omega}{p_c}\left[|y-y'|+\frac{1}{p_c}\right]e^{-p_c|y-y'|} \end{Bmatrix}$$

where $b_c = n_c\sqrt{\mu_0\epsilon_0}$ and derivatives of reflection and coupling coefficients (2.18) are

Normalized Current Amplitude

Figure

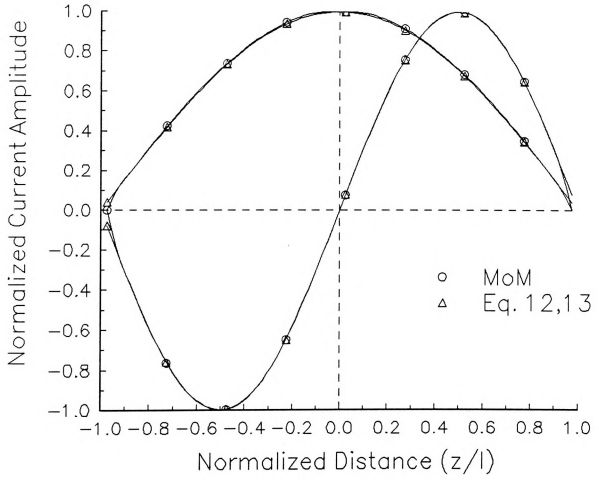

Figure 3.6: Comparison of nullspace current distribution (pulse function MoM) and approximate current distribution (eq's. 12,13) for the first even/odd modes

Normalized Current Amplitude

Figure

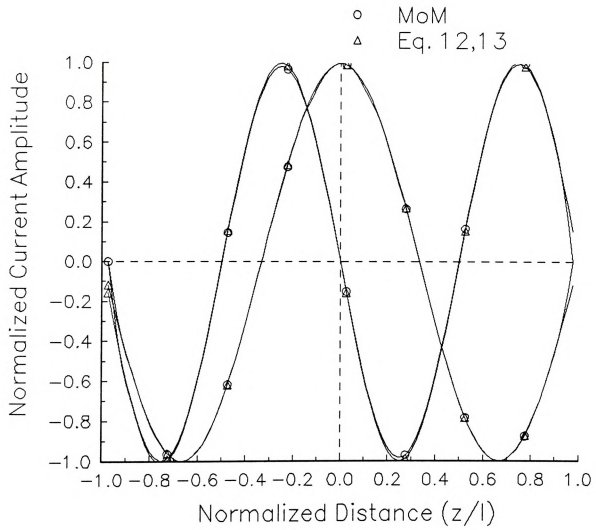

Figure 3.7: Comparison of nullspace current distribution (pulse function MoM) and approximate current distribution (eq's 12,13) for the second even/odd modes.

with *N*

respect

Sp

current

and

lead to

$$R_t' = \frac{1}{Z^h}\left[N_1' - \frac{N_1 Z^{h'}}{Z^h}\right]$$

$$C' = \frac{-2(N_{fc}^2-1)}{Z^h Z^e}\left[\frac{b_c^2\omega}{p_c} + \frac{p_c Z^{e'}}{Z^e} + \frac{p_c Z^{h'}}{Z^h}\right]$$

with N_1, Z^e, and Z^h defined by (2.19). In the above, primes denote differentiation with respect to ω; e.g., $A' = \left.\frac{\partial A}{\partial \omega}\right|_{\omega=\omega_p}$.

Spatial integrals over dipole surface S may now be evaluated, using natural-mode current distribution (12) or (13). The integrals

$$\int_{-w_d}^{w_d} \frac{e^{\pm j\xi x}}{\sqrt{1-\left(\frac{x}{w_d}\right)^2}} dx = (w_d\pi)J_0(\xi w_d)$$

and

$$\int_{-l}^{l} \cos\left(\frac{n\pi z}{2l}\right) e^{\pm j\zeta z} dz = \frac{(n\pi l)\sin\left(\frac{n\pi}{2}\right)\cos(\zeta l)}{\left(\frac{n\pi}{2}+\zeta l\right)\left(\frac{n\pi}{2}-\zeta l\right)} = I_1(n,l,\zeta) \qquad (14)$$

$$\int_{-l}^{l} \sin\left(\frac{n\pi z}{l}\right) e^{\pm j\zeta z} dz = \mp\frac{j(-1)^n(2nl\pi)\sin(\zeta l)}{(n\pi+\zeta l)(n\pi-\zeta l)} = I_2(n,l,\zeta)$$

lead to

for ev

been p

3.4.2

Th

curren

provid

discus

It

transm

where

similar

$$C_p = 4\int_0^{\infty}\int_0^{\pi/2} \frac{\lambda}{2(2\pi)^2}\left\{\frac{b_c^2\omega(R_t+1)}{p_c}\left[\left(\frac{b_c\omega}{p_c}\right)^2+2-\left(\frac{\lambda\sin(\theta)}{p_c}\right)^2\right]\right.$$

$$\left. + \frac{R_t'}{p_c}\left[(b_c\omega)^2-\lambda^2\sin^2(\theta)\right]+\lambda^2\sin^2(\theta)\right\} \qquad (15)$$

$$(w_d\pi)^2 J_0^2(\lambda\cos(\theta)w_d)\begin{Bmatrix} I_1(n,l,\lambda) \\ I_2(n,l,\lambda)\end{Bmatrix}^2 d\theta\, d\lambda$$

for even/odd modes where J_0 is the 0^{th} order Bessel function [40]. Equation (15) has been put in polar form by the transformation (2.28).

3.4.2 COUPLING COEFFICIENT

The coupling coefficient (11) relates the amplitude of induced natural resonant-mode current $\vec{k}_p$ to the impressed excitation $\vec{E}^i$. The field of a microstrip transmission line provides the desired excitation, under the assumptions excluding mutual coupling discussed earlier.

It has been found that the even-mode current distribution on a x-directed microstrip transmission line in the propagation regime is efficiently represented by [41]

$$\vec{k}_m(\vec{r}) = \left\{\hat{x}\sum_{n=0}^{\infty}\frac{a_{x(n+1)}T_{2n}(z/w_t)}{\sqrt{1-(z/w_t)^2}} + \hat{z}\sum_{n=0}^{\infty}a_{z(n+1)}T_{2n+1}(z/w_t)\sqrt{1-(z/w_t)^2}\right\}e^{-j\beta x} \qquad (16)$$

where T_n are the Chebyshev polynomials [40]. The odd-mode current is given by a similar expression. Propagation eigenvalues β are found by a numerical root-search of

a cou

nullsp

propa

transv

nume

electr

Subst

of [4

result

The c

where

a coupled set of spectral EFIE's, and amplitude coefficients $a_{\begin{Bmatrix}z\\x\end{Bmatrix}(n+1)}$ are obtained as the nullspace of the solution matrix. For the example considered here, only even propagation modes are considered. For narrow transmission lines ($w_t \ll \lambda_0$), the transverse component of current may be ignored for field computations, although the numerical root-search for propagation eigenvalues includes both components. The electric field of the transmission line is found from equation (2.21) as

$$\vec{E}^i(\vec{r}) = \frac{-j\eta_c}{k_c}\int_s \ddot{G}^e(\vec{r}|\vec{r}')\cdot\vec{k}_m(\vec{r}')dS'. \tag{17}$$

Substituting the x-component of transmission line current (16) into (17), and making use of [42]

$$\int_{-\infty}^{\infty} e^{-jx(\beta+\xi)}dx = 2\pi\delta(\beta+\xi)$$

results in field components

$$E_{\begin{Bmatrix}x\\z\end{Bmatrix}}(\vec{r}) = e^{-j\beta x}\int_{-\infty}^{\infty}\begin{Bmatrix}Y(\zeta)\\F(\zeta)\end{Bmatrix}N(\zeta)e^{j\zeta z}d\zeta. \tag{18}$$

The coefficients in (18) are given by

$$Y(\zeta) = \frac{[(k_c^2-\beta^2)(R_t+1)+\beta^2 p_c C]}{4\pi j\omega n_c^2\epsilon_0 p_c}$$

$$F(\zeta) = \frac{[R_t+1-p_c C]\beta\zeta}{4\pi j\omega n_c^2\epsilon_0 p_c}$$

where R_t, C, and p_c are evaluated at $\xi=-\beta$. The term $N(\zeta)$ arises from the spatial

integra

The ch

leads

where

Cheb

wher

The

of st

trans

integration transverse to the transmission line as

$$N(\zeta) = \int_{-w_t}^{w_t} \sum_{n=0}^{\infty} \frac{a_{2(n+1)} T_{2n}(z'/w_t)}{\sqrt{1-(z'/w_t)^2}} e^{-j\zeta z'} dz'. \qquad (19)$$

The change of variable

$$\bar{z} = z'/w_t$$
$$d\bar{z} = dz'/w_t$$

leads to

$$N(\zeta) = \sum_{n=0}^{\infty} 2w_t a_{2(n+1)} \int_0^1 \frac{T_{2n}(\bar{z})}{\sqrt{1-\bar{z}^2}} \cos(\zeta w_t \bar{z}) d\bar{z}$$

where the integration and summation have been interchanged and the even nature of the Chebyshev polynomials has been exploited. The integral identity [43]

$$\int_0^1 T_{2n}(z)\cos(az)\frac{dz}{\sqrt{1-z^2}} = (-1)^n \frac{\pi}{2} J_{2n}(a) \qquad [a>0]$$

where $J_m(a)$ is the mth order Bessel function leads to

$$N(\zeta) = \pi w_t \sum_{n=0}^{\infty} a_{2(n+1)} (-1)^n J_{2n}(\zeta w_t).$$

The field distribution arising from (18) is shown in Figure 3.8, for a representative set of structural parameters at an operating frequency of 8.95 GHz.

The expression for electric field components (18) is valid for a x-directed transmission line. In order to allow for the impressed field to have an arbitrary

E—Field Amplitude

Figure

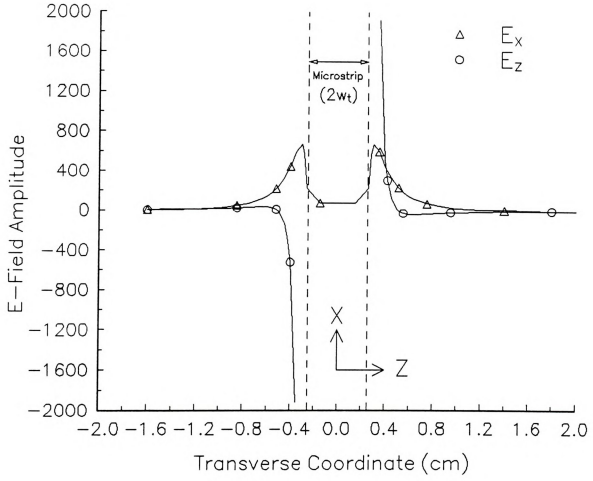

Figure 3.8: Electric field distribution of a microstrip transmission line, principal even propagation modes, x-component of current.

orientation, the field components are assumed to be referenced to a local coordinate system (x_1',z_1'), as shown in Figure 3.9.

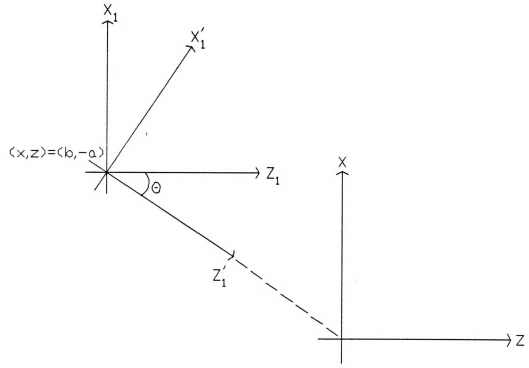

Figure 3.9: Local and global coordinate system used for field component evaluation.

The translation and rotation of coordinates

$$
\begin{aligned}
x_1 &= x - b \\
z_1 &= z + a \\
x_1' &= x_1\cos(\theta) + z_1\sin(\theta) \\
z_1' &= z_1\cos(\theta) - x_1\sin(\theta)
\end{aligned}
$$

lead to the field components with respect to the global coordinates (x,z)

$$
E_{\left\{\begin{matrix}x\\z\end{matrix}\right\}}(r) = e^{-j\beta[x\cos(\theta)+z\sin(\theta)]} \int_{-\infty}^{\infty} \left\{\begin{matrix}\cos(\theta)Y(\zeta) - \sin(\theta)F(\zeta)\\ \sin(\theta)Y(\zeta) + \cos(\theta)F(\zeta)\end{matrix}\right\} N(\zeta) \cdot e^{-jx\zeta\sin(\theta)} e^{jz\zeta\cos(\theta)} e^{j\zeta d}\, d\zeta. \tag{20}
$$

The coupling coefficient (11) is found from the impressed excitation (20) and natural-mode current (12,13) as

$$A_p = -\frac{jk_c}{C_p\zeta_c}\int_0^{\infty}\left\{J_0(\alpha_1 w_d)e^{j\zeta d}\begin{Bmatrix}I_1(n,l,\alpha_3)\\ I_2(n,l,\alpha_3)\end{Bmatrix}[\sin(\theta)Y(\zeta)+\cos(\theta)F(\zeta)]\right.$$
$$\left. + J_0(\alpha_2 w_d)e^{-j\zeta d}\begin{Bmatrix}I_1(n,l,\alpha_4)\\ I_2(n,l,\alpha_4)\end{Bmatrix}[\sin(\theta)Y(\zeta)-\cos(\theta)F(\zeta)]\right\}d\zeta \qquad (21)$$

where

$$\begin{aligned}\alpha_1 &= -\beta\cos(\theta)-\zeta\sin(\theta) & \alpha_3 &= -\beta\sin(\theta)+\zeta\cos(\theta)\\ \alpha_2 &= -\beta\cos(\theta)+\zeta\sin(\theta) & \alpha_4 &= -\beta\sin(\theta)-\zeta\cos(\theta).\end{aligned} \qquad (22)$$

3.5 SUMMARY

The electromagnetic interactions of microstrip integrated electronic devices are described by an electric field integral equation (EFIE)

$$\hat{t}\cdot\int_S \vec{G}^{\,e}(\vec{r}|\vec{r}')\cdot\vec{K}(\vec{r}')dS' = -\frac{jk_c}{\eta_c}\hat{t}\cdot\vec{E}^{\,i}(\vec{r}) \;\ldots\; \forall\ \vec{r}\in S \qquad (23)$$

utilizing the rigorous dyadic Green's functions presented in Chapter 2. The numerical difficulty associated with evaluation of these functions hinders the straightforward solution of eq. (23) by the method of moments (MoM), and prompts an alternative technique. Following the methodology of the well-established singularity expansion method (SEM) which quantifies the EM responses of free-space scatterers, the microstrip device surface current is written as a sum of pole singularities in the complex ω-plane,

$$\vec{K}(\vec{r},\omega) \approx \sum_q \frac{A_q \vec{k}_q(\vec{r})}{(\omega - \omega_q)} \tag{24}$$

where ω_p is a complex natural frequency, $\vec{k}_p$ is the natural-mode current distribution associated with the pth natural-mode, and A_p is the amplitude of the pth natural mode. For steady-state excitations, only one or two terms of (24) are needed to represent the surface current near resonance. Exploiting current (24) in EFIE (23) leads to the defining relation for natural resonance modes

$$\hat{t} \cdot \int_S \ddot{G}^e(\vec{r}|\vec{r}';\omega) \cdot \vec{k}_p(\vec{r}') dS' = 0 \ \ldots \ \forall \ \vec{r} \in S \tag{25}$$

with non-trivial solutions only for $\omega = \omega_p$. Equation (25) defines the pth natural mode with complex natural frequency ω_p.

Amplitude coefficients A_q are found by applying reciprocity of the electric dyadic Green's function to EFIE (23), subsequent to testing with an appropriate natural-mode integral operator. The Green's dyad $\ddot{G}^e$ is expanded in a Taylor's series about $\omega = \omega_p$, leading to

$$A_p = -\frac{jk_c}{\eta_c C_p} \int_S \vec{k}_p(\vec{r}) \cdot \vec{E}^i(\vec{r},\omega) dS \tag{26}$$

where the natural-mode currents are normalized according to

$$C_p = \int_S dS\ \vec{k}_p(\vec{r}) \cdot \int_S \left. \frac{\partial \vec{\vec{G}}^e(\vec{r}|\vec{r}';\omega)}{\partial \omega} \right|_{\omega=\omega_p} \cdot \vec{k}_p(\vec{r}')\, dS'. \tag{27}$$

The electromagnetic response of a microstrip dipole excited by a microstrip transmission line is studied. The unperturbed field of an isolated transmission line is used to approximate the impressed excitation, leading to explicit expressions for natural-mode current amplitude A_p.

CHAPTER FOUR

FULL-WAVE SOLUTIONS OF THE FUNDAMENTAL EFIE AND EXPERIMENTAL AND THEORETICAL VALIDATION OF THE SEM THEORY

4.1 INTRODUCTION

In Chapter 3, the fundamental EFIE which quantifies electromagnetic interactions in microstrip circuits was developed. A dominant-mode singularity expansion analysis was presented which leads to an approximate representation for device surface currents induced by an impressed excitation. Pole-singularity terms were also seen to lead to the defining relation for natural modes, which is conventionally found by the source-free solution to the defining EFIE. In this chapter, full-wave solutions to the fundamental EFIE are presented, which provide a comparison to the singularity expansion approximation. Results obtained by the methods detailed in this chapter and Chapter 3 are presented, and compared with measurements.

EFIE (3.1) can be solved by the method of moments (MoM) [44]. The MoM is a general technique to transform an operator equation into a matrix equation which can be solved on a computer. Salient features of the MoM are summarized here, beginning with a general operator equation,

$$AX = Y \tag{1}$$

wher

unkn

with

In (2)

R_W, i

and i

wher

and I

weigh

metho

weigh

This

where A denotes an operator and X is the unknown to be determined for a given Y. The unknown X is expanded in a set of known expansion (or basis) functions x_i,

$$X \approx X_N = \sum_{i=1}^{N} \alpha_i x_i$$

with unknown coefficients α_i. This approximation is substituted into (1), resulting in

$$\sum_{i=1}^{N} \alpha_i A x_i = Y_N. \tag{2}$$

In (2), Y_N is the solution obtained from the approximate expansion $X \approx X_N$. The residual, R_N, is formed as

$$R_N = A X_N - Y = Y_N - Y$$

and is weighted to zero with respect to a weighting function W_i,

$$\langle R_N, W_i \rangle = 0, \qquad i = 1, \cdots, N \tag{3}$$

where the bracket notation indicates a suitable inner product [44,45] such as

$$\langle u, v \rangle = \int_L u(z) v(z) dz$$

and L denotes the domain of the inner product. A common procedure is to choose the weighting functions equal to the expansion functions, which is known as Galerkin's method. Implementation of the MoM then requires choosing appropriate expansion and weighting functions which will result in an accurate and efficient numerical solution. This has been discussed by many authors, more recently by Sarkar et al. [46].

The solution of integral equations for microstrip antenna problems (dipoles and patches) have been investigated in many papers [6-11,47-52]. Various expansion functions have been used, and Galerkin's method is usually implemented. Two different MoM solutions are developed in this chapter, using different basis functions.

In Section 4.2, EFIE (3.1) is transformed into a Hallen's form integral equation (HFIE) [53], and subsequently solved with sub-domain basis functions. It is believed that the use of the Hallen form IE for microstrip circuits is new, and a discussion of its relative merits is included in Section 4. The HFIE can be solved in general for any type of current, or even/odd modes can be specified analytically.

The next section presents a solution of the EFIE by the MoM, with entire-domain basis functions. It is found that an appropriate choice of basis functions results in good accuracy with a small number of terms, and just one term is often satisfactory for excitations near a natural resonant frequency.

In Section 4, a comparison between the solution of the EFIE with entire-domain basis functions and that of the HFIE with sub-domain basis functions is presented. It is found that each method has advantages for certain applications and disadvantages for others. Convergence studies for both methods are presented, and the method of numerical integration used for each solution, introduced in Section 2.4.2, is discussed.

Numerical and experimental results are presented in Section 5. Characteristics of transmission line fed dipoles such as frequency response and induced current amplitude vs. dipole/transmission-line separation are studied. The differing theoretical methods presented in this chapter and in Chapter 3 are found to agree with each other, as well as

with measured results. Power dissipation due to space and surface-wave radiation, ohmic loss and dielectric loss is discussed.

4.2 HALLEN-FORM SOLUTION WITH SUB-DOMAIN BASIS FUNCTIONS

The EFIE (3.1) relates the unknown surface current on a microstrip device, $\vec{K}(\vec{r})$, to the known impressed electric field, as

$$\hat{t}\cdot(k_c^2+\nabla\nabla\cdot)\int_S \vec{\vec{G}}(\vec{r}\,|\,\vec{r}\,')\cdot\vec{K}(\vec{r}\,')\,dS' = -\frac{jk_c}{\eta_c}\hat{t}\cdot\vec{E}^i(\vec{r}) \;\ldots\; \forall\ \vec{r}\in S. \tag{4}$$

The integral term in (4),

$$\vec{R}(\vec{r}) = \int_S \vec{\vec{G}}(\vec{r}\,|\,\vec{r}\,')\cdot\vec{K}(\vec{r}\,')\,dS' \tag{5}$$

is in the form of a magnetic vector potential. Equation (4) can then be written as a differential equation for the vector potential

$$\hat{t}\cdot(k_c^2+\nabla\nabla\cdot)\vec{R}(\vec{r}) = -\frac{jk_c}{\eta_c}\hat{t}\cdot\vec{E}^i(\vec{r}). \tag{6}$$

For a narrow, z-directed dipole,

$$\vec{K}(\vec{r}) \approx \hat{z}K_z(\vec{r})$$

$$\hat{t}=\hat{z}$$

which leads to the scaler differential equation

$$\left(k_c^2 + \frac{\partial^2}{\partial z^2}\right) R_1(\vec{r}) + R_2(\vec{r}) = -\frac{jk_c}{\eta_c} E_z^i(\vec{r}) \tag{7}$$

with

$$R_1(\vec{r}) = \int_S (G^p + G_t^r) K_z(\vec{r}') dS'$$

$$R_2(\vec{r}) = \int_S \frac{\partial^3 G_c^r}{\partial y \partial z^2} K_z(\vec{r}') dS'$$

and the Green's dyad components are understood to be functions of both source and field points, e.g.: $G_\beta^\alpha = G_\beta^\alpha(\vec{r}\,|\,\vec{r}')$. The term

$$k_c^2 \int_S \frac{\partial G_c^r}{\partial y} K_z(\vec{r}') dS'$$

is added and subtracted from the LHS of (7), resulting in the forced differential equation

$$\left(k_c^2 + \frac{\partial^2}{\partial z^2}\right) L(\vec{r}) = F(\vec{r}) \tag{8}$$

where

$$L(\vec{r}) = \int_S G_s K_z(\vec{r}') dS' \tag{9}$$

and

$$F(\vec{r}) = k_c^2 \int_S \frac{\partial G_c^r}{\partial y} K_z(\vec{r}') dS' - \frac{jk_c}{\eta_c} E_z^i(\vec{r})$$

$$G_s(\vec{r}\,|\,\vec{r}') = \left[G^p(\vec{r}\,|\,\vec{r}') + G_t^r(\vec{r}\,|\,\vec{r}') + \frac{\partial G_c^r(\vec{r}\,|\,\vec{r}')}{\partial y} \right]. \tag{10}$$

The homogeneous solution of (8) is given by

$$L_h(\vec{r}) = C_1\cos(k_c z) + C_2\sin(k_c z) \tag{11}$$

where C_1 and C_2 are treated as constants although they are actually functions of x,y. The justification for treating C_1 and C_2 as constants is as follows:

Consider the homogeneous differential equation

$$\left(k_c^2 + \frac{\partial^2}{\partial z^2}\right) L(x,y,z) = 0 \tag{12}$$

where $L(x,y,z)$ is defined by (9). Equation (12) can be solved easily to yield

$$\int_S G_s K_z(\vec{r}\,')\,dS' = C_1(x,y)\cos(k_c z) + C_2(x,y)\sin(k_c z) \tag{13}$$

where C_1 and C_2 are unknown functions of x,y. Making use of the spectral representation for Green's components (2.17), equation (13) may be written as

$$\int_{-\infty}^{\infty}\int e^{j\xi x} e^{j\zeta z} e^{-p_c y} H(\lambda) d^2\lambda = C_1(x,y)\cos(k_c z) + C_2(x,y)\sin(k_c z) \tag{14}$$

for source points on the film layer surface $y'=0$, and assuming field points $y \geq 0$. The term $H(\lambda)$ comes from the coefficients of the Green's dyad components and the spatial integration as

$$H(\lambda) = \frac{(1+R_t - p_c C)}{2(2\pi)^2 p_c}\int_S e^{-j\xi x'} e^{-j\zeta z'} K_z(x',z')dS'.$$

The functional dependence of the LHS of (14) on x,y can now be studied, and compared to that of the RHS. Since the original EFIE is valid only for field points $\vec{r} \in S$, equation

(14)

at x=

expa

wher

integ

term

(15),

the v

the t

Simi

Equa

Equa

(14) is limited to the same region. For narrow dipoles oriented along the z axis, centered at x=z=0, the field point variation in x will be minimal ($x=0\pm\delta x$). The LHS may be expanded in a Taylor's series about x=0,

$$LHS(x,y,z) = \int_{-\infty}^{\infty}\int \left(1 + j\xi x - \frac{\xi^2}{2}x^2 + \cdots\right) e^{j\zeta z} e^{-p_c y} H(\lambda) d^2\lambda \tag{15}$$

where derivatives with respect to x can be taken inside the spectral integral since the integrand is continuously differentiable in x. Equation (15) may be written as a sum of terms, where it is seen that small variations in x about x=0 result in small variations in (15), assuming, of course, that the spectral integral converges to a finite value. Since the variation in the RHS of (14) as a function of x must be the same as that of the LHS, the terms C_1 and C_2 must change very little with x and may be treated as constants. Similar arguments apply to the y variation, and in fact $y=0$ is usually implemented.

The particular solution of (8) is given by

$$L_p(\vec{r}) = \frac{1}{k_c}\int_0^z F(x,y,z=z')\sin[k_c(z-z')]dz'. \tag{16}$$

Equations (9)-(11) and (16) combine to yield the desired IE

$$\int_S G_s K_z(\vec{r}')dS' = C_1\cos(k_c z) + C_2\sin(k_c z) + k_c\int_0^z \left[\int_S \frac{\partial G_c^r}{\partial y} K_z(\vec{r}')dS' - \frac{j}{k_c\eta_c}E_z^i(\vec{r})\right]_{z=z'} \sin[k_c(z-z')]dz'. \tag{17}$$

Equation (17) is the general form of the HFIE for microstrip dipoles.

4.2.1 MoM SOLUTION OF THE GENERAL HFIE

Equation (17) can be solved by the MoM, after choosing an appropriate set of basis and weighting functions. Two general classes of basis functions exist. Sub-domain basis functions (SBF) exist only over subsections of dipole surface S, and are zero everywhere else. Entire-domain basis functions (EBF) exist over the entire range of S, and should be chosen to model the vanishing of current at the device ends. In this section, pulse-function (PF) sub-domain basis functions are used as both basis and weighting functions, forming a pulse-function Galerkin's solution.

Consider a dipole of width $2w_d$ and total length $L=2l$ which is centered at the origin of coordinates (x,z) along the z axis, as shown in Figure 4.1a. The dipole is subdivided into 2N sections, each of width 2δ. The current in (17) is expanded in a set of pulse functions (PF),

$$K_z(x,z) = \sum_{n=-N}^{N} \frac{a_n P_n(z)}{\sqrt{1-\left(\frac{x}{w_d}\right)^2}} \tag{18}$$

with unknown amplitude a_n. The square root edge singularity condition is incorporated in (18) to model well-known behavior of the current. The PF's are defined by

$$P_n(z) = \begin{cases} 1 & |z-z_n|<\delta \\ 0 & otherwise \end{cases}$$

where 2δ is the size of the partition, as shown in figure 4.1b. The weighting function

$2w_c$

Figu

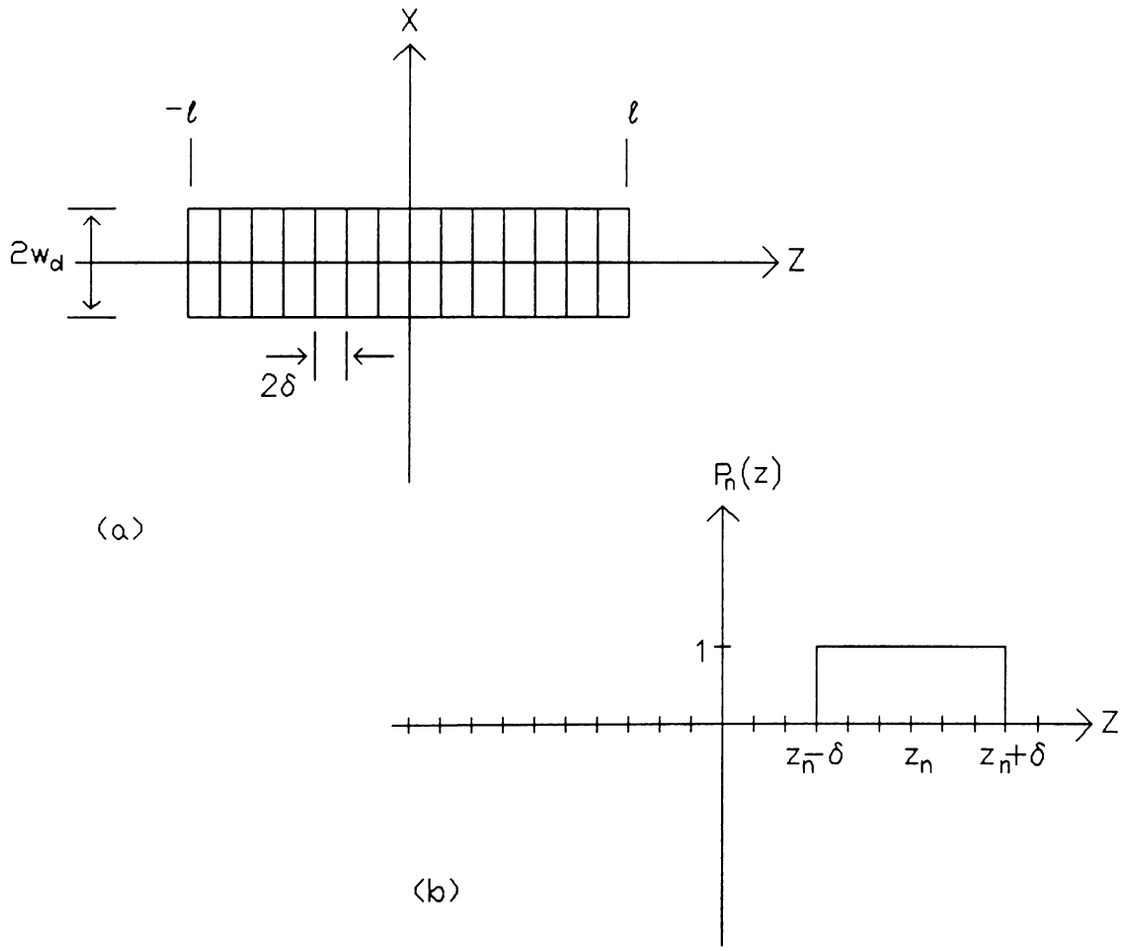

Figure 4.1: Microstrip dipole subdivided into segments for pulse function expansion (a). Pulse function distribution (b).

$$W_m(x,z) = \frac{P_m(z)}{\sqrt{1-\left(\frac{x}{w_d}\right)^2}}$$

is applied to HFIE (17) resulting in

$$\int_{-w_d}^{w_d}\int_{-l}^{l} dzdx \frac{P_m(z)}{\sqrt{1-\left(\frac{x}{w_d}\right)^2}} \left\{ \int_{-w_d}^{w_d}\int_{-l}^{l} G_s \sum_{n=-N}^{N} \frac{a_n P_n(z')}{\sqrt{1-\left(\frac{x'}{w_d}\right)^2}} dz'dx' - \right.$$

$$k_c \int_0^z \left[\int_{-w_d}^{w_d}\int_{-l}^{l} \frac{\partial G_c^r}{\partial y} \sum_{n=-N}^{N} \frac{a_n P_n(\gamma)}{\sqrt{1-\left(\frac{x'}{w_d}\right)^2}} d\gamma dx' - \frac{j}{k_c \eta_c} E_z^i(\vec{r}) \right]_{z=z'} \sin[k_c(z-z')]dz' \qquad (19)$$

$$\left. C_1 \cos(k_c z) - C_2 \sin(k_c z) \right\} = 0.$$

The order of integration and summation may be interchanged, since the sum is finite and all integrations are assumed to be convergent. Exploiting the sub-sectional nature of the pulse functions reduces the integrations over z such that

$$\int_{-w_d}^{w_d}\int_{-l}^{l} f(x,z)P_n(z)dzdx = \int_{-w_d}^{w_d}\int_{z_n-\delta}^{z_n+\delta} f(x,z)\,dzdx.$$

The spectral integrals associated with the Green's function components are evaluated in rectangular form, as detailed in Section 2.4.2. The integrals

and

lead

The

is i

$$\int_{-w_d}^{w_d} \frac{e^{\pm j\xi x}}{\sqrt{1-\left(\frac{x}{w_d}\right)^2}} dx = (w_d\pi)\, J_o(\xi w_d)$$

$$\int_{-w_d}^{w_d} \frac{1}{\sqrt{1-\left(\frac{x}{w_d}\right)^2}} dx = w_d\pi$$

and

$$\int_0^z e^{\pm j\zeta z'} \sin[k_c(z-z')]dz' = \frac{1}{(k_c^2-\zeta^2)}\{k_c[\cos(\zeta z)-\cos(k_c z)]$$

$$\pm j[k_c \sin(\zeta z) - \zeta \sin(k_c z)]\}$$

lead to the matrix equation

$$\sum_{n=-N}^{N} a_n M_{mn} - 2(w_d\pi)\frac{\sin(k_c\delta)}{k_c}\{C_1\cos(k_c z_m) + C_2\sin(k_c z_m)\} = B_m . \tag{20}$$

The term

$$M_{mn} = 16\int_0^{\infty} d\zeta \left\{\cos[\zeta(z_n - z_m)]\frac{\sin^2(\zeta\delta)}{\zeta^2}\left[S_1(\zeta) + \frac{S_2(\zeta)}{(k_c^2-\zeta^2)}\right]\right.$$

$$- \frac{\sin(k_c\delta)}{k_c}\frac{\sin(\zeta\delta)}{\zeta}\left[\cos(\zeta z_n)\cos(k_c z_m)\right. \tag{21}$$

$$\left.\left. + \frac{\zeta}{k_c}\sin(\zeta z_n)\sin(k_c z_m)\right]\frac{S_2(\zeta)}{(k_c^2-\zeta^2)}\right\}$$

is in the form of a 2-dimensional spectral integral, where

$$S_1(\zeta) = \int_0^{\infty} (w_d \pi)^2 J_0^2(\xi w_d) \frac{(1 + R_t - p_c C)}{2(2\pi)^2 p_c} d\xi$$

$$S_2(\zeta) = \int_0^{\infty} (w_d \pi)^2 J_0^2(\xi w_d) \frac{K_c^2 C}{2(2\pi)^2} d\xi \qquad (22)$$

and J_0 is the Oth order Bessel function [40]. The above two terms arise from the spatial integrations over the transverse coordinate, and are approximated by Chebyshev polynomials [54] over ranges of ζ that might be encountered in performing the spectral integral in (21). Evaluation of matrix entries (21) is then reduced to performing a 1-dimensional spectral integral involving the approximated functions $S_1(\zeta)$, $S_2(\zeta)$, and simple trigonometric functions. Since $S_1(\zeta)$ and $S_2(\zeta)$ are approximated only once for all matrix elements, this method is increasingly efficient as the number of sub-sectional pulse functions increases. Later, a entire-domain basis function MoM solution to the same EFIE will be obtained. This solution requires a relatively small number of matrix entries, and it was found for this method that the polar integration scheme discussed in Section 2.4.2 is preferable.

The RHS of (20) is given by

$$B_m = \int_{-w_d}^{w_d} \int_{-l}^{l} \frac{p_m(z)}{\sqrt{1 - \left(\frac{x}{w_d}\right)^2}} \left[-\frac{j}{k_c \eta_c} \int_0^z E_z^i(x,y,z=z') \sin[k_c(z - z')] \, dz' \right] dz dx \qquad (23)$$

For the arbitrarily oriented incident field of a microstrip transmission line, $E_z^i(\vec{r})$ is given

by (3

wher

last

Exp

by (3.20). With (3.20), equation (23) becomes

$$B_m = -\frac{j}{k_c\eta_c}\int_0^{\infty} d\zeta N(\zeta)(w_d\pi)\left\{\frac{1}{(k_c^2-\alpha_1^2)}\left[k_c\left(\frac{2}{\alpha_1}\cos(z_m\alpha_1)\sin(\alpha_1\delta)\right.\right.\right.$$
$$\left.-\frac{2}{k_c}\cos(z_m k_c)\sin(k_c\delta)\right)+j\left(k_c\frac{2}{\alpha_1}\sin(z_m\alpha_1)\sin(\alpha_1\delta)\right.$$
$$\left.\left.-\alpha_1\frac{2}{k_c}\sin(z_m k_c)\sin(k_c\delta)\right)\right]\cdot J_0(\alpha_3 w_d)e^{j\zeta d}[\sin(\theta)Y(\zeta)+\cos(\theta)F(\zeta)]$$
$$+\frac{1}{(k_c^2-\alpha_2^2)}\left[k_c\left(\frac{2}{\alpha_2}\cos(z_m\alpha_2)\sin(\alpha_2\delta)-\frac{2}{k_c}\cos(z_m k_c)\sin(k_c\delta)\right)\right. \tag{24}$$
$$\left.-j\left(k_c\frac{2}{\alpha_2}\sin(z_m\alpha_2)\sin(\alpha_2\delta)-\alpha_2\frac{2}{k_c}\sin(z_m k_c)\sin(k_c\delta)\right)\right]$$
$$\left.\cdot J_0(\alpha_4 w_d)e^{-j\zeta d}[\sin(\theta)y(\zeta)-\cos(\theta)F(\zeta)]\right\}$$

where α_{1-4}, $Y(\zeta)$, $F(\zeta)$, and $N(\zeta)$ are defined in Chapter 3.

The system of equations (20) has 2N equations and 2N+2 unknowns. The first and last pulse amplitude can be set to zero, since the current must vanish at the dipole ends. Exploiting $a_{-N}=a_N=0$ leads to a (2N x 2N) system of equations,

$$\begin{bmatrix} K_{(-N)(-N)} & \cdots & K_{(-N)N} \\ \vdots & \ddots & \vdots \\ K_{N(-N)} & \cdots & K_{NN} \end{bmatrix} \begin{bmatrix} C_1 \\ a_{(-N+1)} \\ \vdots \\ a_{(N-1)} \\ C_2 \end{bmatrix} = \begin{bmatrix} B_{-N} \\ \vdots \\ B_N \end{bmatrix} \tag{25}$$

which may be solved be standard matrix methods. Matrix entries are given by

$$K_{mn} = \begin{cases} M_{mn} & \cdots \text{for } \begin{matrix} m = -N, \cdots, N \\ n = -N+1, \cdots, N-1 \end{matrix} \\ -2(w_d\pi)\cos(k_c z_m)\dfrac{\sin(k_c\delta)}{k_c} & \cdots \text{for } \begin{matrix} m = -N, \cdots, N \\ n = -N \end{matrix} \\ -2(w_d\pi)\sin(k_c z_m)\dfrac{\sin(k_c\delta)}{k_c} & \cdots \text{for } \begin{matrix} m = -N, \cdots, N \\ n = N \end{matrix} \end{cases}$$

and B_m is given by (24). The solution of the above system of equations yields pulse amplitudes a_n, from which the current distribution may be constructed. Natural modes are found by a numerical root search of (25) when the forcing term vanishes, e.g.:

$$\det[K_{mn}] = 0.$$

4.2.2 SEPARATION OF THE HALLEN EQUATION FOR EVEN/ODD MODE SYMMETRY

HFIE (17) may be separated into even and odd modes with respect to z. It can be shown that both terms of (17) which don't involve C_1 and C_2 are even/odd in z for current K_z even/odd in z. This leads to the conclusion

$$\begin{aligned} C_1 &= 0 \quad \cdots \textit{for } K_z(x,z) = K_z(x,-z) \quad (\textit{even modes}) \\ C_2 &= 0 \quad \cdots \textit{for } K_z(x,z) = -K_z(x,-z) \quad (\textit{odd modes}). \end{aligned}$$

Exploiting symmetry about z=0 leads to the HFIE for even/odd modes,

$$\int_{-w_d}^{w_d}\int_{0}^{l} G_s^{\{e\atop o\}} K_z(\vec{r}')\,dS' = \begin{Bmatrix} C_1\cos(k_c z) \\ C_2\sin(k_c z) \end{Bmatrix} +$$

$$k_c\int_0^z \left[\int_{-w_d}^{w_d}\int_0^l \frac{\partial G_c^{r\{e\atop o\}}}{\partial y} K_z(\vec{r}')\,dS' - \frac{j}{k_c\eta_c}E_z(\vec{r})\right]_{z=z'} \sin[k_c(z-z')]\,dz'$$

where

$$G_s^{\{e\atop o\}}(x,y,z\,|\,x',y',z')) = G_s(x,y,z\,|\,x',y',z') \pm G_s(x,y,z\,|\,x',y',-z')$$

and similarly for the $\dfrac{\partial G_c^r}{\partial y}$ term. Following a procedure similar to that of the last section results in the matrix system

$$\begin{bmatrix} K_{11} & \cdots & K_{1N} \\ \vdots & \ddots & \vdots \\ K_{N1} & \cdots & K_{NN} \end{bmatrix} \begin{bmatrix} a_1 \\ \vdots \\ a_{(N-1)} \\ C_{\{1\atop 2\}} \end{bmatrix} = \begin{bmatrix} B_1 \\ \vdots \\ B_N \end{bmatrix} \tag{27}$$

where

$$K_{mn} = \begin{cases} M_{mn}^{\{e\atop o\}} & \cdots \text{for } \begin{matrix} m=1,\ \cdots,\ N \\ n=1,\ \cdots,\ N-1 \end{matrix} \\ -2(w_d\pi)\begin{Bmatrix}\cos(k_c z_m)\\ \sin(k_c z_m)\end{Bmatrix}\dfrac{\sin(k_c\delta)}{k_c} & \cdots \text{for } \begin{matrix} m=1,\ \cdots,\ N \\ n=N. \end{matrix} \end{cases}$$

Matrix entries $M_{mn}^{\{e\atop o\}}$ are

and

whe

dim

poly

whe

4.3

to a

dom

$$M^{e}_{nm} = 32\int_0^{\infty} d\zeta \left\{ \cos(\zeta z_n)\cos(\zeta z_m)\frac{\sin^2(\zeta\delta)}{\zeta^2}\left(S_1(\zeta) + \frac{S_2(\zeta)}{(k_c^2-\zeta^2)} \right) \right.$$
$$\left. -\cos(\zeta z_n)\cos(k_c z_m)\frac{\sin(\zeta\delta)}{\zeta}\frac{\sin(k_c\delta)}{k_c}\frac{S_2(\zeta)}{(k_c^2-\zeta^2)} \right\} \tag{28}$$

and

$$M^{o}_{mn} = 32\int_0^{\infty} d\zeta \left\{ \sin(\zeta z_n)\sin(\zeta z_m)\frac{\sin^2(\zeta\delta)}{\zeta^2}\left(S_1(\zeta) + \frac{S_2(\zeta)}{(k_c^2-\zeta^2)} \right) \right.$$
$$\left. -\sin(\zeta z_n)\sin(k_c z_m)\frac{\sin(\zeta\delta)}{\zeta}\frac{\sin(k_c\delta)}{k_c}\frac{\zeta S_2(\zeta)}{k_c(k_c^2-\zeta^2)} \right\} \tag{29}$$

where $S_1(\zeta)$ and $S_2(\zeta)$ are defined by (22). The matrix entries are evaluated as 1-dimensional integrals, where $S_1(\zeta)$ and $S_2(\zeta)$ are approximated by Chebyshev polynomials as was done in the last section. The forcing term B_m is given by (24), where z_m runs over only half of the dipole.

4.3 ENTIRE-DOMAIN BASIS FUNCTION SOLUTION OF THE EFIE FOR MICROSTRIP DIPOLES

In this section, EFIE (4) is solved directly by the MoM, without first converting it to a HFIE. Entire-domain basis and weighting functions are used, to form a entire-domain Galerkin's solution.

For a narrow, z-directed dipole, the scaler EFIE is found from (7) as

$$\left(k_c^2+\frac{\partial^2}{\partial z^2}\right)\int_{-w_d}^{w_d}\int_{-l}^{l}(G^p+G_t^r)K_z(\vec{r}')dx'dz'+\int_{-w_d}^{w_d}\int_{-l}^{l}\frac{\partial^3 G_c^r}{\partial y\partial z^2}K_z(\vec{r}')dx'dz'=-\frac{jk_c}{\eta_c}E_z(\vec{r}). \quad (30)$$

Current $K_z(x,z)$ is expanded in a series of entire-domain functions

$$K_z(x,z) = \sum_{n=1,3,5}^{N}\frac{a_n\cos\left[\frac{n\pi z}{2l}\right]}{\sqrt{1-\left[\frac{x}{w_d}\right]^2}} + \sum_{m=1}^{M}\frac{a_m\sin\left[n\pi\frac{z}{l}\right]}{\sqrt{1-\left[\frac{x}{w_d}\right]^2}} \quad (31)$$

where the first sum involves only odd values of n. Applying the weighting functions

$$W_i(x,z) = \frac{a_i\cos\left[\frac{i\pi z}{2l}\right]}{\sqrt{1-\left[\frac{x}{w_d}\right]^2}}$$

and

$$W_j(x,z)) = \frac{a_j\sin\left[j\pi\frac{z}{l}\right]}{\sqrt{1-\left[\frac{x}{w_d}\right]^2}}$$

result in a linear matrix system which may be solved for the current amplitudes.

Current expansion (31) was chosen because each term in the sum closely models a natural-mode current distribution. Pozar [48] used similar entire-domain basis functions for the study of rectangular antennas, and found that good results were obtained with only one or two modes. This was also found to be the case for the work described here, and so as an example a two-term solution is described below.

For a current modeled as the first two even-mode (or odd-mode) terms of (31), the 2x2 matrix system is obtained as

$$\begin{bmatrix} A_{11} & A_{12} \\ A_{21} & A_{22} \end{bmatrix} \begin{bmatrix} a_1 \\ a_2 \end{bmatrix} = \begin{bmatrix} B_1 \\ B_2 \end{bmatrix} \tag{32}$$

where matrix entries are

$$A_{ij} = \int_0^{\infty} \int_0^{\frac{\pi}{2}} d\theta \, d\lambda \; 4(w_d \pi)^2 J_0^2[\lambda \cos(\theta) w_d] P_{ij}^{\{e\}} \lambda \cdot \frac{k_c^2(1+R_t) + \lambda^2 \sin^2(\theta)(p_c C - R_t - 1)}{2(2\pi)^2 p_c} \tag{33}$$

The above integrals have been converted to polar form by the transformation (2.28). This was found to be the most efficient integration technique when only a few matrix entries need to be evaluated. The term P_{ij} is defined as

$$P_{11}^{e} = I_1(1,\lambda) I_1(1,\lambda) \quad P_{11}^{o} = I_2(1,\lambda) I_2(1,\lambda)$$

$$P_{12}^{e} = I_1(1,\lambda) I_1(3,\lambda) \quad P_{12}^{o} = I_2(1,\lambda) I_2(2,\lambda)$$

$$P_{21}^{e} = I_1(3,\lambda) I_1(1,\lambda) \quad P_{21}^{o} = I_2(2,\lambda) I_2(1,\lambda)$$

$$P_{22}^{e} = I_1(3,\lambda) I_1(3,\lambda) \quad P_{22}^{o} = I_2(2,\lambda) I_2(2,\lambda)$$

with

$$I_1(n,\lambda) = \frac{(n\pi l)\sin\left(\frac{n\pi}{2}\right)\cos[\lambda \sin(\theta) l]}{\left[\frac{n\pi}{2} + \lambda \sin(\theta) l\right]\left[\frac{n\pi}{2} - \lambda \sin(\theta) l\right]}$$

$$I_2(n,\lambda) = \frac{j(-1)^n(2nl\pi)\sin[\lambda\sin(\theta)l]}{[n\pi + \lambda\sin(\theta)l][n\pi - \lambda\sin(\theta)l]}.$$

The above results were presented without detail or intermediate steps, but are derived in a fashion similar to the HFIE equations. The evaluation of the forcing function B_i is similar to that of the coupling coefficient presented in Chapter 3, and is given by

$$B_i = -\frac{jk_c}{\zeta_c}\int_0^{\infty}\left\{J_0(\alpha_1 w_d)e^{j\zeta d}\,T_i^{\{e\}_o}(\alpha_3)[\sin(\theta)Y(\zeta)+\cos(\theta)F(\zeta)]\right. \tag{34}$$
$$\left. + J_0(\alpha_2 w_d)e^{-j\zeta d}\,T_i^{\{e\}_o}(\alpha_4)[\sin(\theta)Y(\zeta)-\cos(\theta)F(\zeta)]\right\}d\zeta.$$

where

$$T_1^e(x) = I_1(1,x) \quad T_1^o(x) = I_2(1,x)$$

$$T_2^e(x) = I_1(3,x) \quad T_2^o(x) = I_2(2,x)$$

with α_{1-4}, $Y(\zeta)$, $F(\zeta)$, and $N(\zeta)$ defined in Chapter 3. Natural even/odd resonant modes are obtained by a numerical root-search of the homogeneous equation

$$\det[A_{ij}] = 0.$$

The above example of a two-term current expansion has been generalized to accommodate N terms, with a corresponding increase in matrix size. It has been found that higher order terms contribute very little to the current expansion, and at most a two term current is needed. This is especially true near a natural resonant frequency.

A two-term current which consists of an even-mode term and an odd-mode term has also been investigated. This combination is not very practical for the near resonance

regime, as it was found that the amplitude of the term not associated with that resonance practically vanished, as might be expected.

Other single-term currents were also investigated. These included

$$K_z(x,z) = \frac{\cos(k_\alpha z) - \cos(k_\alpha l)}{\sqrt{1-\left(\frac{w_d}{x}\right)^2}} \tag{35}$$

where $k_\alpha = k_c, k_{eff}$ with k_c being the cover wavenumber and k_{eff} the wavenumber for a homogeneous region of effective permittivity [48].

Since a single term EBF solution requires the least amount of computational effort, it is desired to determine which current, equation (35) or single terms of (31), provides the most accurate results. To compare different single term current functions, a resonant-mode root-search was preformed for the first even resonance, where the film permittivity varies. Table 4.1 contains a comparison between a single even term of (31), denoted as I, and (35) with $\alpha = c$ denoted as II and $\alpha = eff$ denoted by III. Table entries are the normalized complex resonant wavenumbers, $k_o l = (k_r + jk_i)l$, for a 1.0 cm x .01 cm dipole over a dielectric film of thickness t=.05 cm and permittivity ϵ_f=3.78.

Tab

It

res

roc

nu

of

cu

re

the

4.

int

di

Table 4.1: Comparison of resonant wavenumbers obtained by different single-term current distributions

ϵ_f	I	II	III
1.5	(1.335,.00284)	(1.332,.00286)	(1.334,.00288)
3.5	(.9662,.00121)	(.9640,.00123)	(.9660,.00123)
5.5	(.7961,.000640)	(.7945,.000646)	(.7957,.000648)
7.5	(.69277,.000390)	(.6915,.000395)	(.6925,.000395)
9.5	(.62149,.000261)	(.6205,.000265)	(.6212,.000265)

It was found that all three current functions converge to the approximately the same resonant wavenumber. When the cover wavenumber was used in (35), the numerical root-search required two more iterations than either I or III, which required the same number of iterations. Forced response current amplitudes, a_1, a_2, found by the solution of (32) were also found to be approximately the same. It can be concluded that either current I, II, or III could be used to model the desired current distribution. For the remainder of this dissertation, the single-term, entire-domain basis function solution of the EFIE is accomplished with current I.

4.4 COMPARISON OF MOM SOLUTIONS

Two full-wave solutions of equation (4) have been presented, based on different integral equation forms. The Hallen-form integral equation (HFIE), (17), is derived directly from the fundamental electric field integral equation (EFIE), (4). The HFIE is

generally cor

because the H

potential is re

a smoothing e

sensitive to d

adjacent pulse

functions in a

solution of a

Either ty

domain basis

which may re

computation

times.

A benefi

current, if er

relatively un

almost certai

Entire-do

somewhat, fu

For example

functions. Pr

solved by on

generally considered to be a more stable integral equation than the EFIE. This is because the HFIE is based on the vector potential, not on the electric field. The vector potential is related to the integral of the electric field, where the integration tends to have a smoothing effect leading to greater numerical stability. Accordingly, the HFIE is less sensitive to discontinuities in the current expansion, such as is found at the juncture of adjacent pulse-functions. For this reason, pulse-functions are viable for use as expansion functions in a HFIE solution, but may lead to numerical instability when used for the solution of a EFIE.

Either type of integral equation may be solved with either entire-domain or sub-domain basis functions. Sub-domain basis functions often lead to large solution matrices, which may require a large amount of computer time to fill. For problems involving the computation of Sommerfeld integrals, this may lead to prohibitively long computation times.

A benefit of sub-domain basis functions is their ability to correctly model any current, if enough subdivisions are used. Thus, for a problem where the current is relatively unknown, a pulse-function solution along with a convergence study would almost certainly yield the correct current distribution.

Entire-domain basis functions have the advantage that if the current is known somewhat, functions may be chosen to correctly model the current in a very few terms. For example, the resonant modes of the microstrip dipole are very similar to sinusoidal functions. Problems involving frequencies in the resonant frequency regime can be easily solved by one or two terms of sinusoidal functions, such as equation (31).

In sectio

spatial integ

accomplished

rectangular c

the polar-coo

requires eval

approximatin

This process

a considerabl

domain basis

the polar for

entry. As a r

(EBF) soluti

basis functio

In order

for the first e

the film are t

was used, i.e

the real reso

dashed line i

wavenumber

considerable

In section 2.4.2, two different integration schemes were presented to evaluate the spatial integrations associated with the dyadic Green's functions. One method accomplished the integration in polar coordinates, while the other method utilized rectangular coordinates. It was found that when only a few integrations were needed, the polar-coordinate integration is preferable. The rectangular coordinate integration requires evaluating a one-dimensional integral as a function of some parameter, and then approximating (or interpolating) that function as part of the integrand of another integral. This process is not efficient when only a few integrations need to be evaluated. When a considerable number of integrations are to be performed, such as the case with sub-domain basis functions, the rectangular coordinate method is much more efficient than the polar form, since the function approximation is done once and used for each matrix entry. As a result, the polar form integration is used for the entire-domain basis function (EBF) solution of (4), and the rectangular form integration is used for the sub-domain basis function (SBF) solution of (17).

In order to compare the two solutions, a convergence study based on the root-search for the first even resonant mode was undertaken. Physical parameters of the dipole and the film are the same as described in Section 4.3. The even-mode solution of HFIE (17) was used, i.e., the homogeneous solution of (27). Figure 4.2 shows the convergence of the real resonant wavenumber, $k_r l$, as a function of the number of pulses used. The dashed line is the solution of a single term of (31). It can be seen that the real resonant wavenumber converges to a value close to the 1 EBF solution, but requires a considerable number of pulses. Figure 4.3 is a similar plot of the imaginary resonant

wavenumber
single term o
of the EBF s
Additionally
to be

This demons

The con

one or at m
solution met
not be dism
numerical ex
problems ex
dipole orien
resonant fre
of the HFIE
EBF solutio

A furth

4.6 and 4.7
film permitt

wavenumber, where again the dashed line is the solution of the EFIE obtained with a single term of (31). Figures 4.4 and 4.5 are the corresponding plots for the convergence of the EBF solution. It can be seen that excellent results are obtained with a single term. Additionally, the nullspace current amplitudes for the three-term expansion were found to be

$$\begin{bmatrix} a_1 \\ a_2 \\ a_3 \end{bmatrix} = \begin{bmatrix} 1.0000 \\ 0.0160 \\ 0.0084 \end{bmatrix}.$$

This demonstrates that the second and third terms may be neglected.

The convergence study would indicate that, at least for resonant-mode root searches, one or at most a few terms of (31) used in a EBF solution of EFIE (4) is the better solution method. The importance of the sub-domain basis function of HFIE (17) should not be dismissed, though. This solution, along with various root-searches and other numerical experimentation, led to the motivation for current expansion (31). Also, many problems exist for which the current is expected to have an unusual shape, such as a dipole oriented at an arbitrary angle to a source of excitation, and excited away from a resonant frequency. For these types of problems, the sub-domain basis function solution of the HFIE should be performed, and the unknown current quantified so as to see if an EBF solution is appropriate.

A further comparison between the two solution methods is demonstrated in Figures 4.6 and 4.7. These figures show the real and imaginary resonant wavenumber versus film permittivity. The pulse-function solution was the even-mode solution with 20 pulses

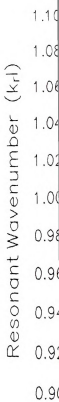
Resonant Wavenumber ($k_r l$)
1.10
1.08
1.06
1.04
1.02
1.00
0.98
0.96
0.94
0.92
0.90

Figure 4.2:

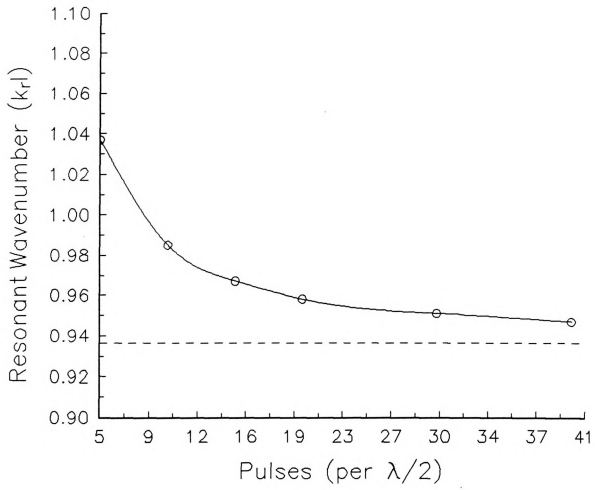

Figure 4.2: Convergence of pulse-function MoM solution for real resonant wavenumber.

x 10
1.86
1.74
1.62
1.50
1.37
1.25
1.13
1.01
0.88
0.76
0.64
Resonant Wavenumber (k1 l)

Figure 4.3:

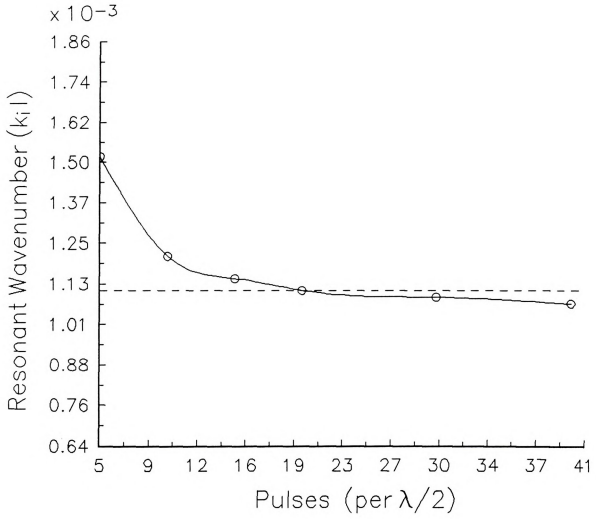

Figure 4.3: Convergence of pulse-function MoM solution for imaginary resonant wavenumber.

Resonant Wavenumber ($k_r l$)
0.950
0.94
0.94
0.93
0.93
0.93
0.92
0.92
0.91
0.91
0.91

Figure 4.4:

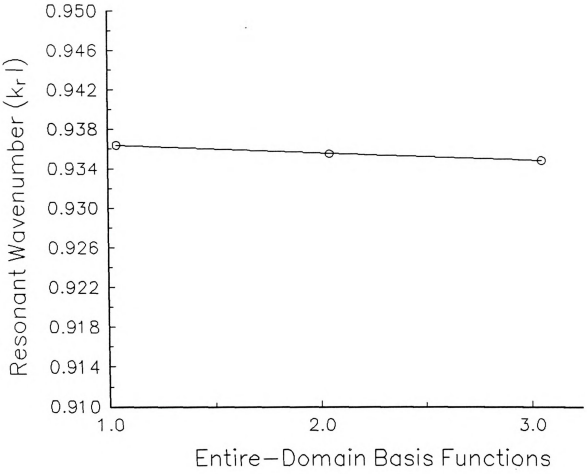

Figure 4.4: Convergence of entire-domain basis function MoM solution for real resonant wavenumber.

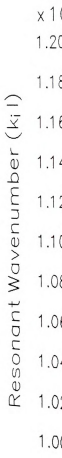
x 1
1.20
1.18
1.16
1.14
1.12
1.10
1.08
1.06
1.04
1.02
1.00
Resonant Wavenumber (k_i l)

Figure 4.5:

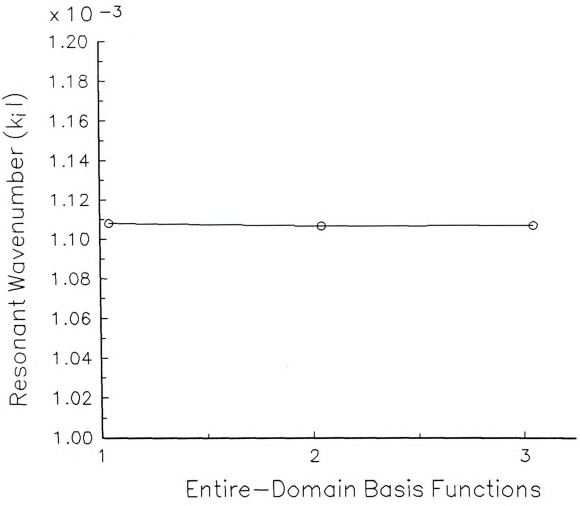

Figure 4.5: Convergence of entire-domain basis function MoM solution for imaginary resonant wavenumber.

per $\lambda/2$, where λ refers to the wavelength in a homogeneous region of effective permittivity ϵ_{eff}. The EBF solution consisted of the first even term of (31). Agreement is seen to good throughout the range of permittivities. This demonstrates that the current is still well-modeled by a single term of (31), as a parameter of the surround environment is varied.

Since the differing solution methods are seen to agree for the homogenous case, a general check on the overall accuracy of the resonant-mode solution is in order. This was accomplished by comparing the solution of the EFIE with an independent solution method.

The resonant modes of coupled, free-space thin cylinders was available for comparison [55]. By considering the film permittivity to be unity, a microstrip dipole over a ground plane can be considered to be two coupled, planer dipoles in free space. Cylindrical and planer antennas can be compared by considering the planer dipole to have an effective radius $a_{eff}=w/2$, where w is the half-width of the planer strip. In this manner, the resonant modes obtained from EFIE (4) can be compared with those obtained by the free-space solution for the anti-symmetric (constrained by the ground plane) mode of a coupled-dipole system. The free-space coupled dipole problem was solved by a pulse Galerkin's solution of a coupled set of EFIE's, which involve the free-space Green's function. Figure 4.8 shows such a comparison, where the real resonant wavenumber is plotted against the imaginary resonant wavenumber, for values of dipole separation ranging from d=0.2 cm up to d=8.0 cm. The plot labeled "microstrip pole" signifies the single-term EBF solution to (4). Agreement is seen to be excellent over the

Figure 4.6:

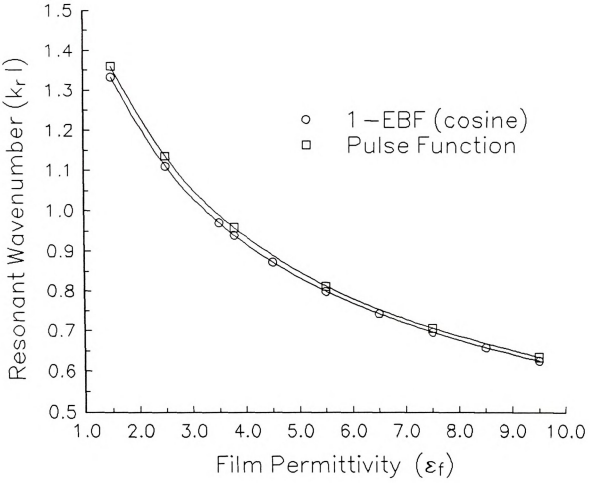

Figure 4.6: Real resonant wavenumber versus film permittivity.

x 1
3.00
2.72
2.44
2.16
1.88
1.60
1.32
1.04
0.76
0.48
0.20
Resonant Wavenumber (kl l)

Figure 4.7:

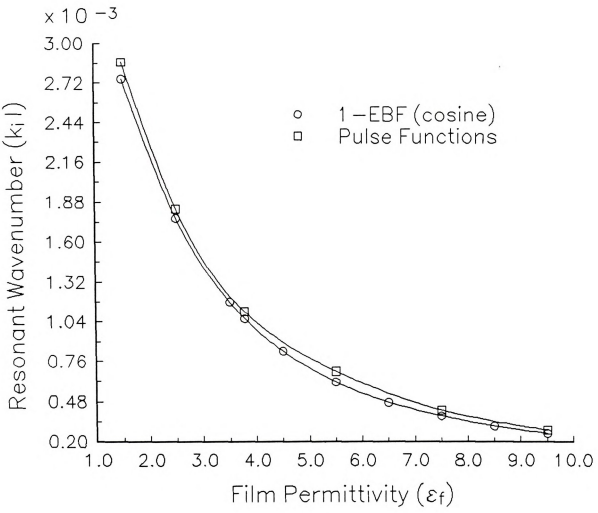

Figure 4.7: Imaginary resonant wavenumber versus film permittivity.

Resonant Wavenumber (k i l)
0.40
0.36
0.32
0.28
0.24
0.20
0.16
0.12
0.08
0.04
0.00

Figure 4.8:

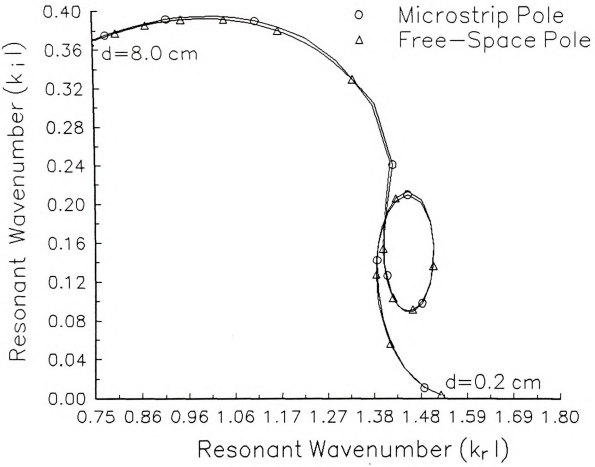

Figure 4.8: Comparison of free-space, coupled dipole natural modes and microstrip modes.

entire rang

signifies th

when ϵ_f=1

Agreem

numerical

integrations

Figure 2.7

solution de

are accurat

integration

the HFIE-b

space solu

verified.

4.5 RES

The sir

in this chap

numerical

with experi

entire range of d. Similar agreement was found with the HFIE-based solution. This signifies that the electric dyadic Green's function (2.24) reduces to the proper result when $\epsilon_f=1.0$.

Agreement between the above solution methods provides a validation check for numerical integrations performed in the solution of IE's (4) and (17). Numerical integrations in the EBF solution follow contours in the complex lambda-plane shown in Figure 2.7. Agreement between the EBF solution and the independent free-space solution demonstrates that the numerical integration methods used in the EBF solution are accurate. The HFIE-based solution follows similar integration contours, although the integration is performed in rectangular coordinates as detailed in Section 2.4.2. Since the HFIE-based solution agrees with the EBF solution, and with the independent free-space solution, accuracy of the rectangular coordinate integration technique is also verified.

4.5 RESULTS

The singularity expansion theory (Chapter 3) and the full-wave methods presented in this chapter should provide results that agree in the resonance regime. In this section, numerical results obtained using the above methods are compared with each other, and with experimental data where applicable.

4.5.1 CU

The SE
of nearly-r
device cur
modeled i
approximat

It was
frequency
modes was
pulse-funct
functions (

The cu
Figure 4.9
transmissio
cm thick w
0%, -5%, a
at resonanc
resonance
amplitude r

Figure
the current

4.5.1 CURRENT DISTRIBUTION

The SEM theory was proposed in Chapter 3 as an efficient method for the analysis of nearly-resonant microstrip device interactions. For this method to be successful, the device current must be modeled accurately. The current on a microstrip dipole was modeled in Chapter 3 with simple sinusoidal functions, and the validity of this approximation is studied here.

It was stated in Chapter 3 that the theoretical current distribution at a natural-mode frequency was very similar to a sinusoid. The current distribution for the first four modes was shown in Figures 3.5, 3.6, and 3.7. These distributions were based on a pulse-function MoM solution of the HFIE, equation (25). It was seen that the sinusoidal functions (3.12, 3.13) closely model the full-wave solution.

The current distribution at several frequencies near resonance is investigated in Figure 4.9, for the case of a parallel-coupled dipole a distance of .75 cm from a transmission line. The dipole is 5.0 cm long and 0.1588 cm wide. The film is 0.0787 cm thick with permittivity (2.2-j.00198). The current at a frequency of +10%, +5%, 0%, -5%, and -10% of resonance is shown, along with the measured current distribution at resonance. It is seen that the current distribution doesn't seem to change from its resonance value, for frequencies at least 10% away from resonance. Beyond 10%, the amplitude response of the dipole is negligible, hence those frequencies aren't of concern.

Figure 4.10 shows the same data for a perpendicular-coupled dipole. It is seen that the current does change slightly with frequency, although at resonance the current

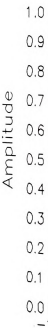

Figure 4.9

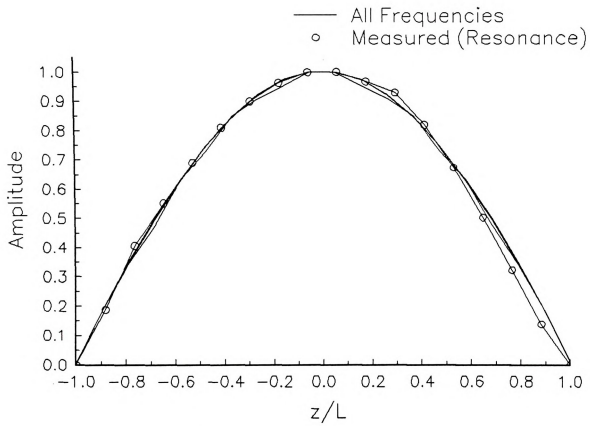

Figure 4.9: Current distribution near first even resonance for a parallel-coupled dipole.

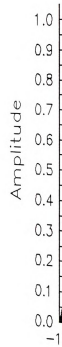

Figure 4.1(

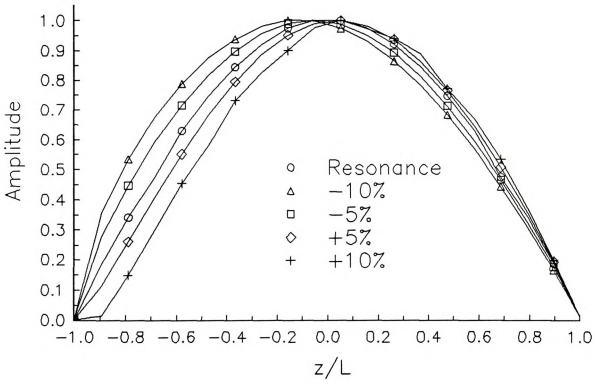

Figure 4.10: Current distribution near first even mode for a perpendicular-coupled dipole.

distribution

frequencies

sinusoidal

4.5.2 FRI

The fre

singularity

presented i

induced cu

cm parallel

a SBF solu

comparisor

function is

Agreement

resonant-m

normalized

resonance.

In orde

the strip c

addition of

term is des

distribution is sinusoidal regardless of orientation. Since the dipole's response at frequencies just 5% away from resonance is practically negligible (see next section), the sinusoidal distribution (3.12) should be sufficient.

4.5.2 FREQUENCY RESPONSE

The frequency dependence of a dipole's surface current is obtained approximately as singularity expansion (3.4). This current should be in agreement with full-wave solutions presented in this chapter, as well as experimental measurements. Figure 4.11 shows the induced current amplitude as a function of normalized cover wavenumber ($k_c l$), for a 1.0 cm parallel-coupled dipole located 1.8 cm from a transmission line. The MoM solution, a SBF solution for even modes of (27), is compared to results from the SEM theory. A comparison between the SEM theory and the EBF MoM solution with one expansion function is shown in Figure 4.12, for the same physical configuration as in Figure 4.11. Agreement between the differing methods of solution is excellent over the entire resonant-mode frequency regime. It should be noted that in both figures, curves were normalized by the same value, which was obtained from the SEM method at the peak of resonance.

In order to compare theoretical and measured results, the imperfect conductivity of the strip conductors must be accounted for. This effect modifies EFIE (4) with the addition of a term involving the skin-effect surface impedance [56]. The addition of this term is described in Appendix E. Figure 4.13 shows the induced current amplitude as

Figure 4.1

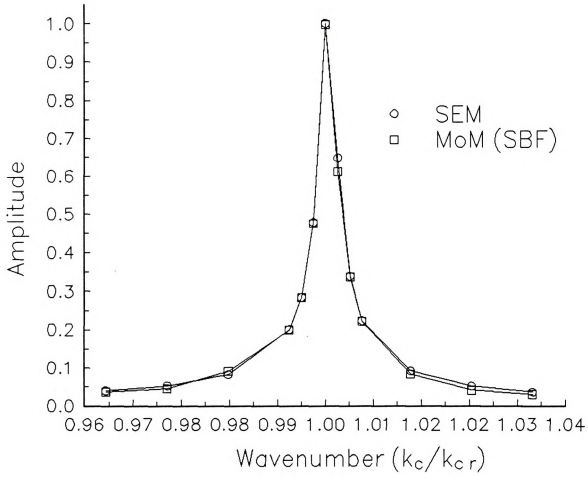

Figure 4.11: Comparison between SEM theory and PF MoM solution for current amplitude vs. wavenumber.

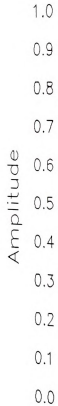

Figure 4.12:

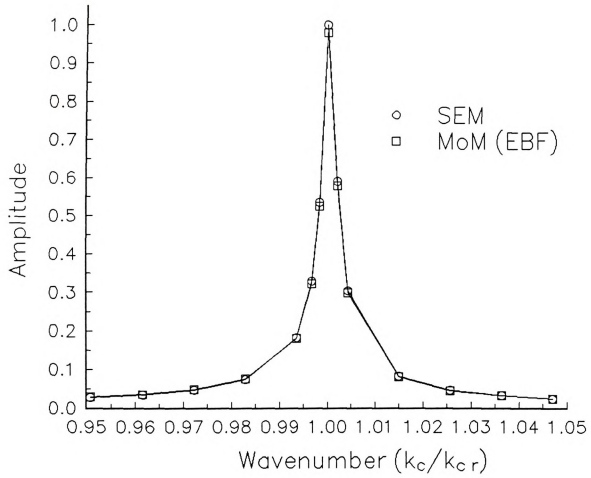

Figure 4.12: Comparison between SEM theory and EBF MoM solution for current amplitude vs. wavenumber.

a function

cm from a

amplitude t

zero surfac

normalized

Agreement

comparison

normalized

then for th

the microst

4.5.3 VA
DI

The va

is also pred

This can

experiment

line is use

experiment

from the t

for the cas

separations

a function of normalized wavenumber for a 5.0 cm parallel-coupled dipole located 1.0 cm from a transmission line. Plots are shown comparing the SEM predicted current amplitude to the measured current amplitude. The theoretical results account for the non-zero surface impedance by the methods of Appendix E. The experimental curve was normalized to unity, and so only the correct bandwidth can be compared with theory. Agreement is seen to be good over the entire frequency range considered. For comparison, theoretical results ignoring the finite surface impedance are included, normalized to unity. It can be seen that the bandwidth of this curve is much narrower then for the others, suggesting that ohmic losses must be considered to properly model the microstrip dipole. This is discussed further in Section 4.5.4.

4.5.3 VARIATION OF DIPOLE CURRENT AS A FUNCTION OF DIPOLE/TRANSMISSION LINE SEPARATION

The variation of dipole current as a function of dipole/transmission-line separation is also predicted by singularity expansion (3.4), through the coupling coefficient term A_p. This can also be compared with results obtained through full-wave methods and experiment. As discussed in Chapter 3, the unperturbed field of an isolated transmission line is used as the approximate excitation in the theoretical methods. It was shown experimentally that this should be a good approximation when the dipole is separated from the transmission line by a sufficient distance, which was found to be fairly small for the case examined. Therefore, theoretical and experimental results should agree for separations beyond that critical value. Figure 4.14 shows the amplitude of a 5.0 cm,

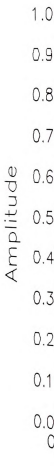

Figure 4.1

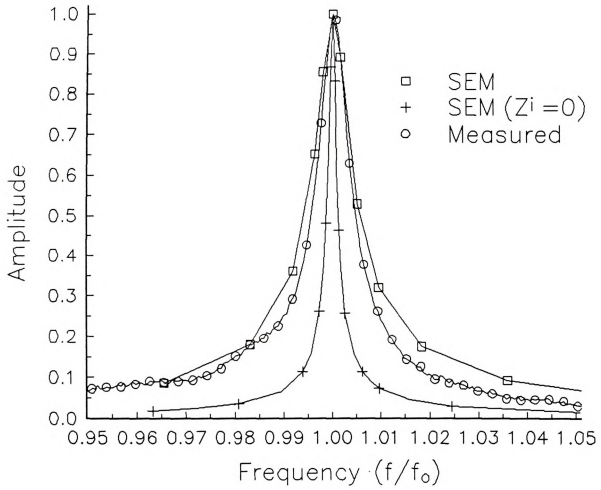

Figure 4.13: Comparison between SEM theory with and without finite conductor impedance accounted for, and measured Q-curve.

parallel-cou

normalized

quality fact

the curves i

then the cri

It shou

of the tran

constant, th

Only the R

This also p

system Q-f

approxima

when norm

Figure

curve was

This was d

for perpen

leave only

4.5.4 LO

Figure

parallel-coupled dipole vs. dipole/transmission-line separation. Each curve was normalized to unity at a separation distance where the dipole/transmission-line system quality factor became within 10% of its isolated value. It is seen that agreement between the curves is good for separations beyond the critical value, and poor for separations less then the critical value, as expected.

It should be realized that the main significance of this figure is to verify the accuracy of the transmission line field, found by equation (3.20). Since the frequency is held constant, the LHS of matrix system (25) or (27) doesn't change with separation distance. Only the RHS, which involves the transmission line's electric field, varies with distance. This also provides complementary verification for monitoring the dipole/transmission-line system Q-factor to indicate when the unperturbed field of the transmission line is a good approximation to the actual impressed field, since the predicted current amplitudes agree when normalized at this critical separation distance.

Figure 4.15 is a similar plot for a perpendicular-coupled dipole. For this case, each curve was set individually to unity at a small value of transmission-line/dipole separation. This was done because the induced current amplitude falls off very sharply with distance for perpendicular-coupled dipoles, and to normalize at a sufficient separation value would leave only a few data points to compare.

4.5.4 LOSS CONSIDERATIONS

Figure 4.13 showed the need for correctly accounting for ohmic losses due to

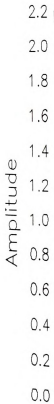

Figure 4.1

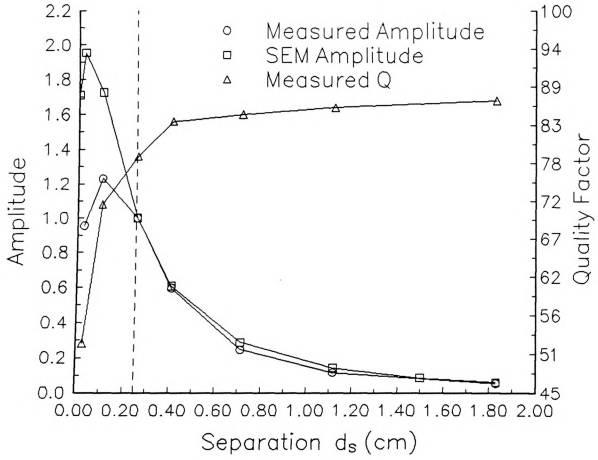

Figure 4.14: Experimental and theoretical current amplitude vs. separation for a parallel-coupled dipole, with measured Q-factor.

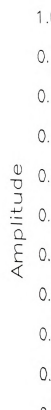

Figure 4.

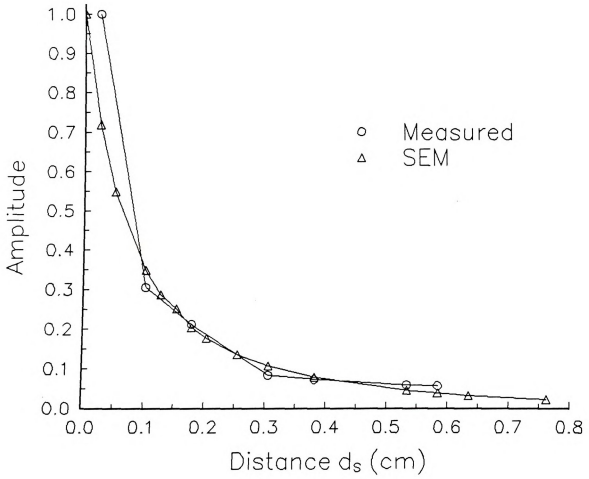

Figure 4.15: Experimental and theoretical current amplitude vs. separation for a perpendicular-coupled dipole.

imperfect

properties

loss, and

effect of v

cm dipole

Table 4.2

Each cas

conductor

finite con

the finite

Appendix

dissipated

Power di

imperfect conductors. By including this effect, and by varying the dielectric film properties, loss mechanisms associated with space and surface-wave radiation, dielectric loss, and conductor loss can be studied. The following table entries demonstrate the effect of varying the film and impedance parameters on resonant wavenumber, for a 5.0 cm dipole over a t=.0787 cm film.

Table 4.2: Effect of dielectric and ohmic loss on the complex resonant wavenumber

ϵ_f	Z^i	$k_o l$	Description
(2.2,0.0)	=0	(1.14196,.000378)	PD, PC
(2.2,0.0)	≠0	(1.13916,.003183)	PD, IC
(2.2,-.00198)	=0	(1.14196,.000802)	ID, PC
(2.2,-.00198)	≠0	(1.13916,.003607)	ID, IC

Each case is given a descriptive set of letters: PD=perfect dielectric, PC=perfect conductor, ID=imperfect dielectric, and IC=imperfect conductor. When $Z^i=0$, the finite conductivity of the copper dipoles was ignored. For the two cases listed as $Z^i \neq 0$, the finite conductivity of the dipoles was accounted for by the methods described in Appendix E. The imaginary wavenumber is related to the Q and hence the power dissipated (P_d) and the energy stored (E_s) by

$$Q = \frac{\omega_r}{2\omega_i} = \frac{\omega_r E_s}{P_d}. \tag{36}$$

Power dissipated is then

Assuming

table, the p

where C =

d=dielectr

the total d

found as

Thus it is

small, wh

resonators

thickness.

which the

where it i

substrates.

$$P_d = 2\omega_1 E_s. \tag{37}$$

Assuming that the stored energy remains constant as parameters are varied in the above table, the power dissipated due to all loss mechanisms is obtained as $P_d^{rscd} = .003607C$ where $C = 2E_s$ and r=space radiation, s=surface-wave radiation, c=conductor loss, and d=dielectric loss. This represents the total power dissipated by the dipole. Normalizing the total dissipated power to unity, dissipated power due to other mechanisms can be found as

1. *PD, PC*: $P_d^{rs} = .1048$
2. *PD, IC*: $P_d^{rsc} = P_d^{rs} + P_d^c \Rightarrow P_d^c = .7777$
3. *ID, PC*: $P_d^{rsd} = P_d^d + P_d^{rs} \Rightarrow P_d^d = .1176$

Thus it is seen that conductor loss is the dominant factor. Radiation losses are very small, which agrees qualitatively with Belohoubek et al. [57], who studied microstrip resonators. It was stated there that radiation increases with increasing substrate thickness. This was verified by increasing the substrate thickness to t=.315 cm, for which the dissipated powers were found to be

1. $P_d^{rs} = .6445$
2. $P_d^c = .2810$
3. $P_d^d = .0749$

1.0

where it is clear that radiation has a dominant effect on the dipole's losses for thicker substrates.

4.5 SU

Full-w

to the SE

equation i

The f

circuits is

equation (

which is

for the di

EFIE

resulting

is solved

expanded

4.5 SUMMARY

Full-wave solutions to the EFIE presented in Chapter 3 are obtained, and compared to the SEM theory. The method of moments (MoM) is used to transform the integral equation into a matrix equation, which can be solved numerically on a computer.

The fundamental EFIE which quantifies electromagnetic interactions in microstrip circuits is solved by two methods. EFIE (4) is transformed into a Hallen-form integral equation (HFIE)

$$\int_S G_s\, K_z(\vec{r}\,')dS' \;=\; C_1\cos(k_c z) + C_2\sin(k_c z) +$$

$$k_c\int_0^z \left[\int_S \frac{\partial G_c^r}{\partial y}K_z(\vec{r}\,')dS' - \frac{j}{k_c\eta_c}E_z(\vec{r})\right]_{z=z'} \sin[k_c(z-z')]dz'.$$

which is solved with a pulse-function, Galerkin's MoM solution. A complete solution for the dipole current is obtained, as well as individual solutions for even/odd modes.

EFIE (4) is also solved directly, without converting to the Hallen form. The resulting equation,

$$\left(k_c^2+\frac{\partial^2}{\partial z^2}\right)\int_{-w_d-l}^{w_d\;\;l}\int (G^p + G_t^r)K_z(\vec{r}\,')dx'dz' + \int_{-w_d-l}^{w_d\;\;l}\int \frac{\partial^2 G_c^r}{\partial y\partial z^2}K_z(\vec{r}\,')dx'dz' = -\frac{jk_c}{\eta_c}E_z(\vec{r})$$

is solved by an entire-domain basis function (EBF) MoM solution. The current is expanded as

$$K_z(x,z) = \sum_{n=1,3,5}^{N} \frac{a_n \cos\left[\frac{n\pi z}{2l}\right]}{\sqrt{1-\left[\frac{x}{w_d}\right]^2}} + \sum_{m=1}^{M} \frac{a_n \sin\left[n\pi \frac{z}{l}\right]}{\sqrt{1-\left[\frac{x}{w_d}\right]^2}}$$

which is used for testing also. It is found that one or at most a few terms of the above current result in good accuracy.

Convergence studies are performed on the various methods of solution, and results obtained with each method are compared. It is found that the EBF solution method is generally preferable for near-resonant frequencies, although the pulse-function solution is more robust for the purpose of correctly modeling the unknown current.

The current induced upon a microstrip dipole by a transmission line is studied, for frequencies corresponding to resonance and near resonance. It is found that the current distribution remains sinusoidal for parallel-coupled dipoles excited up to 10% away from resonance, and that nearly sinusoidal currents were found for perpendicular-coupled dipoles.

Results are presented for the frequency response of the dipole current. Agreement is found to be good between the various solution methods of this chapter, Chapter 3, and experimental methods. The amplitude response of the dipole current as a function of dipole/transmission-line separation is studied by the various methods, where agreement is again found to be good.

Power dissipation is discussed in terms of space and surface-wave radiation, ohmic loss, and dielectric loss. It is found that ohmic losses are dominant for thin substrates, but radiative losses become significant as the substrate thickness increases.

5.1 IN

The p
dipole ex
are studie
is a full-v
will be u
Sectio
devices.
singularit
of EFIE'
modes. T
interact s
isolated
describin

CHAPTER FIVE

COUPLED MICROSTRIP DEVICES

5.1 INTRODUCTION

The preceding chapters described various methods for the analysis of a microstrip dipole excited by a nearby transmission line. In this chapter, coupled microstrip dipoles are studied using an approximate, dominant-mode singularity expansion. Also presented is a full-wave MoM solution for coupled dipoles, which, along with measured results, will be used to validate the coupled-mode perturbation approximation.

Section 5.2 presents the approximate singularity expansion method for coupled devices. The current on any element of the coupled system is approximated by a singularity expansion similar to equation (3.4). Exploiting this current in the coupled set of EFIE's describing the system then leads to the defining relation for natural system-modes. The assumption that only elements with nearly identical resonant frequencies will interact strongly prompts expanding the Green's dyad in a Taylor series about the isolated resonant frequency, leading to an algebraic set of system-mode equations describing the coupled system.

Sectio

with entir

presented

isolated e

accuracy i

Sectio

coupled-d

experimer

"critical s

which res

as the dip

throughou

for separa

5.2 Al

The

environm

The nth di

in Figure

longitudir

Syste

Section 5.3 presents a MoM solution to the coupled-system problem, implemented with entire-domain basis functions (EBF's). Similar full-wave solutions have been presented for rectangular patches by Pozar [48], where it was found that, as in the isolated element case, only one expansion function is required to provide adequate accuracy in the resonance regime.

Section 5.4 presents numerical and experimental results for the investigation of coupled-dipole system-modes. Agreement between the two theoretical methods and experiment is found to be good for dipoles separated by an adequate distance. This "critical separation" is found to be quite small, and can be inferred to be the point at which results from the approximate theory diverge from those of the full-wave theory, as the dipoles are brought together. Experimental results agree with the full-wave theory throughout the entire range of dipole-dipole separations, and with the approximate theory for separations beyond the critical distance.

5.2 APPROXIMATE PERTURBATION THEORY FOR COUPLED DEVICES

The N coupled dipoles are located in the cover layer of a conductor/film/cover environment, at the film/cover interface. The film is of thickness t and permittivity ϵ_f. The n^{th} dipole is of total length L_n and half length l_n. A system of two dipoles is shown in Figure 5.1. The dipoles are separated from each other by transverse distance d_{s1}, and longitudinal distance d_{s2}.

System eigenmodes of an N-dipole system are based upon the coupled set of electric

field integ

for all $\vec{r} \in$

are the co

EFIE's (

multi-dev

5.2.1 N

The s

natural-m

similar fo

mode cur

n^{th} dipole

where ω

amplitud

field integral equations (EFIE's)

$$\hat{t}_m \cdot \sum_{n=1}^{N} \int_{S_n} \vec{G}^{\,e}(\vec{r}|\vec{r}') \cdot \vec{K}_n(\vec{r}')\, dS' = \frac{-jk_c}{\eta_c} \hat{t}_m \cdot \vec{E}^{\,i}(\vec{r}) \qquad (1)$$

for all $\vec{r} \in S_m$, $m = 1, \ldots, N$, where $\hat{t}_m$ is a unit vector tangent to the mth dipole and k_c, η_c are the cover layer wavenumber and refractive index, respectively. The coupled set of EFIE's (1) provide the fundamental resource for the investigation of EM phenomena in multi-device systems.

5.2.1 NATURAL SYSTEM-MODES

The singularity expansion for isolated element currents (3.4) was based upon isolated natural-mode currents $\vec{k}_q(\vec{r})$ and resonant frequencies ω_q. It is reasonable to assume a similar form for the current on each element of a coupled system, where the natural mode current is replaced by $\vec{k}_{nq}(\vec{r})$, the eigenmode current of the qth system mode on the nth dipole. The current on the nth dipole can be approximately represented as

$$\vec{K}_n(\vec{r}, \omega) \approx \sum_q \frac{a_{nq}\, \vec{k}_{nq}(\vec{r})}{(\omega - \omega_q)} \qquad (2)$$

where ω_q is the qth complex natural system-mode frequency and a_{nq} is the natural-mode amplitude. Exploiting expansion (2) in the coupled EFIE's (1) lead to

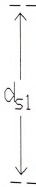

Figure 5

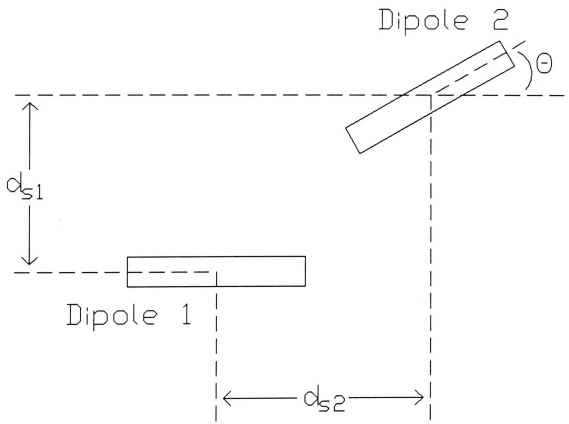

Figure 5.1: A system of two coupled dipoles.

Since $\vec{E}^i$

vanish at

system

with non-

frequency

The

impractic

mode pe

coupled-s

5.2.2 C

Natu

where kn

knowledg

$$\hat{t}_m \cdot \sum_q \frac{a_q}{(\omega - \omega_q)} \sum_{n=1}^{N} \int_{S_n} \ddot{G}^e(\vec{r}|\vec{r}') \cdot \vec{k}_{nq}(\vec{r}')\, dS' = \frac{-jk_c}{\eta_c} \hat{t}_m \cdot \vec{E}^i(\vec{r}).$$

Since $\vec{E}^i$ is regular at $\omega \to \omega_p$ and the LHS has a pole there, the integral sum must vanish at ω_p to produce an indeterminate form. This results in the homogeneous EFIE system

$$\hat{t}_m \cdot \sum_{n=1}^{N} \int_{S_n} \ddot{G}^e(\vec{r}|\vec{r}';\omega) \cdot \vec{k}_{nq}(\vec{r}')\, dS' = 0 \qquad \cdots\ m = 1, \ldots, N \tag{3}$$

with non-trivial solutions for $\omega = \omega_q$, which defines the q^{th} system mode with natural frequency ω_q and element current distributions $\vec{k}_{nq}$.

The direct solution of (3) by the MoM is examined in Section 3, but becomes impractical for systems composed of a large number of interacting devices. A coupled-mode perturbation approximation, based upon the isolated natural-mode currents of coupled-system elements is consequently prompted.

5.2.2 COUPLED-MODE PERTURBATION EQUATIONS

Natural system-mode frequencies ω_q can be obtained from the direct solution of (3), where knowledge of the isolated device characteristics is not required . Alternatively, knowledge of each system element's isolated resonant frequency and current distribution

can be us

The t

is applied

Exploitin

$\vec{k}_{nq} = a_{nq} \vec{k}$

with non-

$\omega = \omega_q$ de

For near

identified

leading t

The lead

can be used to obtain an approximate perturbation solution for system-modes.

The testing operator

$$\int_{S_m} dS\ \vec{k}_{mq}^{(0)}(\vec{r}') \cdot$$

is applied to EFIE's (3), where $\vec{k}_{mq}^{(0)}$ is the resonant current on the mth isolated dipole. Exploiting reciprocity of $\ddot{G}^{e}(\vec{r}|\vec{r}')$ and making use of the coupled-mode approximation $\vec{k}_{nq} \approx a_{nq}\vec{k}_{nq}^{(0)}$ leads to the algebraic set of system-mode equations

$$\sum_{n=1}^{N} C_{mn}^{q}(\omega) a_{nq} = 0 \quad \ldots \ m = 1,2,\ldots,N \tag{4}$$

with non-trivial solutions for current amplitudes a_{nq} only for complex natural frequencies $\omega = \omega_q$ determined from $\det[C_{mn}^{q}(\omega)] = 0$. Coupling coefficients C_{mn}^{q} are identified as

$$C_{mn}^{q}(\omega) = \int_{S_n} dS'\ \vec{k}_{nq}^{(0)}(\vec{r}') \cdot \int_{S_m} \ddot{G}^{e}(\vec{r}'|\vec{r};\omega) \cdot \vec{k}_{mq}^{(0)}(\vec{r})\, dS. \tag{5}$$

For nearly-identical dipoles, the operating frequency regime of significant interaction is identified as $\omega \approx \omega_{mq}^{(0)} \approx \omega_{nq}^{(0)}$. A Taylor's series expansion of $\ddot{G}^{e}$ about $\omega_{mq}^{(0)}$ is prompted, leading to

$$C_{mn}^{q}(\omega) = \int_{S_n} dS'\ \vec{k}_{nq}^{(0)}(\vec{r}') \cdot \int_{S_m} \left[\ddot{G}^{e}(\vec{r}'|\vec{r};\omega_{mq}^{(0)}) + \left.\frac{\partial \ddot{G}^{e}}{\partial \omega}\right|_{\omega_{mq}^{(0)}} (\omega - \omega_{mq}^{(0)}) + \cdots \right] \cdot \vec{k}_{mq}^{(0)}(\vec{r})\, dS. \tag{6}$$

The leading term vanishes for n=m, by (3.8) for the resonant current on the mth isolated

device. T

where, by

When $n=$

$(\omega - \omega_{mq}^{(0)},$

Exploitin

mode per

which de

element

Natu

to non-tr

devices,

the avera

device. The coupling coefficient for the n=m term becomes

$$C^q_{mm}(\omega) \approx \bar{C}^q_{mm}\left[\omega - \omega^{(0)}_{mq}\right] \tag{7}$$

where, by reciprocity of $\ddot{G}^e$,

$$\bar{C}^q_{mm}(\omega) \approx \int_{S_m} dS\ \vec{k}^{(0)}_{mq}(\vec{r}) \cdot \int_{S_m} \left.\frac{\partial \ddot{G}^e(\vec{r}|\vec{r}';\omega)}{\partial\omega}\right|_{\omega^{(0)}_{mq}} \cdot \vec{k}^{(0)}_{mq}(\vec{r}')\ dS'. \tag{8}$$

When $n \neq m$, the leading term in (6) is non-vanishing. The term proportional to $(\omega - \omega^{(0)}_{mq})$ is consequently rendered second-order small, leading to

$$C^q_{mn} \approx \int_{S_n} dS'\ \vec{k}^{(0)}_{nq}(\vec{r}') \cdot \int_{S_m} \ddot{G}^e(\vec{r}'|\vec{r},\omega^{(0)}_{mq}) \cdot \vec{k}^{(0)}_{mq}(\vec{r})\ dS. \tag{9}$$

Exploiting equations (7) and (9) in the system-mode equations (4) leads to the coupled-mode perturbation equations

$$[\omega - \omega^{(0)}_{mq}] a_{mq} \bar{C}^q_{mm} + \sum_{n \neq m} C^q_{mn} a_{nq} = 0 \quad \text{... for } m = 1,2,...,N \tag{10}$$

which depend only upon the constant coupling coefficients (8) and (9), and the isolated-element resonant frequency.

Natural system-modes are obtained from the solution of $\det[C^q_{mn}(\omega)] = 0$, which lead to non-trivial solutions for amplitudes a_{nq}. For the case of two nearly-degenerate devices, the system-mode frequency is obtained as $\omega = \bar{\omega} \pm \delta$, where $\bar{\omega} = (\omega_1 + \omega_2)/2$ is the average of the two isolated resonant frequencies and

$$\delta = \sqrt{\Delta^2 + (C_{12}C_{21})^2}$$

with $\Delta =$

For two

$a_2 = \mp a_1$.

the two s

The

isolated d

in the ne

equation

repeated

entries in

developm

(5.22).

5.3 M

The

comparis

The

with $\Delta = (\omega_1 - \omega_2)/2$. The ratio of natural-mode currents is found as

$$\frac{a_2}{a_1} = \frac{\Delta}{C_{12}} \mp \sqrt{\left(\frac{\Delta}{C_{12}}\right)^2 + \frac{C_{21}}{C_{12}}} \ .$$

For two identical elements, $\omega_1 = \omega_2 = \omega_0$ and $C_{12} = C_{21}$ such that $\omega = \omega_0 \pm C_{12}$ and $a_2 = \mp a_1$. These system modes correspond to antisymmetric/symmetric coupling between the two system elements.

The example to be considered is a system of two coupled microstrip dipoles. The isolated dipole current $\vec{k}_{mq}^{(0)}$ is modeled by (3.12, 3.13), which was found to be accurate in the near-resonant frequency regime. The coupling coefficient (8) is identical to equation (3.10) for isolated dipoles, and its implementation, equation (3.15), is not repeated here. For $n \neq m$, coupling coefficient (9) is identical to off-diagonal matrix entries in the single-term EBF solution of the coupled-dipole system of EFIE's. This development is presented in the next section, and the resulting equation is given by (5.22).

5.3 MoM SOLUTION FOR COUPLED DIPOLES WITH EBF'S

The coupled set of EFIE's (1) is solved by an EBF MoM solution, to provide a comparison to the approximate coupled-mode theory presented in the last section.

The current on the n^{th} dipole is expanded in a set of EBF's

resulting

for all $\vec{r} \in$

elements,

operator

which re

$$\sum_{n=1}^{N} \sum_{j=1}^{J} a_{}$$

which is

The

coupled

is of leng

has lengt

coupled

$$\vec{K}_n(\vec{r}) = \sum_{j=1}^{J} a_{nj}\,\vec{K}_{nj}(\vec{r}) \qquad n=1,\ldots,N \tag{12}$$

resulting in

$$\hat{t}_m \cdot \sum_{n=1}^{N} \int_{S_n} \vec{G}^{\,e}(\vec{r}|\vec{r}\,') \cdot \sum_{j=1}^{J} a_{nj}\vec{K}_{nj}(\vec{r}\,')\,dS' = \frac{-jk_c}{\eta_c}\,\hat{t}_m \cdot \vec{E}^{\,i}(\vec{r})$$

for all $\vec{r} \in S_m$, $m = 1, \ldots, N$. It is assumed that each dipole has the same number of current elements, (J). The above system has N equations and NJ unknowns. Testing with the operator

$$\int_{S_m} ds\ \vec{K}_{ml}(\vec{r}) \cdot \qquad \ldots \begin{cases} m = 1, \ldots, N \\ l = 1, \ldots, J \end{cases}$$

which replaces the $\hat{t}_m \cdot$ operation leads to

$$\sum_{n=1}^{N}\sum_{j=1}^{J} a_{nj} \int_{S_m} dS\,\vec{K}_{ml}(\vec{r}) \cdot \int_{S_n} \vec{G}^{\,e}(\vec{r}|\vec{r}\,') \cdot \vec{k}_{nj}(\vec{r}\,')\,dS' = \frac{-jk_c}{\eta_c} \int_{S_m} \vec{K}_{ml}(\vec{r}) \cdot \vec{E}^{\,i}(\vec{r})\,dS \quad \ldots \begin{cases} m = 1, \ldots, N \\ l = 1, \ldots, J \end{cases} \tag{13}$$

which is a $(JN)\,x\,(JN)$ system of equations.

The above system of equations is solved to determine the system resonances of two-coupled dipoles. Consider the coupled dipole system shown in Figure 5.2. Dipole one is of length $2l_1$, width $2w_{d1}$ and is located at the origin of coordinates x,z. Dipole two has length $2l_2$, width $2w_{d2}$, and is located at the origin of local coordinates (x_1', z_1'). The coupled set of equations (13) become

Figure 5

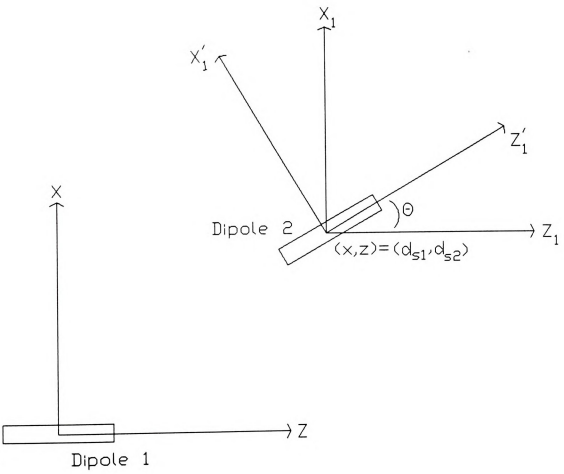

Figure 5.2: Global and local coordinate systems of a two-dipole system.

$$\left[\begin{array}{c|c} \int_{S_1} ds\,\vec{k}_{1l}(\vec{r})\cdot\int_{S_1}\vec{\vec{G}}^{\,e}\cdot\vec{k}_{1j}(\vec{r}')\,ds' & \int_{S_1} ds\,\vec{k}_{1l}(\vec{r})\cdot\int_{S_2}\vec{\vec{G}}^{\,e}\cdot\vec{k}_{2j}(\vec{r}')\,ds' \\ \hline \int_{S_2} ds\,\vec{k}_{2l}(\vec{r})\cdot\int_{S_1}\vec{\vec{G}}^{\,e}\cdot\vec{k}_{1j}(\vec{r}')\,ds' & \int_{S_2} ds\,\vec{k}_{2j}(\vec{r})\cdot\int_{S_2}\vec{\vec{G}}^{\,e}\cdot\vec{k}_{2j}(\vec{r}')\,ds' \end{array}\right]\left[\begin{array}{c} a_{1l} \\ \hline a_{2l} \end{array}\right] = \left[\begin{array}{c} 0 \\ \hline 0 \end{array}\right] \quad \ldots \begin{cases} l = 1,\ldots,J \\ j = 1,\ldots,J. \end{cases}$$

(14)

It should be noted that terms in (14) are represented in block-matrix form. Entries in each block are designated by (l, j), and each block is of size (JxJ). When each dipole's current is modeled with a single term (J=1), (14) will have the form of a 2x2 matrix system.

The diagonal blocks in (14) are found to be the reaction of each dipole with itself. These terms are independent of the position of the other dipoles, and are found to be identical to the (l, j) matrix entries found in the J-term EBF solution for single dipoles presented in Chapter 4. These terms are given by (4.33) for the case of two EBF's. If the two dipoles are identical, the diagonal blocks are the same.

The off-diagonal blocks represent an overlap integral between the current of one dipole and the field due to another dipole, evaluated at the first dipole's location. This relationship can be written as

$$\int_{S_\alpha} ds\,\vec{k}_\alpha(\vec{r})\cdot\int_{S_\beta}\vec{\vec{G}}^{\,e}\cdot\vec{k}_\beta(\vec{r}')\,ds' \propto \int_{S_\alpha} ds\,\vec{k}_\alpha(\vec{r})\cdot\vec{E}_\beta(\vec{r})$$

where $\vec{E}_\beta$ is the field due to the β^{th} dipole and $\vec{k}_\alpha$ is the current on the α^{th} dipole. To evaluate the above, the field of dipole β is found in terms of a local coordinate system,

and then translated to the coordinate system of the α^{th} dipole. This results in elementary evaluation of the spatial integrals associated with EBF's such as (4.31).

As an example of evaluating an off-diagonal term, consider dipole β to be positioned at the origin of local coordinates x_1', z_1', $\vec{r}_1{}' = \hat{x}_1' x_1' + \hat{z}_1' z_1' + \hat{y}y$, and have current

$$\vec{K}_\beta(\vec{r}_1{}') = \hat{z}_1' K_\beta(\vec{r}_1{}').$$

The electric field (2.21) then becomes

$$\begin{aligned} \vec{E}_\beta(\vec{r}_1{}') = {} & \hat{x}_1' \int_{S''} \frac{\partial^2}{\partial x_1' \partial z_1'} \left(G^p + G_t^r + \frac{\partial G_c^r}{\partial y} \right) K_\beta(\vec{r}_1{}'')\, dS'' \\ & + \hat{z}_1' \int_{S''} \left[k_c^2 (G^p + G_t^r) + \frac{\partial^2}{\partial z_1'^2} \left(G^p + G_t^r + \frac{\partial G_c^r}{\partial y} \right) \right] K_\beta(\vec{r}_1{}'')\, dS'' \end{aligned} \tag{15}$$

where the double-prime notation designates the source-point coordinates, and the y-component of field is not of consequence. Expanding the current as either even EBF's

$$K_\beta^e(x_1', z_1') = \sum_{n=1,3,5}^{N} \frac{a_n \cos\left[\dfrac{n\pi z_1'}{2l}\right]}{\sqrt{1 - \left[\dfrac{x_1'}{w_d}\right]^2}} \tag{16}$$

or odd EBF's

$$K_\beta^o(x_1', z_1') = \sum_{m=1}^{M} \frac{a_m \sin\left[n\pi \dfrac{z_1'}{l}\right]}{\sqrt{1 - \left[\dfrac{x_1'}{w_d}\right]^2}} \tag{17}$$

and exploiting the integral form of Green's dyad terms G_μ^v (2.17) leads to

$$\vec{E}_\beta^{\begin{Bmatrix}e\\o\end{Bmatrix}}(\vec{r}_1{}') = \int_{-\infty}^{\infty}\int d\xi d\zeta \frac{(w_d\pi)}{2(2\pi)^2} J_0(w_d\xi) e^{j\xi x_1'} e^{j\zeta z_1'} \sum_{n=1}^{N} I_{\begin{Bmatrix}1\\2\end{Bmatrix}}(n,l_\beta,\zeta) \left\{\hat{x}_1' \left[\xi\zeta(p_c C - R_t - 1)\right]\right.$$
$$\left. + \hat{z}_1' \left[k_c^2(1+R_t) + \zeta^2(p_c C - R_t - 1)\right]\right\} \tag{18}$$

where for even modes the sum is over odd terms and for odd modes the sum is over all terms. The quantities $I_1(n,l,\zeta)$ and $I_2(n,l,\zeta)$ are defined in Chapter 4 (equation 4.14).

The above field of dipole β can be translated to the coordinate system of dipole α (ie., x,z; $\vec{r} = \hat{x}x + \hat{z}z + \hat{y}y$) by the rotation and translation of coordinates

$$x_1 = x - d_{s1}$$
$$z_1 = z - d_{s2}$$

$$x_1' = (x - d_{s1})\cos(\theta) - (z - d_{s2})\sin(\theta)$$
$$z_1' = (x - d_{s1})\sin(\theta) + (z - d_{s2})\cos(\theta)$$
$$\hat{x}_1' = \hat{x}\cos(\theta) - \hat{z}\sin(\theta)$$
$$\hat{z}_1' = \hat{x}\sin(\theta) + \hat{z}\cos(\theta)$$

resulting in the z-component of field

$$E_{\beta z}^{\begin{Bmatrix}e\\o\end{Bmatrix}}(\vec{r}) = \int_{-\infty}^{\infty}\int d\xi d\zeta \frac{(w_{d2}\pi)}{2(2\pi)^2} J_0(w_{d2}\xi)\, e^{j\chi x}\, e^{j\psi x}\, e^{j\xi(d_{s2}\sin(\theta) - d_{s1}\cos(\theta))}$$
$$e^{-j\zeta(d_{s1}\sin(\theta) + d_{s2}\cos(\theta))} \sum_{n=1}^{N} I_{\begin{Bmatrix}1\\2\end{Bmatrix}}(n,l_\beta,\zeta) \left\{-\sin(\theta)\left[\xi\zeta(p_c C - R_t - 1)\right]\right. \tag{19}$$
$$\left. + \cos(\theta)\left[k_c^2(1+R_t) + \zeta^2(p_c C - R_t - 1)\right]\right\}.$$

in terms of the coordinate system associated with dipole α, where

$$\chi = \xi\cos(\theta) + \zeta\sin(\theta)$$
$$\psi = \zeta\cos(\theta) - \xi\sin(\theta).$$

Testing with

$$\int_s ds \; \frac{\cos\left[\frac{n\pi z}{2l}\right]}{\sqrt{1-\left[\frac{x}{w_d}\right]^2}} \; . \tag{20}$$

for even modes, or

$$\int_s ds \; \frac{\sin\left[n\pi\frac{z}{l}\right]}{\sqrt{1-\left[\frac{x}{w_d}\right]^2}} \; . \tag{21}$$

for odd modes results in the matrix block

$$A_{\alpha\beta}^{\left\{\begin{matrix}e\\o\end{matrix}\right\}} = \int_{-\infty}^{\infty}\int d\xi d\zeta \; \frac{(w_{d2}w_{d1}\pi^2)}{2(2\pi)^2} J_0(w_{d2}\xi)\, J_0(w_{d1}\chi)\, e^{j\xi(d_{x2}\sin(\theta)-d_{z1}\cos(\theta))}\, e^{-j\zeta(d_{z1}\sin(\theta)+d_{x2}\cos(\theta))} \tag{22}$$
$$\sum_{m=1}^{N} I_{\left\{\begin{matrix}1\\2\end{matrix}\right\}}(m,l_\alpha,\psi) \sum_{n=1}^{N} I_{\left\{\begin{matrix}1\\2\end{matrix}\right\}}(n,l_\beta,\zeta) \; \{-\sin(\theta)\left[\xi\zeta(p_c C - R_t - 1)\right]$$
$$+\cos(\theta)\left[k_c^2(1+R_t)+\zeta^2(p_c C - R_t - 1)\right]\}.$$

Other matrix entries are evaluated in a similar manner. It can be seen that each matrix block is the reaction between two dipoles, or one dipole with itself, and doesn't involve any other dipoles that may be present. Thus, (14) may be easily generalized for N dipole systems by adding the appropriate blocks, which will be of the same form as those in (14).

All matrix entries are converted to polar coordinates in the spectral plane, which was found to be the most numerically efficient form if only a few integrations need to be performed. The polar coordinate transform was originally discussed in Section 2.4.2.

5.4 NUMERICAL AND EXPERIMENTAL RESULTS FOR COUPLED DIPOLES

The approximate, coupled-dipole perturbation theory should agree with the full-wave MoM solution for various systems of coupled dipoles. Experimental results are also obtained by methods described in Chapter 6, and a comparison of results is presented in this section. All results obtained with the MoM used 1 EBF. This results in resonant system-modes which agree with experimental results.

The coupled system of two identical, parallel coupled dipoles has been investigated. The physical configuration is shown in Figure 5.2, where $d_{s2}=0$, $\theta=0$ degrees, and d_{s1} varies. The dielectric film has permittivity $\epsilon_f=2.20-j.00198$ and thickness t=.0787 cm. Two L=5.0 cm dipoles of width $w_d=.0784$ cm are located on the film layer, separated by a distance d_{s1}. Figure 5.3 shows the real resonant system wavenumber, normalized by the isolated resonant wavenumber, as a function of d_{s1}. All three methods (approximate perturbation, full-wave MoM, and experimental) agree very well for separations beyond a "critical separation" distance of about .25 cm. For separations less then this critical value, all three methods agree for the symmetric modes (bottom set of curves), but do not agree for the antisymmetric modes (top set of curves). For the antisymmetric modes, the perturbation approximation diverges from the MoM and

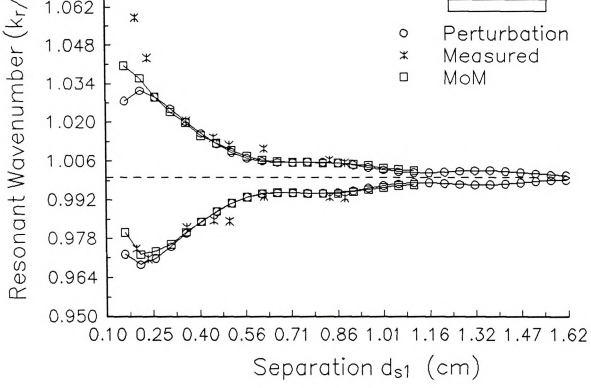

Figure 5.3: System-modes for two identical, parallel coupled dipoles.

experimental results, whereas the latter two agree qualitatively though not quantitatively. It is sensible that the perturbation approximation breaks down for very close spacings, since the currents on the coupled-dipoles are expected to be significantly perturbed from their isolated states. It is also reasonable that the symmetric mode would be easier to model for small dipole-dipole separations, since this configuration is analogous to one thicker dipole. Two closely spaced dipoles at the anti-symmetric mode frequency have equal but opposite currents, and a complicated interaction is expected. It should be noted that the theoretical curves were normalized to the same isolated resonant wavenumber, and the experimental points were normalized to the measured isolated resonant wavenumber. These isolated wavenumbers differed by 1.42%.

Figure 5.4 is a 3-dimensional plot of the current amplitude on one dipole of a two-coupled-dipole system versus separation and frequency. This data was obtained experimentally for the system of identical, parallel-coupled dipoles considered above. It is seen that the symmetric/antisymmetric modes are clearly discernable for small separations, and that there is little response at other frequencies. As the dipole-dipole separation (d_{s1}) increases, the frequencies of the two modes coalesce into a single frequency, that of the isolated dipole.

As a further study of parallel-coupled dipoles, resonant system-modes are studied at a fixed transverse separation, d_{s1}=.16 cm, as longitudinal separation d_{s2} is varied. All other physical parameters are the same as in the above. Figure 5.5 shows symmetric/antisymmetric modes versus longitudinal separation. It can be seen that the mode-splitting increases initially, and as the separation is further increased, the modes

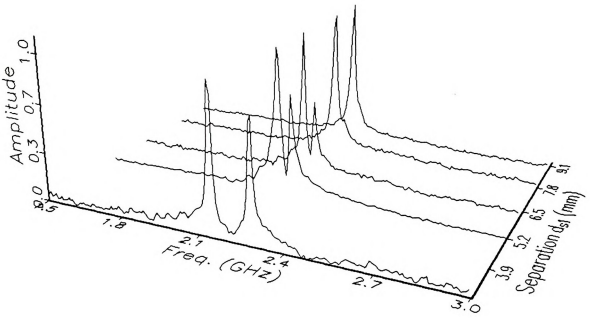

Figure 5.4: Measured parallel-coupled dipole response vs. frequency and separation.

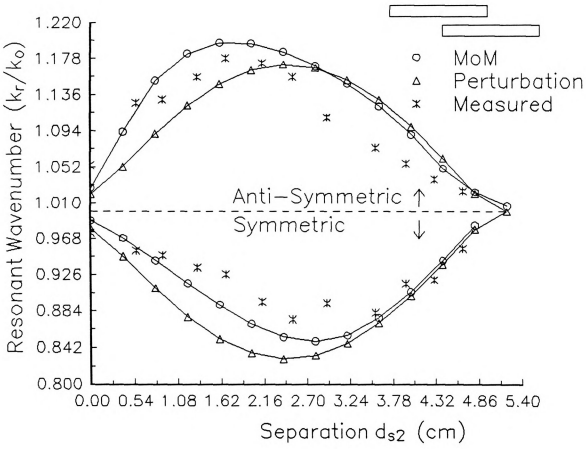

Figure 5.5: Resonant wavenumber vs. longitudinal separation d_{s2}.

approach the isolated resonant mode, which is represented by the dashed line. This is in agreement with physical intuition, since for sufficient separations the two dipoles do not overlap each other at all, and little coupling would be expected.

Figure 5.6 shows the real resonant system wavenumber versus dipole separation d_{s1}, for two parallel-coupled, unequal dipoles. The plot is normalized by the average of the isolated dipole's system wavenumbers. The physical parameters are the same as in Figure 5.3, except that the two dipoles have length L_1=5.0 cm and L_2=4.5 cm. It is seen that the system-mode wavenumbers are split symmetrically about the average wavenumber, corresponding to symmetric/antisymmetric coupling. Again, results from all three methods agree for the symmetric mode, but the perturbation approximation disagrees with the experimental and measured results for the antisymmetric mode at very small separations.

The system-mode resonances of two coupled dipoles is shown in Figure 5.7, as the angle between them varies. The longitudinal displacement is d_{s2}=2.6 cm, and the transverse separation is d_{s1}=-.16 cm. The relative angle between the dipoles, θ, is varied from 0 to 70 degrees. All other physical parameters of the board and dipoles are the same as in Figure 5.3. It can be seen that the maximum coupling exists between dipoles when θ=0 degrees, and that the coupling decreases as θ increases until the dipoles are virtually uncoupled. The resonant system wavenumber is normalized by the isolated dipole's resonant wavenumber, k_o.

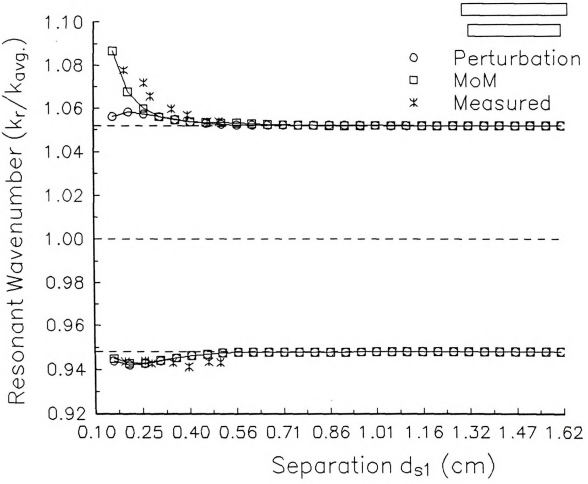

Figure 5.6: Resonant system-modes for non-identical, parallel-coupled dipoles.

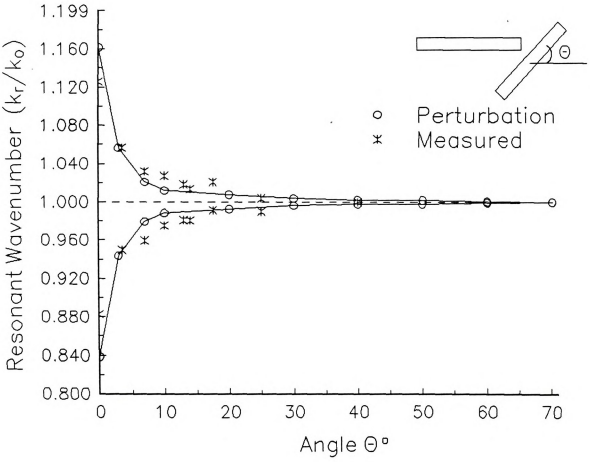

Figure 5.7: Resonant system-modes as the relative angle between two dipoles is varied.

5.4 SUMMARY

Resonant system-modes of coupled microstrip dipoles are studied. A perturbation theory is developed based on the coupled set of EFIE's which rigorously describe the system.

The current on the n^{th} dipole can be approximately represented as

$$\vec{K}_n(\vec{r},\omega) \approx \sum_q \frac{a_{nq}\ \vec{k}_{nq}(\vec{r})}{(\omega-\omega_q)} \tag{23}$$

where ω_q is the q^{th} complex, natural system-mode frequency and a_{nq} is the natural-mode amplitude. The above current is utilized in the coupled set of EFIE's (1), leading to the defining relation for natural system-modes

$$\hat{t}_m \cdot \sum_{n=1}^{N} \int_{S_n} \vec{\bar{G}}^e(\vec{r}|\vec{r}';\omega) \cdot \vec{k}_{nq}(\vec{r}')\, dS' = 0 \qquad \cdots\ m = 1,\ldots, N \tag{24}$$

with non-trivial solutions for $\omega = \omega_q$, which defines the q^{th} system mode with natural frequency ω_q and current distribution $\vec{k}_{nq}$.

Coupled-mode perturbation equations are developed by testing the coupled set of homogeneous EFIE's (24) with

$$\int_{S_m} dS\ \vec{k}_{mq}^{(0)}(\vec{r}') \cdot$$

where $\vec{k}_{mq}^{(0)}$ is the resonant current on the m^{th} isolated dipole. Exploiting the coupled-

mode approximation $\vec{k}_{nq} \approx a_{nq} \vec{k}_{nq}^{(0)}$, and expanding the Green's kernel in a Taylor's series about the isolated element's resonant frequency, leads to the perturbation equations

$$[\omega - \omega_{mq}^{(0)}] a_{mq} \bar{C}_{mm}^{q} + \sum_{n \neq m} C_{mn}^{q} a_{nq} = 0 \quad \text{... for } m = 1, ..., N \tag{25}$$

where $\bar{C}_{mm}^{q}$ and C_{mn}^{q} are coupling coefficients which depend only on the isolated element's resonant frequency and current distribution.

A MoM solution of EFIE's (1) with entire-domain basis functions is presented, to provide a comparison to the perturbation approximation. A numerical root-search provides system resonant frequencies. It is found that the approximate perturbation theory leads to results which generally agree well with the MoM solution. The perturbation theory requires significantly less computational time then the full MoM solution, and thus was found to be an efficient technique.

Measurements are made to validate both methods. Experimental results are found to agree with the two theoretical solutions.

CHAPTER SIX

EXPERIMENTAL METHODS

6.1 INTRODUCTION

Experimental methods used in the investigation of the electromagnetic properties of integrated electronic devices are presented in this chapter. Experimental measurements have been made in order to: i) investigate an isolated dipole's EM characteristics, ii) quantify the dipole/transmission-line separation needed to neglect secondary coupling effects, iii) validate the approximate dominant-singularity-based analysis of transmission-line/dipole coupling and iv) confirm the perturbation approximation theory for coupled dipoles. Additionally, the relative merits of different experimental methods is studied and discussed.

Theoretical investigations of microstrip devices (transmission lines, dipoles, etc.) are described in a great many papers, although relatively few describe experimental procedures in great detail. References [58-62] consider this topic, although the main focus of these is microstrip transmission lines.

The experiments were performed on microstrip circuits applied to a printed circuit (PC) board, which consists of a thin dielectric film layer backed by a copper ground plane. The dielectric film was RT/duroid 5880, which is a glass microfiber reinforced

PTFE composite, available from Rogers Corporation. The board was 16″x 10″, with 1/2 oz. electrodeposited copper on one side and unclad on the other. Electrical and physical properties of the board were as follows:

Dielectric constant @ 10 GHz:	2.20 ± 0.02
Loss tangent @ 10 GHz:	0.0009
Dielectric thickness:	0.07874 cm.

Circuit devices were formed on the dielectric film layer with commercially available gum-backed copper tape (manufactured by GC Electronics), in widths of 0.3175 cm and 0.15675 cm. The 0.3175 cm tape was used to form microstrip transmission lines of $Z_0 \approx 42$ ohms. The use of copper tape allows unlimited flexibility in the positioning of circuit elements, while conserving resources. This is especially important for the investigation of the effect of physical separation on coupled dipole performance, which would require many circuit boards to be etched with various dipole-to-dipole separations. It is assumed that EM properties of the copper tape are similar to those of an etched copper conductor.

Two different instruments were used to measure the EM properties of microstrip circuits. A Network analyzer, Hewlett Packard (HP) model 8720B, was used to perform swept frequency measurements of both reflection and transmission parameters. A vector voltmeter, HP model 8508A, was used to perform single-frequency measurements of transmission parameters. The network analyzer was used for all measurements except in the determination of the induced current distribution on the dipole, where the increased sensitivity of the vector voltmeter proved useful. Both of the above instruments have

terminal ports designed for coaxial connections. Hence, some additional circuitry was needed to excite the device-under-test (DUT) and receive its response. This circuitry consisted of small E-field probes, or transmission line segments. The E-field probe was constructed using rigid (solid-jacketed) 50-ohm microcoaxial cable, with .030 inch outside diameter. At one end of the microcoax, approximately 1 mm of the outer jacket was removed, leaving the center conductor and insulation intact, to form an insulated monopole probe. The other end of the microcoax was terminated in a SMA coax connector, to which the measurement instrument's cables were attached. The probe was inserted through holes in the PC-board so that the truncated outer jacket abuts the ground plane, as shown in Figure 6.1. Solder was applied to this joint to insure good electrical contact. The insulated center conductor continues past the ground plane, into the dielectric film layer, to sample the vertical component of electric field. The center conductor was often allowed to protrude into the cover region slightly, which resulted in a stronger received signal then obtained with probes confined to the film region.

Transmission line segments were also used to excite and receive energy from the microstrip dipoles, forming transmission line (T-line) probes [62]. The wider copper tape of width 0.3175 cm was applied to the dielectric film layer to form microstrip transmission line segments of $Z_0 \approx 42$ ohms, as shown in Figure 6.2. Copper tape was not available in widths which would correspond to $Z_0 \approx 50$ ohms. One end of the transmission line was left open, with the open end located a distance d_s from the DUT. The other end terminated in a SMA coaxial connector. The center pin of the connector protruded through a hole in the PC-board into the cover region, piercing the copper tape.

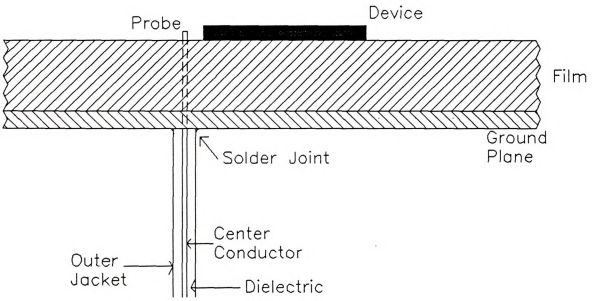

Figure 6.1: E-field probe structure used in measuring microstrip device characteristics.

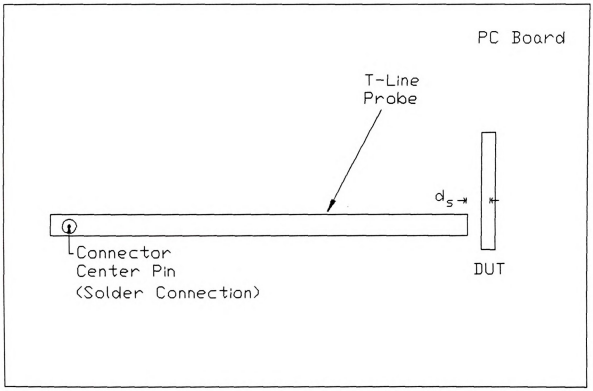

Figure 6.2: T-line probe structure.

Solder was applied to this connection, and also to the connection between the outer conductor of the connector and the ground plane, to insure good electrical contact.

Section 2 describes the study of "isolated" dipole characteristics, such as the natural resonant frequency and quality factor. Different measurement schemes are presented and compared, and some typical results are shown.

Section 3 describes the investigation of transmission-line-fed dipoles. The mutual interactions in a dipole/transmission-line system are assessed by measuring the change in dipole Q as a function of dipole/transmission-line separation. The forced current distribution on the dipole is measured, as well as the relative induced current amplitude. The amplitude and Q-factor are investigated for differing dipole positions and orientations with respect to the transmission line.

Section 4 describes the measurements made to confirm the approximate perturbation theory for coupled dipoles, which was presented in Chapter 5. Swept frequency measurements are made to ascertain the frequency response of a coupled dipole system, allowing for the determination of system-mode frequencies.

6.2 ISOLATED DIPOLE RESONANT CHARACTERISTICS

The experimental study of an "isolated" dipole is intrinsically more difficult then that of a dipole coupled to another device. When making measurements, care must be exercised in order to separate the device's characteristics from those of the measuring system. This is especially true for "isolated" device measurements, since the device can

never be truly isolated from the measurement system. Coupled device systems are generally less sensitive to interactions with the measurement system, since mutual interactions among the individual devices may often dominate over the interactions between a small probe and the circuit devices.

Two characteristics of the isolated dipole were investigated: i) real resonant frequencies and ii) Q-factor, which is related to the imaginary resonant frequency. It was found that the real resonant frequency is an easily measured parameter, and is insensitive to interactions with the measurement system. The Q-factor exhibits considerable sensitivity to dipole/measurement-system interactions, which is expected since this coupling allows power to be transferred from the resonant dipole to the measurement system.

The experimental investigation of the real resonant frequency may be accomplished in a number of ways. E-field probes may be used to excite the dipole, and to receive the dipole's response, or sections of transmission line may be used in place of the E-field probes. Both measurement schemes are depicted in Figure 6.3. Swept frequency measurements of the port-to-port transmission coefficient (S_{21}) are made with the network analyzer. Typical data resulting from this measurement is shown in Figure 6.4, for a 5.0 cm dipole. Peaks of transmission indicate the position of natural modes, at $f_r \approx Re\{f_n\}$, where f_n is the complex natural-mode frequency associated with the isolated dipole. Measured resonant frequencies f_r were found to agree to within 2% of values obtained by the full-wave methods described in Chapter 4. It was found that the real resonant

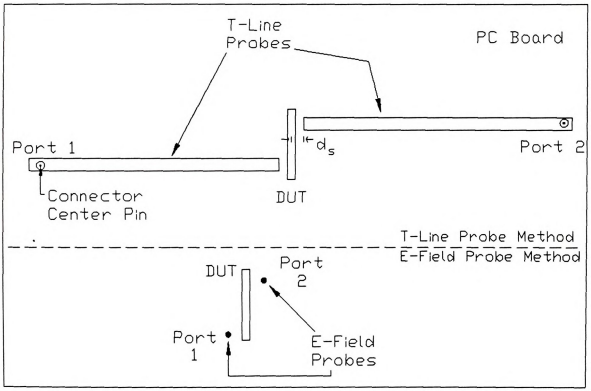

Figure 6.3: Investigation of isolated-dipole resonant frequency and quality factor using T-line and E-field probes.

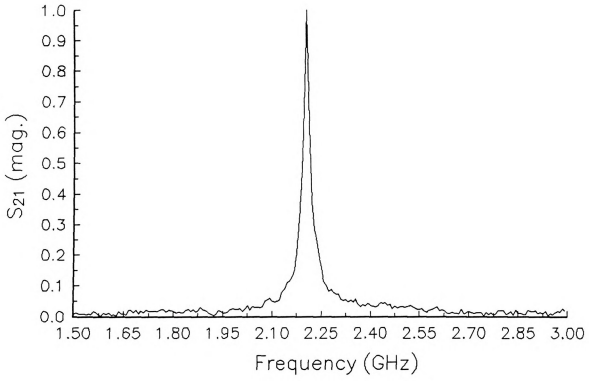

Figure 6.4: Typical results for transmission (S_{12}) measurements made on a isolated microstrip dipole.

frequency (peak of S_{21}) was relatively insensitive to the coupling between measurement probes and the dipole, since increasing the dipole-probe separation did not change the measured resonant frequency. The position of the probe along the dipole (at the dipole's end, center, etc.) did influence which modes were observed. Certain modes, even or odd, would not be "found" for some probe positions, although most probe positions resulted in the observation of most modes.

The approximate placement of the probes to observe a particular mode can be determined by considering the current distribution of the mode of interest. The E-field probe actually provides a voltage proportional to the local charge distribution along the dipole. If the approximate current distribution is known, then the expected charge distribution can be found by

$$\frac{\partial J_z(z)}{\partial z} = -j\omega\rho_s . \tag{1}$$

This indicates that the probes should be placed where the greatest rate of change of the current occurs, since the induced charge will be maximum there. As an example, the current distribution of the first even mode associated with an isolated microstrip dipole is shown in Figure 6.5, obtained by the MoM solution described in Chapter 4 (20 pulses per $\lambda_{eff}/2$). Also shown is the expected charge distribution, obtained by (1). It can be seen that the logical place to position the probes in order to observe the first even mode is near the dipole ends. Similarly, probes should be positioned near the dipole's center to observe the first odd mode, and so on.

The experimental investigation of the Q-factor may accomplished by two

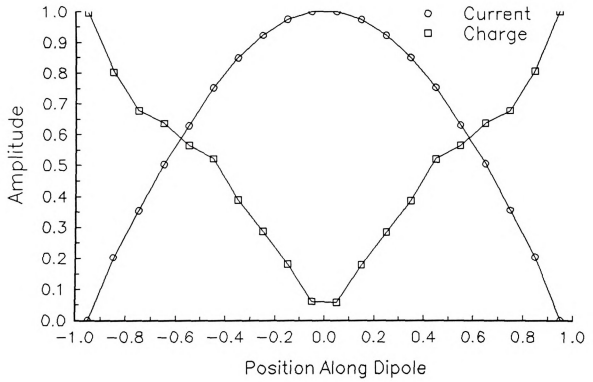

Figure 6.5: Theoretical current and charge distribution (magnitudes) for an isolated microstrip dipole.

fundamentally different methods. One method consists of attempting to critically couple the device to the measurement system [58]. The unloaded Q, Q_o, is then related to the measured Q, Q_l, by $Q_o=2\ Q_l$. This technique suffers from the difficulty of finding the probe position which achieves critical coupling. This is also a fairly narrow-band procedure. Alternatively, measurements may be made on devices that are very loosely coupled to the measurement system, such that $Q_o \approx Q_l$ [58,62]. This procedure is simple and wide-band, although the loose coupling results in low power levels of the measurement signals. A brief comparison of these methods appears in [58] for the investigation of microstrip transmission lines, where it was found that the two methods agreed to within three percent. The latter technique was implemented using transmission line segments as shown in Figure 6.3.

The experimental procedure for determining the isolated dipole's Q is as follows. A dipole of dimensions 5.0 cm x .159 cm was placed on the dielectric film layer. Microstrip T-line probes were located perpendicular to the dipole as shown in Figure 6.3, with their open ends very near the dipole. The probe-to-probe transmission, S_{21}, was measured for frequencies near the real resonant frequency of the device, resulting in a figure similar to Figure 6.4. The Q-factor of the dipole's resonance was recorded. The open ends of both T-line probes were then trimmed back with a razor blade, to increase the probe-to-dipole separation. The new Q-factor was found, and the process repeated until the dipole's Q stopped changing. This Q was then considered the unloaded Q of the dipole, since it was unaffected by further increases in probe-to-dipole separation.

The quality factor of two different dipoles was measured, and compared to theoretical

results. Table 7.1 contains the theoretical resonant wavenumber for two dipoles of different widths, along with the theoretical and measured Q-factor, Q_t and Q_m, respectively. The dipoles were of length L=5.0 cm.

Table 7.1: Theoretical and measured Quality factors

Dipole	$k_o l$	$Q_t = \frac{k_r}{2k_i}$	Q_m	% Δ
w_d=.0794 cm	(1.139,.00360)	157.91	156.8	0.7
w_d=.1588 cm	(1.115,.00309)	180.67	173.5	4.0

The theoretical values were obtained by the EBF MoM solution discussed in Chapter 4, and the finite conductivity of the copper dipoles was accounted for. It can be seen that good agreement was obtained between theory and measurement. Accounting for the finite conductivity of the copper was found to be critical in order to obtain agreement between measurement and theory. For example, the theoretical Q-factor of a perfectly conducting dipole of width w_d=.0794 cm was found to be 711.9, which yields a 78% Δ compared to the actual measured value.

6.3 TRANSMISSION LINE FED DIPOLES

In Chapter 3, the theory of a dipole excited by a microstrip transmission line was developed. The impressed field was assumed to be the unperturbed field of an isolated transmission line, which neglects the secondary coupling effect of nearby objects on the transmission line currents. In this section, the validity of that assumption is examined

experimentally. Techniques to measure the forced current distribution and relative current amplitudes are also presented. Comparisons between measurements and theory have been presented in Chapter 4.

6.3.1 NEGLIGENCE OF SECONDARY COUPLING EFFECTS

It is desired to experimentally quantify the transmission-line/dipole separation needed in order to neglect the secondary coupling of the dipole field with the transmission line. In order to investigate the above, a transmission-line/dipole system was constructed, as shown in Figure 6.6. The transmission line was excited at one end by the center conductor of a coax probe, and the other end was connected to a 50-ohm matched termination through another connector. This resulted in a traveling wave on the transmission line.

The dipole was located near the transmission line, a distance d_s away. An E-field probe was located near the dipole, and the transmission line to dipole transmission (S_{21}) was monitored, beginning with the dipole positioned close to the transmission line. The dipole's Q-factor was recorded. The dipole and E-field probe were then moved as a unit, further away from the transmission line. Care was taken to insure that the dipole-to-probe separation did not change, and that the probe was located at the same point relative to the dipole as previously positioned. The dipole's Q-factor was then found, and the process repeated until the Q-factor stopped changing. Data for this experiment can be found in Figure 3.4.

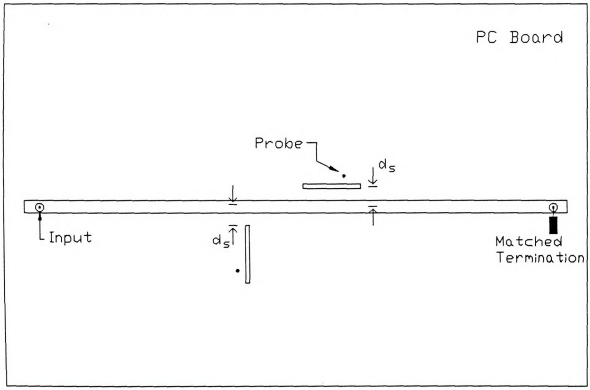

Figure 6.6: Measurement system for the investigation of transmission-line/dipole interactions.

It should be noted that in the above experiment, the actual Q-factor of the transmission-line/dipole system was not being measured, since coupling to the E-field probe was still relatively strong. The relative Q-factor was being measured, as the transmission-line/dipole separation was varied. This is the important quantity in the above experiment, though, and indicates how the transmission line and dipole mutually interact.

6.3.2 FORCED CURRENT DISTRIBUTION

In this section, experimental methods to measure the current distribution induced upon a microstrip dipole by a nearby transmission line are described. Measurements were made using E-field probes, which sample the local charge distribution along the dipole.

The experimental setup is depicted in Figure 6.7. A signal generator provides a sinusoidal steady-state signal to port A of a directional coupler. The input wave is split by the directional coupler, and appears at ports B and C. The output of port C is sent to a vector voltmeter, to provide a voltage reference. The output of port B provides the excitation for a microstrip transmission line, which is terminated in a (nearly) matched load impedance. The resulting EM field of the transmission line excites currents on a nearby microstrip dipole, which is the quantity to be determined. Holes were drilled through the PC board along the length of the dipole, into which E-field probes were inserted. The vector voltmeter monitors the voltage induced upon the probes, where it

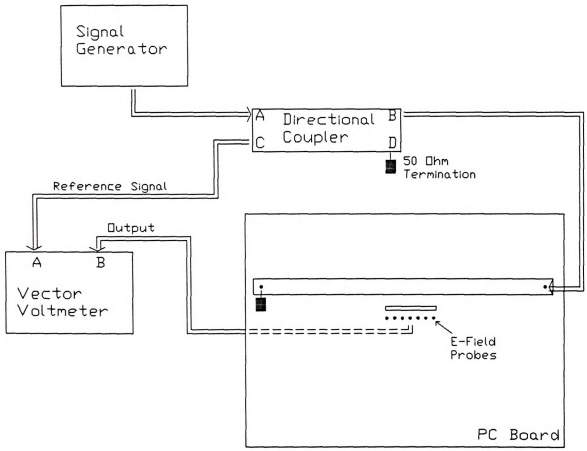

Figure 6.7: Experimental set-up for measuring microstrip dipole current distribution.

was compared with the reference voltage. In this manner, the induced charge on the dipole is measured relative to a reference value, for various positions along the dipole.

A fortran program was written to integrate the charge distribution to provide the desired current, using

$$J_z(z) = -j\omega \int_{\alpha}^{z} \rho_s(z)\, dz. \tag{2}$$

The measured charge was interpolated by a cubic spline [54], and then integrated to yield the current.

The lower limit of integration in (2) was left as α for generality. Let one end of the dipole be at $z=-l$, and the other end at $z=l$, with its center at $z=0$. The charge could be integrated as

$$J_z(z) = -j\omega \int_{-l}^{z} \rho_s(z)\, dz \quad \cdots \textit{for all } z \tag{3}$$

although this method results in errors accumulating as the integration proceeds, and leads to erroneous results for regions z approaching l due to incomplete cancellation (of contributions from the two dipole halves) occurring in the integration. A better method was found to be

$$\begin{aligned} J_z(z) &= -j\omega \int_{-l}^{z} \rho_s(z)\, dz \quad \cdots \textit{for } z \le 0 \\ J_z(z) &= -j\omega \int_{l}^{z} \rho_s(z)\, dz \quad \cdots \textit{for } z > 0 \end{aligned} \tag{4}$$

which does not rely on complete cancellation, at least for the first even mode.

Integrating from two different positions can be thought as providing different phase references for the current, but results in correct magnitudes.

The verification of this method (integration of an interpolated charge distribution) was accomplished by considering some theoretical results obtained from the MoM solution described in Chapter 4. A complex-valued amplitude distribution was obtained for a dipole fed by a transmission line at its resonant frequency. This current distribution was interpolated by a cubic spline, and differentiated to provide the charge using equation (1). This charge profile was compared to the measured charge distribution, where agreement was found to be good. The theoretical charge was then integrated using equations (3) and (4), to obtain the current back again. It was found that equation (3) resulted in nearly correct magnitudes, and correct phases. Equation (4) resulted in correct magnitudes and nearly correct phases, which is expected. In this way, the numerical procedure associated with (3)-(4) was tested, as well as the measurement procedure involving the vector voltmeter to obtain the charge profile.

The experimentally measured current distribution is shown in Figure 4.9, for a parallel-coupled dipole at resonance. The width of the copper tape used to construct the transmission line actually resulted in a 42 ohm transmission line, so some standing waves were expected since the measurement system was 50 ohms. Additionally, reflections will undoubtedly occur at the transition to the microstrip. It was found that these standing waves do not interfere with measurements made at the resonant frequency, although they disturb the induced current distribution at other frequencies. For this reason, measurements were only made at the resonant frequency of the dipole.

6.4 COUPLED DIPOLES

An approximate theory for coupled microstrip devices has been presented in Chapter 5, along with the full MoM solution for coupled dipoles. Natural resonant system modes are found to split about the isolated devices' resonant modes. For the case of two nearly-degenerate dipoles, the system modes can be classified as symmetric and antisymmetric, which refers to the direction of current on the two dipoles. It is the aim of this section to describe the experimental method used to measure these system modes.

The experimental setup for the determination of coupled dipole system modes is shown in Figure 6.8. An E-field probe was used to excite the structure, slightly off center from dipole number 1. A second E-field probe was located near the end of dipole one, and the probe-to-probe transmission was measured. As was the case for isolated dipoles, peaks of transmission indicate the presence of system modes. Typical results of such a measurement are shown in Figure 6.9, for the case of two identical parallel dipoles, L=5.0 cm, separated by d_s=.281 cm. This measurement system allows for freedom in changing the second dipole's position, relative to the first dipole. Since system modes are shared by both dipoles, only one dipole need be monitored, which enables the probe position to remain stationary when the position of the second dipole is changed. Results of these measurements are presented in Chapter 5. It was found that the probe-to-probe transmission vanished when the dipoles were removed, so the measurement system didn't contribute significant errors to the response of the dipoles.

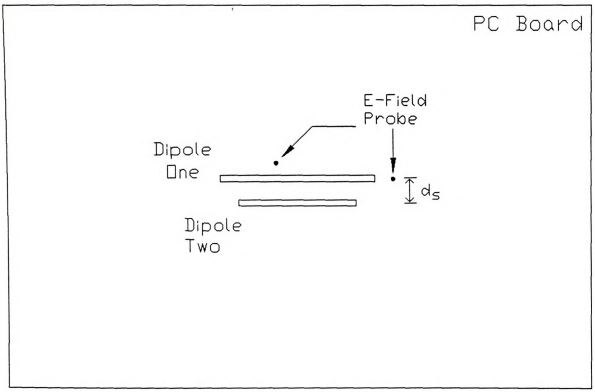

Figure 6.8: Experimental configuration for the investigation of coupled-dipole characteristics.

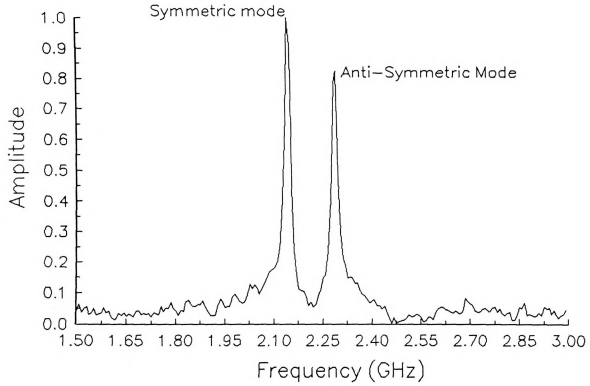

Figure 6.9: System-modes of two coupled, 5 cm dipoles separated by .281 cm.

6.5 SUMMARY

Experimental methods used in the investigation of microstrip dipole properties have been described. Measurements to characterize isolated, coupled, and transmission-line-fed dipoles have been made, using both E-field and transmission line probes.

An isolated dipole's real resonant frequency has been measured, where it was found that the probe type and degree of coupling to the measurement system are relatively unimportant. The quality factor has been measured using transmission line probes, while trying to very loosely couple the dipole to the measuring system. A lack of coupling to the measurement system would, of course, lead to vanishing of the measured signal, so the isolated dipole is characterized by finding the loosest coupling that yields a measurable signal.

Transmission-line-fed dipoles have been studied to determine the separation needed to neglect secondary coupling of the dipole field upon the transmission line. This condition was assessed by measuring the relative Q-factor of the dipole/transmission-line system, as their separation was gradually increased. It was found that the dipole's real resonant frequency changed little as the separation varied, but the Q-factor changed considerably for very close spacings, results for which were presented in Chapter 3. Both parallel and perpendicular coupled dipoles were investigated.

The induced current distribution upon the dipole was examined by measuring the charge distribution along the dipole. The charge was interpolated, and the current was obtained as

$$J_z(z) = -j\omega \int_{\alpha}^{z} \rho_s(z)\, dz$$

where the correct value of α was discussed.

Coupled-dipole system modes were found with swept transmission measurements between E-field probes located near the coupled dipole system. Since the transmission between probes vanished when the dipoles were removed, the response of the measurement system by itself didn't appreciably affect the measurements.

CHAPTER SEVEN

CONCLUSIONS AND RECOMMENDATIONS

An integral-operator formulation for the analysis of the electromagnetic properties of microstrip devices in the near resonant frequency regime has been presented. This approximate theory was proposed as an efficient method of analysis to quantify the dominant interactions in integrated electronic systems. This formulation was based on the rigorous dyadic Green's function which characterizes the layered microstrip environment, and was found to be computationally efficient compared to other full-wave methods. Systems composed of microstrip dipoles were studied as an example of applying the general method.

The dyadic Green's function for tri-layered media was developed in Chapter 2, and a thorough discussion of its singularities in the spectral plane was included. Understanding the physical and numerical implication of these singularities was of utmost importance in correctly evaluating the desired field quantities. Efficient evaluation of the Green's function was discussed, and numerical integration schemes were presented.

In Chapter 3, the singularity expansion method for integrated electronics was developed. This method is based on the conceptually exact electric field integral equation, which quantifies all electromagnetic interactions in integrated electronic

systems. The example of a microstrip dipole excited by a nearby transmission line was considered as representative of a typical application of this method.

Other full-wave methods were developed in Chapter 4. These well-established methods, along with experimental results, were used to validate the approximate singularity expansion theory. Theoretical and experimental results were presented, and found to be in good agreement.

Systems of coupled microstrip devices were considered in Chapter 5. An approximate perturbation theory for coupled devices was presented, and applied to the problem of coupled dipoles. This method was found to be very efficient compared to a full-wave method of moments solution, which was also obtained to provide a comparison to the approximate theory. Theoretical and experimental results were presented and compared, where agreement was found to be good.

Experimental methods used to verify the theoretical results were described in Chapter 6. Various experimental techniques were described and discussed for measuring characteristics of both isolated and coupled systems. Natural resonances were identified, and results were found to agree well with theory. The forced response of a dipole excited by a transmission line was investigated, and the approximations made in developing the singularity expansion description of this problem were discussed.

An approximate, engineering theory for the efficient analysis of dominant interactions in integrated electronic systems was considered. Viability of this method was demonstrated for single devices and small systems. It is proposed that future work examine the feasibility of applying this method to study increasingly complex systems.

The secondary effects of individual system elements on each other is accounted for by the perturbation theory for coupled devices, but does not account for coupling back to the original source of excitation. It is recommended that these interactions be investigated theoretically, and their relative importance assessed.

APPENDIX A

APPENDIX A

ELECTRIC HERTZIAN POTENTIAL

In general, both electric and magnetic potentials may be defined. For the case of no magnetic sources, a single potential is sufficient to uniquely define the fields, which is the circumstance for this dissertation.

Equation (1.b) shows that the divergence of the magnetic field vanishes, demonstrating the nonexistence of magnetic monopoles. This enables us to define

$$\vec{H} = j\omega\epsilon \nabla\times\vec{\Pi}. \tag{A.1}$$

Substitution of (A.1) into (1.c) yields

$$\nabla\times(\vec{E} - k^2\vec{\Pi}) = 0 \tag{A.2}$$

where $k = \omega\sqrt{\mu\epsilon}$. Since the curl of the gradient of a scaler field vanishes, equation (A.2) gives us

$$\vec{E} = -\nabla\phi + k^2\vec{\Pi} \tag{A.3}$$

where ϕ is an arbitrary scaler field. Substitution of equations (A.1) and (A.3) into (1.d) and use of the vector identity

$$\nabla\times\nabla\times\vec{\Pi} = \nabla(\nabla\cdot\vec{\Pi}) - \nabla^2\vec{\Pi} \tag{A.4}$$

results in

$$(\nabla^2 + k^2)\vec{\Pi} = \frac{-\vec{J}}{j\omega\epsilon} + \nabla(\nabla\cdot\vec{\Pi} + \phi). \tag{A.5}$$

Since a vector field is uniquely determined by its curl and divergence, the divergence of $\vec{\Pi}$ must be specified. Choosing $\phi = -\nabla\cdot\vec{\Pi}$, which is the Lorentz gauge, equation (A.3) becomes

$$\vec{E} = \nabla(\nabla\cdot\vec{\Pi}) + k^2\vec{\Pi} \tag{A.6}$$

where $\vec{\Pi}$ is the solution to the non-homogeneous vector Helmholtz equation

$$(\nabla^2 + k^2)\vec{\Pi} = \frac{-\vec{J}}{j\omega\epsilon} \tag{A.7}$$

obtained from (A.5) by use of the gauge condition.

APPENDIX B

APPENDIX B

SPECTRAL REPRESENTATION OF PRINCIPAL GREEN'S DYAD

The Helmholtz equation for the primary component of potential is found in Appendix A to be

$$\nabla^2\vec{\Pi}^p + k^2\vec{\Pi}^p = \frac{-\vec{J}}{j\omega\epsilon} \tag{B.1}$$

which can be written in scaler form as

$$\nabla^2\Pi_\alpha^p + k^2\Pi_\alpha^p = \frac{-J_\alpha}{j\omega\epsilon} \tag{B.2}$$

for α=x,y,z. The Green's function $G^p(\vec{r}|\vec{r}')$ is defined by

$$\nabla^2 G^p(\vec{r}|\vec{r}') + k^2 G^p(\vec{r}|\vec{r}') = -\delta(\vec{r}-\vec{r}') \tag{B.3}$$

where $\delta(\vec{r}-\vec{r}')$ is the Dirac Delta distribution [42]. Without loss of generality, a solution for $G^p(\vec{r}|\vec{r}'=0)$ is sought, and the final result shifted to an arbitrary $\vec{r}'$. Defining the two-dimensional Fourier transform pair

$$G^p(\vec{r}) = \frac{1}{(2\pi)^2}\int\int_{-\infty}^{\infty} g^p(\vec{\lambda},y)\, e^{-j\vec{\lambda}\cdot\vec{r}}\, d^2\lambda \tag{B.4}$$

$$g^p(\vec{\lambda},y)=\int\int_{-\infty}^{\infty} G^p(\vec{r})e^{+j\vec{\lambda}\cdot\vec{r}}dxdz \tag{B.5}$$

where $\vec{\lambda} = \hat{x}\xi + \hat{z}\zeta$ is a 2-D spatial frequency, equation (B.5) is substituted into (B.4), resulting in

$$G^p(\vec{r}) = \int\int_{-\infty}^{\infty} dx'dz' \; G^p(\vec{r}')\frac{1}{(2\pi)^2}\int\int_{-\infty}^{\infty} e^{j\vec{\lambda}\cdot(\vec{r}-\vec{r}')}\, d^2\lambda. \tag{B.6}$$

From the above, it is clear that

$$\frac{1}{(2\pi)^2}\int\int_{-\infty}^{\infty} e^{j\vec{\lambda}\cdot(\vec{r}-\vec{r}')}\, d^2\lambda = \delta(x-x')\,\delta(z-z') \tag{B.7}$$

by the sifting property of delta functions. Use of (B.3), (B.4), and the Fourier transform property

$$\mathcal{F}^{-1}\{\cdots\} = 0 \;\rightarrow\; \{\cdots\} = 0$$

leads to

$$\left[\frac{\partial^2}{\partial y^2} - p^2(\vec{\lambda})\right] g^p(\vec{\lambda},y) = -\delta(y) \tag{B.8}$$

where $p(\lambda) = \sqrt{(\lambda^2 - k^2)}$. The above one dimensional ordinary differential equation for g^p can be easily solved to obtain

$$g^p(\vec{\lambda},y) = \frac{e^{-p|y|}}{2p(\lambda)}. \tag{B.9}$$

Equation (B.4) becomes, after shifting to an arbitrary $\vec{r}'$,

$$G^p(\vec{r}|\vec{r}') = \int\int_{-\infty}^{\infty} \frac{e^{j\vec{\lambda}\cdot(\vec{r}-\vec{r}')}\ e^{-p_c|y-y'|}}{2(2\pi)^2 p_c} d^2\lambda. \tag{B.10}$$

APPENDIX C

APPENDIX C

HERTZIAN POTENTIAL BOUNDARY CONDITIONS AND THEIR APPLICATION

I. Hertzian Potential boundary conditions:

The electric and magnetic fields are found in terms of the Hertzian potential in Appendix A as

$$\begin{aligned} \vec{E} &= (k^2 + \nabla\nabla\cdot)\vec{\Pi} \\ \vec{H} &= j\omega\epsilon\nabla\times\vec{\Pi}. \end{aligned} \tag{C.1}$$

Separating (C.1) into rectangular components yields

$$\begin{aligned} E_{ix} &= k_i^2\Pi_{ix} + \frac{\partial}{\partial x}\nabla\cdot\Pi_i \qquad H_{ix} = j\omega\epsilon_i\left[\frac{\partial\Pi_z}{\partial y} - \frac{\partial\Pi_y}{\partial z}\right] \\ E_{iy} &= k_i^2\Pi_{iy} + \frac{\partial}{\partial y}\nabla\cdot\Pi_i \qquad H_{iy} = j\omega\epsilon_i\left[\frac{\partial\Pi_x}{\partial z} - \frac{\partial\Pi_z}{\partial x}\right] \\ E_{iz} &= k_i^2\Pi_{iz} + \frac{\partial}{\partial z}\nabla\cdot\Pi_i \qquad H_{iz} = j\omega\epsilon_i\left[\frac{\partial\Pi_y}{\partial x} - \frac{\partial\Pi_x}{\partial y}\right] \end{aligned} \tag{C.2}$$

for the i^{th} layer.

Enforcing the continuity of tangential field components of (C.2) as generated by the α^{th} source component individually [17], the general boundary conditions are constructed as

$$\Pi_{1\alpha} = N_{21}^2 \Pi_{2\alpha} \qquad \alpha = x,y,z \tag{C.3.a}$$

$$\frac{\partial \Pi_{1\alpha}}{\partial y} = N_{21}^2 \frac{\partial \Pi_{2\alpha}}{\partial y} \qquad \alpha = x,z \tag{C.3.b}$$

$$\frac{\partial \Pi_{1y}}{\partial y} - \frac{\partial \Pi_{2y}}{\partial y} = -(N_{21}^2 - 1)\left[\frac{\partial \Pi_{2x}}{\partial x} + \frac{\partial \Pi_{2z}}{\partial z}\right] \tag{C.3.c}$$

for the y=0 interface and

$$\Pi_{2\alpha} = N_{32}^2 \Pi_{3\alpha} \qquad \alpha = x,y,z \tag{C.3.d}$$

$$\frac{\partial \Pi_{2\alpha}}{\partial y} = N_{32}^2 \frac{\partial \Pi_{3\alpha}}{\partial y} \qquad \alpha = x,z \tag{C.3.e}$$

$$\frac{\partial \Pi_{2y}}{\partial y} - \frac{\partial \Pi_{3y}}{\partial y} = -(N_{32}^2 - 1)\left[\frac{\partial \Pi_{3x}}{\partial x} + \frac{\partial \Pi_{3z}}{\partial z}\right] \tag{C.3.f}$$

for the y=-t interface, where $N_{ij}=n_i/n_j$ and n_i is the i^{th} layer refractive index.

II. Enforcement of Boundary Conditions to Determine Weighting Coefficients:

The Hertzian potential in each region as given in Chapter 2 can be written in scaler form as

$$\Pi_{1\alpha}(\vec{r}) = \frac{1}{(2\pi)^2}\int\int_{-\infty}^{\infty} e^{j\vec{\lambda}\cdot\vec{r}}\left[\int_V \frac{J_\alpha}{j\omega\epsilon_1}\,\frac{e^{-j\vec{\lambda}\cdot\vec{r}'}e^{-p_1(\lambda)|y-y'|}}{2p_1(\lambda)}dV' + W_{1\alpha}^r(\lambda)e^{-p_1(\lambda)y}\right] d^2\lambda \tag{C.4.a}$$

$$\Pi_{2\alpha}(\vec{r}) = \frac{1}{(2\pi)^2}\int_{-\infty}^{\infty}\int e^{j\vec{\lambda}\cdot\vec{r}}\left[\, W_{2\alpha}^{t}(\lambda)e^{p_2(\lambda)y} + W_{2\alpha}^{r}(\lambda)e^{-p_2(\lambda)y}\,\right] d^2\lambda. \qquad \text{(C.4.b)}$$

$$\Pi_{3\alpha}(\vec{r}) = \frac{1}{(2\pi)^2}\int_{-\infty}^{\infty}\int e^{j\vec{\lambda}\cdot\vec{r}}\left[\, W_{3\alpha}^{t}(\lambda)e^{p_3(\lambda)y}\,\right] d^2\lambda. \qquad \text{(C.4.c)}$$

for $\alpha = x,y,z$ and $Re\{p_i\} > 0$ is chosen to satisfy the radiation condition.

Enforcing boundary conditions (C.3.a), (C.3.b), (C.3.d), (C.3.e) at y=0,-t for tangential components of Hertzian potential leads to the linear system of equations

$$\begin{aligned}
&-W_{1\alpha}^{r} + N_{21}^2(W_{2\alpha}^{t} + W_{2\alpha}^{r}) = V_\alpha \\
&W_{1\alpha}^{r} + \frac{N_{21}^2 p_2}{p_1}(W_{2\alpha}^{t} - W_{2\alpha}^{r}) = V_\alpha \\
&W_{2\alpha}^{t}e^{-p_2 t} + W_{2\alpha}^{r}e^{p_2 t} - N_{32}^2 W_{3\alpha}^{t}e^{-p_3 t} = 0 \\
&W_{2\alpha}^{t}e^{-p_2 t} - W_{2\alpha}^{r}e^{p_2 t} - \frac{N_{32}^2 p_3}{p_2}W_{3\alpha}^{t}e^{-p_3 t} = 0
\end{aligned} \qquad \text{(C.5)}$$

where

$$V_\alpha = \int_V \frac{J_\alpha(\vec{r}')}{j\omega\epsilon_1}\frac{e^{-j\vec{\lambda}\cdot\vec{r}'}e^{-p_1 y'}}{2p_1(\lambda)}\,dV' \qquad \alpha = x,z$$

The system of equations (C.5) is solved to yield

$$\begin{aligned}
W_{2\alpha}^{t} &= \frac{T_{12}^{t}}{D^{t}}V_\alpha \\
W_{2\alpha}^{r} &= \frac{T_{12}^{t}R_{32}^{t}e^{-2p_2 t}}{D^{t}}V_\alpha \\
W_{1\alpha}^{r} &= \left[R_{21}^{t} + \frac{T_{21}^{t}T_{12}^{t}R_{32}^{t}e^{-2p_2 t}}{D^{t}}\right]V_\alpha \\
W_{3\alpha}^{t} &= \frac{T_{12}^{t}T_{23}^{t}e^{(p_3-p_2)t}}{D^{t}}V_\alpha
\end{aligned}$$

where

$$D^t = 1 - R_{12}^t R_{32}^t e^{-2p_2 t}$$

$$\begin{aligned} R_{21}^t &= \frac{p_1 - p_2}{P_1 + p_2}, & R_{12}^t &= \frac{p_2 - p_1}{p_1 + p_2} \\ T_{21}^t &= \frac{2N_{21}^2 p_2}{p_1 + p_2}, & T_{12}^t &= \frac{2p_1}{N_{21}^2(p_1 + p_2)} \\ R_{32}^t &= \frac{p_2 - p_3}{p_2 + p_3}, & T_{23}^t &= \frac{2p_2}{N_{32}^2(p_2 + p_3)} \end{aligned} \tag{C.7}$$

Enforcing boundary conditions (C.3.a), (C.3.d), (C.3.c), and (C.3.f) for normal components of potential leads to the linear system of equations

$$\begin{aligned} -W_{1y}^r + N_{21}^2(W_{2y}^t + W_{2y}^r) &= V_y \\ W_{1y}^r + \frac{p_2}{p_1}(W_{2y}^t - W_{2y}^r) &= V_y + F\left[j\xi V_x + j\zeta V_z\right] \\ W_{2y}^t e^{-p_2 t} + W_{2y}^r e^{p_2 t} - N_{32}^2 W_{3y}^t e^{-p_3 t} &= 0 \\ W_{2y}^t e^{-p_2 t} - W_{2y}^r e^{p_2 t} - \frac{p_3}{p_2} W_{3y}^t e^{-p_3 t} &= -G\left[j\xi V_x + j\zeta V_z\right] \end{aligned} \tag{C.8}$$

where

$$\begin{aligned} F &= \frac{(N_{21}^2 - 1)}{p_1} \frac{T_{12}^t\left[1 + R_{32}^t e^{-2p_2 t}\right]}{D^t} \\ G &= \frac{(N_{32}^2 - 1)}{p_2} \frac{T_{12}^t T_{23}^t e^{(p_3 - p_2)t}}{D^t} e^{-p_3 t} \\ V_y &= \int_V \frac{J_y(r')}{j\omega\epsilon_1} \frac{e^{-j\lambda \cdot r'} e^{-p_1 y'}}{2p_1(\lambda)}\, dV' \end{aligned}$$

and D^t is defined previously.

The system of equations (C.8) is solved to yield

$$W_{2y}^{r} = \frac{T_{12}^{n} R_{32}^{n} e^{-p_2 t}}{D^{n}} V_y + \frac{\left[R_{32}^{n} N_{21}^{-2} C_1 + C_2\right]}{D^{n}} e^{-2p_2 t} \left[j\xi V_x + j\zeta V_z\right]$$

$$W_{2y}^{t} = \frac{T_{12}^{n}}{D^{n}} V_y + \frac{N_{21}^{-2} C_1 - R_{21}^{n} C_2 e^{-2p_2 t}}{D^{n}} \left[j\xi V_x + j\zeta V_z\right]$$

$$W_{1y}^{r} = \left[R_{21}^{n} + \frac{T_{12}^{n} R_{32}^{n} T_{21}^{n} e^{-2p_2 t}}{D^{n}}\right] V_y + \left[C_1 + \frac{T_{21}^{n} (R_{32}^{n} N_{21}^{-2} C_1 + C_2)\, e^{-2p_2 t}}{D^{n}}\right] \left[j\xi V_x + j\zeta V_z\right]$$

$$W_{3y}^{t} = \left\{\frac{T_{12}^{n} T_{23}^{n}}{D^{n}} V_y + \left[N_{32}^{-2} C_2 + \frac{T_{23}^{n} (N_{21}^{-2} C_1 - R_{21}^{n} C_2 e^{-2p_2 t})}{D^{n}}\right] \left[j\xi V_x + j\zeta V_z\right]\right\} e^{(p_3 - p_2)t}$$

where

$$D^{n} = 1 - R_{21}^{n} R_{32}^{n} e^{-2p_2 t}$$

$$R_{21}^{n} = \frac{N_{21}^{2} p_1 - p_2}{n_{21}^{2} P_1 + p_2}, \qquad R_{32}^{n} = \frac{N_{32}^{2} p_2 - p_3}{N_{32}^{2} p_2 + p_3}$$

$$T_{21}^{n} = \frac{2p_2}{N_{12}^{2} p_2 + p_1}, \qquad T_{12}^{n} = \frac{2p_1}{N_{21}^{2} (p_1 + p_2)}$$

$$T_{23}^{n} = \frac{2p_2}{N_{32}^{2} p_2 + p_3}$$

$$C_1 = \frac{N_{21}^{2} (N_{21}^{2} - 1)\, T_{12}^{t}}{N_{21}^{2} p_1 + p_2} \frac{1 + R_{32}^{t} e^{-2p_2 t}}{D^{t}}$$

$$C_2 = \frac{N_{32}^{2} (N_{32}^{2} - 1)}{N_{32}^{2} p_2 + p_3} \frac{T_{12}^{t} T_{23}^{t}}{D^{t}}$$

III. Determination of Hertzian Potential:

Rewriting coefficients in region (1) as

$$W_{1\alpha}^{r} = R_t V_\alpha \qquad \text{(C.10)}$$
$$W_{1y}^{r} = R_n V_y + C\left[j\xi V_x + j\zeta V_z\right]$$

where

$$R_t = R_{21}^t + \frac{T_{12}^t R_{32}^t T_{21}^t}{D^t} e^{-2p_2 t}$$

$$R_n = R_{21}^n + \frac{T_{12}^n R_{32}^n T_{21}^n}{D^n} e^{-2p_2 t} \qquad \text{(C.11)}$$

$$C = C_1 + \frac{T_{21}^n \left[R_{32}^n N_{21}^{-2} C_1 + C_2 \right]}{D^n} e^{-2p_2 t}$$

the total potential may be written as

$$\vec{\Pi}_1 = \vec{\Pi}_1^p + \vec{\Pi}_1^r.$$

Equation (C.10) is substituted into (C.4.a) to yield

$$\vec{\Pi}_1(\vec{r}) = \int_V \ddot{G}(\vec{r}|\vec{r}') \cdot \frac{\vec{J}(\vec{r}')}{j\omega\epsilon_1} dV'$$

where

$$\ddot{G}(\vec{r}|\vec{r}') = \ddot{G}^p(\vec{r}|\vec{r}') + \ddot{G}^r(\vec{r}|\vec{r}')$$

$$\ddot{G}^p(\vec{r}|\vec{r}') = \ddot{I} G^p(\vec{r}|\vec{r}')$$

$$\ddot{G}^r(\vec{r}|\vec{r}') = \hat{x}\, G_t^r \hat{x} + \hat{y} \left[\frac{\partial G_c^r}{\partial x} \hat{x} + G_n^r \hat{y} + \frac{\partial G_c^r}{\partial z} \hat{z} \right] + \hat{z}\, G_t^r\, \hat{z}$$

$$G^p(\vec{r}|\vec{r}') = \int_{-\infty}^{\infty}\int \frac{e^{j\vec{\lambda}\cdot(\vec{r}-\vec{r}')}\, e^{-p_c|y-y'|}}{2(2\pi)^2 p_c} d^2\lambda$$

$$\begin{Bmatrix} G_t^r(\vec{r}|\vec{r}') \\ G_n^r(\vec{r}|\vec{r}') \\ G_c^r(\vec{r}|\vec{r}') \end{Bmatrix} = \int_{-\infty}^{\infty}\int \begin{Bmatrix} R_t(\lambda) \\ R_n(\lambda) \\ C(\lambda) \end{Bmatrix} \frac{e^{j\vec{\lambda}\cdot(\vec{r}-\vec{r}')} e^{-p_c(y+y')}}{2(2\pi)^2 p_c} d^2\lambda.$$

For the case of a conducting region (3) (substrate), the reflection and coupling coefficients become

$$R_t(\lambda) = \frac{p_1 - p_2 \coth(p_2 t)}{Z^h(\lambda)}$$

$$R_n(\lambda) = \frac{N_{21}^2 p_1 - p_2 \tanh(p_2 t)}{Z^e(\lambda)}$$

$$C(\lambda) = \frac{2(N_{21}^2 - 1)p_1}{Z^h(\lambda) Z^e(\lambda)}$$

where

$$Z^e(\lambda) = N_{21}^2\ p_1 + p_2 \tanh(p_2 t)$$

$$Z^h(\lambda) = p_1 + p_2 \coth(p_2 t).$$

APPENDIX D

APPENDIX D

EXISTENCE OF BRANCH POINTS IN THE COMPLEX FREQUENCY PLANE

Singularity expansion (3.3) for unknown surface current $\vec{K}$ is given as a sum of pole terms in the complex frequency plane. This sum of pole singularities constitutes the dominant contribution to the current, although the sum is not a complete representation. Other complex frequency-plane singularities are needed, and a complete representation for the surface current would be

$$\vec{K}(\vec{r},\omega) = \sum_{n=1}^{N} \frac{A_n \vec{k}_n(\vec{r})}{\omega - \omega_n} + \vec{W}(\vec{r},\omega) \tag{D.1}$$

where $\vec{W}(\vec{r},\omega)$ is the contribution from other singularities. It is conjectured here that branch-point singularities are present in the complex frequency-plane, although numerical results indicate that they may not be important when compared with the pole singularities.

The solution of EFIE (3.1) requires the evaluation of the dyadic Green's function presented in Chapter 2. Components of the reflected part of the Green's dyad are given by

$$\begin{Bmatrix} G_t^r(\vec{r}|\vec{r}') \\ G_n^r(\vec{r}|\vec{r}') \\ G_c^r(\vec{r}|\vec{r}') \end{Bmatrix} = \int_0^{\infty}\int_0^{2\pi} \begin{Bmatrix} R_t(\lambda) \\ R_n(\lambda) \\ C(\lambda) \end{Bmatrix} \frac{e^{j(\hat{x}\lambda\cos\theta+\hat{z}\lambda\sin\theta)\cdot(\vec{r}-\vec{r}')}\, e^{-p_c(y+y')}}{2(2\pi)^2 p_c} \lambda d^2\lambda \qquad \text{(D.2)}$$

where $\vec{\lambda} = \hat{x}\xi + \hat{z}\zeta$ is a 2-D spatial frequency with $\lambda^2 = \xi^2 + \zeta^2$ and $d^2\lambda = d\xi d\zeta$. Equation (D.2) is found from (2.17) by the rectangular to polar transformation

$$\begin{aligned} \xi &= \lambda\cos\theta \\ \zeta &= \lambda\sin\theta \end{aligned}$$

Wavenumber parameters are $p_i = \sqrt{\lambda^2 - k_i^2}$ with $Re\{p_i\} > 0$ for i=s,f,c. Coefficients R_t, R_n, and C are given by

$$\begin{aligned} R_t(\lambda) &= \frac{p_c - p_f \coth(p_f t)}{Z^h(\lambda)} \\ R_n(\lambda) &= \frac{N_{fc}^2 p_c - p_f \tanh(p_f t)}{Z^e(\lambda)} \\ C(\lambda) &= \frac{2(N_{fc}^2 - 1)p_c}{Z^h(\lambda) Z^e(\lambda)} \end{aligned}$$

where

$$\begin{aligned} Z^e(\lambda) &= N_{fc}^2\, p_c + p_f \tanh(p_f t) \\ Z^h(\lambda) &= p_c + p_f \coth(p_f t). \end{aligned}$$

Consider preforming the inverse spectral integrals in (D.2) by the method of contour deformation. The integral may be found as a sum of integrations around the poles plus a term resulting from integrating along the branch cut. A representative Green's component of (D.2) may be written as

$$I = \int_0^{2\pi} \int_0^{\infty} \frac{F(\lambda,\theta)}{Z(\lambda)} d\lambda d\theta$$

where the order of integration has been interchanged. $F(\lambda,\theta)$ is the portion of the integrand analytic within and on a circle C_p enclosing the pole at $Z(\lambda)$. Considering the integration around a C_p leads to

$$I = \int_0^{2\pi} \int_{C_p} \frac{F(\lambda,\theta)}{Z(\lambda)} d\lambda d\theta.$$

If contour C_p is made limitingly small, and $F(\lambda,\theta)$ is a well-behaved function in the vicinity of the pole, the above integral may be written as

$$I \approx \int_0^{2\pi} d\theta \; F(\lambda_p,\theta) \int_{C_p} \frac{d\lambda}{Z(\lambda)}. \tag{D.3}$$

The Taylor's series expansion of $Z(\lambda)$ about $\lambda = \lambda_p$ is

$$Z(\lambda) = Z(\lambda_p) + (\lambda - \lambda_p) \frac{\partial}{\partial \lambda} Z(\lambda)\Big|_{\lambda=\lambda_p} + \ldots .$$

Retaining the first non-vanishing term (the leading term vanishes by definition) results in

$$I = \int_0^{2\pi} d\theta \; \frac{F(\lambda_p,\theta)}{Z'(\lambda_p)} \int_{C_p} \frac{d\lambda}{\lambda - \lambda_p} \tag{D.4}$$

where

$$Z'(\lambda_p) = \frac{\partial}{\partial\lambda} Z(\lambda)\Big|_{\lambda=\lambda_p} .$$

The change of variables

$$\lambda - \lambda_p = \epsilon e^{j\psi}$$
$$d\lambda = j\epsilon e^{j\psi} d\psi$$

leads to the second integral in (D.4) being evaluated as $2\pi j$. Integral (D.4) is found to be

$$I = \frac{2\pi j}{Z'(\lambda_p)} \int_0^{2\pi} F(\lambda_p, \theta) d\theta. \tag{D.5}$$

By inspection of (D.2) and (D.5), it is obvious that wavenumber parameters $p_c = \sqrt{\lambda_p^2 - k_c^2}$ are involved in the frequency-domain expression for $I = I(\omega)$ resulting from the surface-wave contribution to the spectral integral. Hence it is shown that branch points are found in the complex frequency-plane. Since (D.5) is only part of the spectral integral evaluation, it is not clear what role these branch points may take. Also, the above derivation was for the Green's function by itself, before it is operated on by the spatial integrals associated with obtaining the electric field. It is assumed that the singularities associated with the Green's dyad are shared by the solution of the integral equation involving $\ddot{G}$.

APPENDIX E

APPENDIX E

MODIFICATION OF THE EFIE TO INCLUDE FINITE CONDUCTOR SURFACE IMPEDANCE

An electric field integral equation (EFIE) is derived by enforcing continuity of tangential electric field components across an interface, such as a conducting surface. Typically, an impressed electric field $\vec{E}^i$ excites currents on surface S, producing scattered field $\vec{E}^s$ and internal field $\vec{E}^{int}$. When S bounds a perfect conductor, $\vec{E}^{int}=0$ and the boundary condition for tangential $\vec{E}$ requires that $\hat{t}\cdot(\vec{E}^i+\vec{E}^s)=0$, where $\hat{t}$ is a unit tangent vector at any point on surface S. If the conductor has finite conductivity, $\vec{E}^{int}=Z^i\vec{K}(\vec{r})$ where $\vec{K}(\vec{r})$ is the total current at point $\vec{r}$ and Z^i is the internal surface impedance. The boundary condition for tangential field components then becomes $\hat{t}\cdot(\vec{E}^i+\vec{E}^s-\vec{E}^{int})=0$, resulting in EFIE

$$\hat{t}\cdot\int_S \vec{\vec{G}}^e(\vec{r}|\vec{r}')\cdot\vec{K}(\vec{r}')\,dS' = -\frac{jk_c}{\eta_c}\hat{t}\cdot\left[\vec{E}^i(\vec{r})+Z^i\vec{K}(\vec{r})\right] \quad ...\forall\ \vec{r}\in S. \tag{E.1}$$

For wires, $E^{int}=Z_l I$ where I is the total current and the impedance per unit length can be found as [56]

$$Z_l = \frac{\mu\omega}{4\pi}\frac{\delta}{a}(1+j) \tag{E.2}$$

where

$$\delta = \sqrt{\frac{2}{\omega\mu\sigma}}$$

is the skin depth, σ =conductivity in (mhos/m), and a=radius of the wire. Equation (E.2) has been found to be accurate when (δ/a) is small, which is often the case for good conductors.

EFIE (E.1) is the same as the fundamental EFIE derived in Chapter 3, with the addition of the surface impedance term. When considering resonance problems ($\vec{E}^i$=0), the term involving Z^i should be subtracted from the LHS, resulting in modification of the resonant wavenumber which reflects the finite conductivity of the object.

As an example of computing $Z^i\vec{K}(\vec{r})$, the single-term, even EBF solution of EFIE (E.1) is considered. All terms are the same as derived in Chapter 4, with the addition of the surface impedance term. For narrow strip dipoles, Z^iK can be replaced by Z_lI on a circular dipole of equivalent radius and the current reduces to $I(z)$, which can be found as

$$I(z) = \int_x J(x,z)dx = \int_{-w_d}^{w_d} \frac{a_0 \cos\left(\frac{n\pi z}{2l}\right)}{\sqrt{1-\left(\frac{x}{w_d}\right)^2}} dx$$

and becomes

$$I(z) = a_0 w_d \pi \cos\left(\frac{n\pi z}{2l}\right).$$

Testing with the integral operator

$$\int_{-w_d}^{w_d}\int_{-l}^{l} \frac{\cos\left(\frac{n\pi z}{2l}\right)}{\sqrt{1-\left(\frac{x}{w_d}\right)^2}} dz dx$$

results in the term

$$T = \frac{-jk_c}{\eta_c}\left[a_0 (w_d \pi)^2 l Z_l\right]$$

which augments the equations that neglect the finite conductor impedance of the conductor.

BIBLIOGRAPHY

BIBLIOGRAPHY

[1] R. E. Munson, "Conformal Microstrip Antennas and Microstrip Phased Arrays," *IEEE Trans. Ant. Prop.*, vol. AP-22, pp. 74-77, Jan. 1974.

[2] Y. T. Lo, D. Solomon, and W. F. Richards, "Theory and Experiment on Microstrip Antennas," *IEEE Trans. Ant. Prop.*, vol. AP-27, pp. 137-145, March 1979.

[3] K. R. Carver and J. W. Mink, "Microstrip Antenna Technology," *IEEE Trans. Ant. Prop.*, vol. AP-29, pp. 2-24, Jan. 1981.

[4] R. J. Mailloux, J. McIlvenna, and N. Kernweis, "Microstrip Array Technology," *IEEE Trans. Ant. Prop.*, vol. AP-29, pp. 25-38, Jan. 1981.

[5] I. E. Rana, and N. G. Alexopoulos, "Current Distribution and Input Impedance of Printed Dipoles," *IEEE Trans. Ant. Prop.*, vol. AP-29, pp. 99-105, Jan. 1981.

[6] M. C. Bailey and M. D. Deshpande, "Integral Equation Formulation of Microstrip Antennas," *IEEE Trans. Ant. Prop.*, vol. AP-30, pp. 651-656, July 1982.

[7] D. M. Pozar, "Considerations for Millimeter Wave Printed Antennas," *IEEE Trans. Ant. Prop.*, vol. AP-31, pp. 740-747, Sept. 1983.

[8] D. M. Pozar, "Analysis of Finite Phased Arrays of Printed Dipoles," *IEEE Trans. Ant. Prop.*, vol. AP-33, pp. 1045-1053, Oct. 1985.

[9] E. Newman, and D. Forrai, "Scattering from a Microstrip Patch," *IEEE Trans. Ant. Prop.*, vol. AP-35, pp. 245-251, Mar. 1987.

[10] W. C. Chew, and Q. Liu, "Resonance Frequency of a Rectangular Microstrip Patch," *IEEE Trans. Ant. Prop.*, vol. 36, pp. 1045- 1056, Aug. 1988.

[11] N. K. Das and D. M. Pozar, "Analysis and Design of Series-Fed Arrays of Printed-Dipoles Proximity-Coupled to a Perpendicular Microstripline," *IEEE Trans. Ant. Prop.*, vol. AP-37, pp. 435-444, April 1989.

[12] P. Parhami, Y. Rahmat-Samii, and R. Mittra, "An Efficient Approach for Evaluating Sommerfeld Integrals Encountered in the Problem of a Current

Element Radiating Over Lossy Ground," *IEEE Trans. Ant. Prop.*, vol. AP-28, pp. 100-104, Jan. 1980.

[13] Y. Rahmat-Samii, R. Mittra, and P. Parhami, "Evaluation of Sommerfeld Integrals for Lossy Half-Space Problems," *Electromagn.*, vol. 1, pp. 1-28, 1981.

[14] W. C. Chew and J. A. Kong, "Asymptotic Approximation of Waves Due to a Dipole on a Two-Layer Medium," *Radio Science*, vol. 17, pp. 509-513, May-June 1982.

[15] P. B. Katehi and N. G. Alexopoulos, "Real Axis Integration of Sommerfeld Integrals with Applications to Printed Circuit Antennas," *J. Math. Phys.*, vol. 24, pp. 527-533, March 1983.

[16] H. Yang, A. Nakatani, and J. A. Casteñeda, "Efficient Evaluation of Spectral Integrals in the Moment Method Solution of Microstrip Antennas and Circuits," *IEEE Trans. Ant. Prop.*, vol. 38, pp. 1127-1130, July 1990.

[17] J. S. Bagby and D. P. Nyquist, "Dyadic Green's Functions for Integrated Electronic and Optical Circuits," *IEEE Trans. Microwave Theory Tech.*, vol. MTT-35, pp. 206-210, Feb. 1987.

[18] C. E. Baum, "The Singularity Expansion Method," in L. B. Felson, ed., Transient Electromagnetic Fields, New York: Springer-Verlag, 1976, pp. 128-177.

[19] C. E. Baum, "Emerging Technology for Transient and Broad-Band Analysis and Synthesis of Antennas and Scatterers," *Proc. IEEE*, vol. 64, pp. 1598- 1616, Nov. 1976.

[20] C. E. Baum, "The Singularity Expansion Method: Background and Developments," *IEEE Ant. Prop. Society Newsletter*, pp. 15-23, Aug. 1986.

[21] A. Sommerfeld, "Über die Ausbreitung der Wellen in der drahtlosen Telegraphie," *Annalen der Physik* (4th Folge), vol. 28, pp. 665-736, 1909.

[22] A. Baños, Jr., Dipole Radiation in the Presence of a Conducting Half-Space, Oxford: Pergamon Press, 1966.

[23] A. D. Yaghjian, "Electric Dyadic Green's Functions in the Source Region," *Proc. IEEE*, vol. 68, pp. 248-263, Feb. 1980.

[24] A. Sommerfeld, Partial Differential Equations in Physics, New York: Academic Press, 1964, pp. 236-265.

[25] W. C. Chew, Waves and Fields in Inhomogeneous Media, New York: Van Nostrand Reinhold, 1990.

[26] H. Weyl, *Ann d. Physik* 60: 481, 1919.

[27] W. Fulks, Advanced Calculus, New York: John Wiley and Sons, 1978.

[28] M. S. Viloa and D. P. Nyquist, "An Observation on the Sommerfeld-Integral Representation of the Electric Dyadic Green's Function for Layered Media," *IEEE Trans. Microwave Theory Tech.*, vol. 36, pp. 1289-1292, Aug. 1988.

[29] R. F. Harrington, Field Computation by Moment Methods, New York: The MacMillan Co., 1968.

[30] R. V. Churchill and J. W. Brown, Complex Variables and Applications, New York: McGraw-Hill Book Co., 1984.

[31] R. E. Collin, Field Theory of Guided Waves, New York: McGraw-Hill, 1960.

[32] W. C. Chew and J. A. Kong, "Resonance of the Axial-Symmetric Modes in Microstrip Disk Resonators," *J. Math. Phys.*, vol 21, pp. 582-591, Nov. 1979.

[33] K. A. Michalski and D. Zheng, "Rigorous Analysis of Open Microstrip Lines of Arbitrary Cross Section in Bound and Leaky Regimes," *IEEE Trans. Microwave Theory Tech.*, vol. MTT-37, pp. 2005-2010, Dec. 1989.

[34] A. K. Sharma and B. Bhat, "Spectral Domain Analysis of Interacting Microstrip Resonant Structures," *IEEE Trans. Microwave Theory Tech.*, vol. MTT-31, pp. 681-685, Aug. 1983.

[35] T. M. Martinson and E. F. Kuester, "Accurate Analysis of Arbitrarily Shaped Patch Resonators on Thin Substrates," *IEEE Trans. Microwave Theory Tech.*, vol. MTT-36, pp. 324-331, Feb. 1988.

[36] K. D. Stephan, S. L. Young, and S. C. Wong, "Microstrip Circuit Application of High-Q Open Microwave Resonators," *IEEE Trans. Microwave Theory Tech.*, vol. MTT-36, pp. 1319-1327, Sept. 1988.

[37] D. P. Nyquist, "Deduction of EM Phenomena in Microstrip Circuits from an Integral-Operator Description of the System," *Proc. 1989 URSI Int. Symp. EM Theory*, Stockholm, Sweden, pp. 533-535, Aug. 1989.

[38] B. P. Lathi, Signals, Systems and Communication, New York: John Wiley and Sons, 1965.

[39] N. K. Uzunoglu, N. G. Alexopoulos, and J. G. Fikioris, "Radiation Properties of Microstrip Dipoles," *IEEE Trans. Ant. Prop.*, vol. AP-27, pp. 853-858, Nov. 1979.

[40] M. Abramowitz and I. A. Stegun, Handbook of Mathematical Functions, New York: Dover Publications, Inc., 1972.

[41] C. H. Lee, J. S. Bagby, Y. Yaun, and D. P. Nyquist, "Entire-basis MoM analysis of coupled microstrip transmission lines," To appear in a future *IEEE Trans. Microwave Theory Tech.*

[42] A. Papoulis, The Fourier Integral and its Applications, McGraw-Hill, 1962.

[43] I. S. Gradshteyn and I. M. Ryzhik, Table of Integrals, Series, and Products, San Diego: Academic Press, Inc., 1980.

[44] R. F. Harrington, Field Computation by Moment Methods, New York: MacMillan, 1968.

[45] T. K. Sarkar, "A Note on the Choice Weighting Functions in the Method of Moments," *IEEE Trans. Ant. Prop.*, vol. AP-33, pp. 436-441, April 1985.

[46] T. K. Sarkar, A. R. Djordjević, and E. Arvas, "On the Choice of Expansion and Weighting Functions in the Numerical Solution of Operator Equations," *IEEE Trans. Ant. Prop.*, vol. AP-33, pp. 988-996, Sept. 1985.

[47] I. E. Rana, and N. G. Alexopoulos, "Current Distribution and Input Impedance of Printed Dipoles," *IEEE Trans. Ant. Prop.*, vol. AP-29, pp. 99-105, Jan. 1981.

[48] D. M. Pozar, "Input Impedance and Mutual Coupling of Rectangular Microstip Antennas," *IEEE Trans. Ant. Prop.*, vol AP-30, pp. 1191- 1196, Nov. 1982.

[49] P. B. Katehi, and N. G. Alexopoulos, "On the Effect of Substrate Thickness and Permittivity on Printed Circuit Dipole Properties," *IEEE Trans. Ant. Prop.*, vol. AP-31, pp. 34-39, Jan. 1983.

[50] P. B. Katehi, and N. G. Alexopoulos, "On the Modeling of Electromagnetically Coupled Microstrip Antennas- The Printed Strip Dipole," *IEEE Trans. Ant. Prop.*, vol. AP-32, pp. 1179- 1186, Nov. 1984.

[51] D. M. Pozar, "Finite Phased Arrays of Rectangular Microstrip Patches," *IEEE Trans. Ant. Prop.*, vol. AP-34, pp. 658-665, May 1986.

[52] H. Nakano, S. R. Kerner, and N. G. Alexopoulos, "The Moment Method

Solution for Printed Wire Antennas of Arbitrary Configuration," *IEEE Trans. Ant. Prop.*, vol. 36, pp. 1667-1673, Dec. 1988.

[53] E. Hallén, "Theoretical Investigations into Transmitting and Receiving Qualities of Antennas," *Nova Acta Regiae Soc. Sci. Upsaliensis*, pp. 1-44, Jan. 1938.

[54] W. H. Press, B. P. Flannery, S. A. Teukolsky, and W. T. Vetterling, Numerical Recipes, Cambridge: Cambridge University Press, 1986.

[55] J. E. Ross, E. J. Rothwell, D. P. Nyquist, and K. M. Chen, "Multiple Target Discrimination Using E-Pulse Techniques," IEEE AP-S Symposium Digest, vol. 3, pp. 1342-1345, May 1990.

[56] J. Moore and R. Pizer, ed., Moment Methods in Electromagnetics, England: Research Studies Press Ltd., 1984.

[57] E. Belohoubek and E. Denlinger, "Loss Considerations for Microstrip Resonators," *IEEE Trans. Microwave Theory Tech.*, vol. MTT-23 , pp. 522-526, June 1975.

[58] R. A. Purcel, D. J. Massé, and C. P. Hartwig, "Losses in Microstrip," *IEEE Trans. Microwave Theory Tech.*, vol. MTT-16, pp. 342-350, June 1968.

[59] R. Seckelmann, "On Measurements of Microstrip Properties," in J. F. Frey and K. B. Bhasin, ed., Microwave Integrated Circuits, Mass: Artech House, Inc., 1985.

[60] M. Caulton, J. J. Hughes, and H. Sobol, "Measurements on the Properties of Microstrip Transmission Lines for Microwave Integrated Circuits," in J. F. Frey and K. B. Bhasin, ed., Microwave Integrated Circuits, Mass: Artech House, Inc., 1985.

[61] W. J. Getsinger, "Measurement and Modeling of the Apparent Characteristic Impedance of Microstrip," in J. F. Frey and K. B. Bhasin, ed., Microwave Integrated Circuits, Mass: Artech House, Inc., 1985.

[62] P. Troughton, "High Q Factor Resonators in Microstrip," *Electronics Letters*, vol. 4, pp. 520-522, Nov. 1968.